Graphene for Multi-purpose Applications

Dissertation by

Ramy Mohammed Qaisi

In Partial Fulfillment of the Requirements

For the Degree of

Doctor of Philosophy

King Abdullah University of Science and Technology

Thuwal, Kingdom of Saudi Arabia

EXAMINATION COMMITTEE PAPER

The dissertation of Ramy Mohammed Qaisi was reviewed and approved by the examination committee.

Committee Chairperson: [Dr. Muhammad Mustafa Hussain]

Committee Member: [Dr. Mohammed-Slim Alouini]

Committee Member: [Dr. Lance Li]

Committee Member: [Dr. Sanjay Banerjee]

COPY RIGHTS PAGE

ABSTRACT

GRAPHENE FOR MULTI-PURPOSE APPLICATIONS

In the recent past, graphene has been discovered and studied as one of the most promising materials after silicon and carbon nanotube. Its atomically thin structure, pristine dangling bonds free surface and interface, ultra-fast charge transport capability, semi-metallic behavior, ultra-strong mechanical ruggedness, promising photonic properties and bio-compatibility makes it a material to explore from all different perspectives to identify potential application areas which can augment the quality of our life. Therefore, in this doctoral work the following critical studies have been carried out meticulously with key findings are listed below:

(1) A simplistic and sustainable growth process of double or multi-layer graphene (up to 4" substrate coverage with uniformity) using low-cost atmospheric chemical vapor deposition (APCVD) technique. [presented in MRS Fall Meeting 2012 and in IEEE SIECPC 2012)

(2) A buried metallic layer based contact engineering process to overcome the sustained challenge of contact engineering associated with low-dimensional atomically thin material. (presented in IEEE Nano 2013 and archieved in conference proceedings)

(3) Demonstration of a fin type graphene transistor (inspired by multi-gate architecture) with a mobility of 11,000 cm2/V.s at room temperature with an applied drive-in voltage of ±1 volt to demonstrate for the first time a pragmatic approach for

graphene transistor for mobile applications which can maintain its ultra-fast charge transport behavior with ultra-low power consumption. [Published in ACS Nano 2013]

(4) Further a meticulous study has been done to understand the harsh environment compatibility of graphene for its potential use in underwater and space applications. [Published as Cover Article in physica solidi status – Rapid Research Letters, 2014]

(5) Due to its highly conductive nature and low surface-to-volume ratio it has been used to replace conventional gold based anodic material in microbial fuel cells (used for water purification in self-sustained mode) to demonstrate its effectiveness as a sustainable low-cost mechanically robust transparent material. [Published in ACS Nano 2013, in Energy Technology 2014 as a Cover Article and in Nature Publishing Group Asia Materials 2014]

(6) Extensive study to stabilize graphene surface and to use the phenomena for development of a sensor which can monitor the quality of water. [presented in MRS Fall Meeting 2013 and in MRS Fall Meeting 2014]

(7) By using graphene as an expose transistor architecture with ultra-scale high-k dielectric, to develop a series of sensor for glucose monitoring. Sensitivity, selectivity, response rate and refresh time has been studied and optimized. [pending review in Nature Scientific Reports 2015]

(8) From the lessons learnt during the development of glucose monitoring sensor cell, a sophisticated low-cost ultra-low power mobile graphene based non-invasive

sensor has been assembled and clinically trialed in collaboration with King Faisal Hospitals in Jeddah and in Makkah. [pending review in Science 2015]

As a future direction, this thesis also discusses potential of graphene growth on electrochemically deposited metallic seed layers and consequential usage in stretchable and transparent graphene antenna development for fully flexible only graphene based integrated electronic system integration.

ACKNOWLEDGEMENT

Firstly, I would like to express my sincere gratitude to my advisor professor Muhammed Hussain who has been my mentor since I joined KAUST for the continuous support of my Ph.D study and related research, for his patience, motivation, and immense knowledge. His guidance helped me in all the time of research and writing of this thesis. I could not have imagined having a better advisor and mentor for my Ph.D study. I am blessed to have a mentor like him who has always been there for me and my colleagues as a brother to guide us in the direction of the research and life. My sincere thanks also goes to Mr. Nadhmi Alnasser and Dr. Najah Ashry for the unconditional support since the foundation of KAUST at 2008. Without their precious support it would not be possible to conduct this research and complete my degree. I thank my fellow lab mates Dr. Jhonathan Rojas, Dr. Casey Smith for the stimulating discussions, for the sleepless nights we were working together before deadlines, and for all the fun we have had in the last four years. Also I thank my friends in the ministry of health care. In particular, I am grateful to Dr. Meshal Sadiq and Salim Bazmool for enlightening me the first glance of research. Last but not the least, I would like to thank my family: my parents Mohammed and Eltaf and to my brothers and sister (Raid, Ammar, Reham and Raja) for supporting me spiritually throughout writing this thesis and my life in general. Also, I would like to extend a special gratitude for my wife Kholod whose supported me through all my research work and my life. Finally, special thanks to my friends whose stand by me and provide me every possible support , Justine, Essam, my cousin Faisal, Turki, Hani, Bakri, Abdulaziz Fallatah, Abdullah Sehli, Khalid Ghniem, Mohammed Ghoniem, abdulilah

Mayet, Sulatn Jadani, Mohanned Edini and Wail Bamhair for motivating me the most to complete my degree.

TABLE OF CONTENTS

LIST OF ABBREVIATIONS

DIBL	drain induced barrier limit
NaCl	sodium chloride
HEMT	high electron mobility transistors
CVD	chemical vapor deposition
FET	Field effect transistors
Al_2O_3	Aluminum oxide
MFC	micro bio fuel cell
HOPG	highly ordered pyrolytic graphite
LPCVD	low pressure chemical vapor deposition
APCVD	Atmospheric pressure chemical vapor deposition
MLG	multi-layer graphene
BLG	Bilayer graphene
PMMA	Polymethyl methacrylate
IPA	ISO-propyl alcohol
DI Water	Deionized water

FWHM	Full width at half maximum
ITO	Indium tin oxide
g_m	Transconductance
ALD	Atomic layer deposition
SEM	Scanning electron micrograph
Graphene FinFET	Graphene Fin field effect transistor structure
MOSFETs	Metal oxide semiconductor field effect transistor
CMOS	Complementary metal oxide semiconductor
RF	Radio frequency
CMP	Chemical mechanical planarization
RIE	reactive ion etch
PR	Photo resist
TLM	Transfer length model
SGFET	Solution gated field effect transistor
MBE	Molecular beam epitaxy
MOCVD	Metal organic chemical vapor deposition
S/D	Source and drain

2D	Two dimensional

LIST OF FIGURES

LIST OF TABLES

CHAPTER 1. INTRODUCTION

1.1. Motivation and Dissertation Overview

Graphene – the two dimensional carbon material has received enormous interests from all around the world after its discovery in 2004. The ultra-high mobility up to 200,000 $cm^2\ V^{-1}s^{-1}$ has been reported for graphene [1-3], micro-meter scale mean free path [4,6], Ballistic transport distances of up to a micron at room temperature [7,8] and is a truly 2-dimensional semi-metallic material composed of only one atomic layer of carbon atoms making it an attractive material for nanoelectronics, microelectromechanical systems, bio sensing, transparent electrodes and many other applications.

Ever since its existence in the laboratory via simple easy scotch tape method, the pioneers in the field are in full swing to make graphene synthesis and growth more reliable on a larger scale. The feasibility of realizing graphene devices for low power applications depends heavily on controlling growth parameters which eventually effect the quality of the grown film. Thus controlling the growth environment would allow researchers to adjust graphene intrinsic properties to be modified as per the needs of the application [9]. For example graphene exhibited a pronounced degradation in its carrier mobility due to chemical treatment and fabrication procedures which involves exposure to different chemical processes eventually rendering the device p-doped under ambient conditions.

The conducted research on graphene would eventually change many aspects in the field of solid state physics [10]. Among the exciting graphene properties, two are extra ordinary phenomenon. It's true two dimensionality and dirac particles. Dirac equation are used to describe electron movement in the honeycombed lattice [11,12].

Unconventional half integer quantum Hall Effect of graphene has been verified experimentally at room temperature [13,14]. As a result of its two dimensionality, perpendicular electric field would not disturb the electron movement in lateral direction [15]. In addition, the electrons in two dimensional electron gas 2DEG system are quantized in equidistant landau levels which can be used to describe dirac electrons as well when subjected to perpendicular magnetic field [16]. However Landau levels are following the square room of the magnetic field at not equally spaced .Also, electrons tunneling through high barrier potential (known as Klein tunneling) at 100% probability has been confirmed experimentally using p-n junction [17,18]. Interestingly electrons in graphene are behaving as two dimensional at low temperature, room temperature and high temperate [19]. Thus, two dimensionality of graphene is appealing to researchers because it is allowing for building new architectures which would eventually may change the face of computations .

Another resulted fact in graphene is the conical shape of electronic dispersion near the vertices of the hexagonal Brillouin zone (k point). In mono layer graphene, direct implication of electronic dispersion is that fermions behave as massless particles [20]. While the fermions in bilayer graphene can be described as massive Chiral fermions with a symmetrical band structure near neutrality point [21]. In addition, its natural two dimension system along with the atomic thickness making graphene more sensitive to

ambient changes [22]. Utilization of graphene as channel material in field effect transistors FET has enabled high performance transistors. Due its zero bandgap mono layer graphene suffer low I_{on}/I_{off} ratio [23]. Different attempts to address this issue has been reported under the category of bandgap engineering [24=26]. For instance, using Bi-layer graphene transistors inherently has better I_{on}/I_{off} ratio due to its natural atomic structure [27]. Another approach is by confining the carries into quasi one dimensional 1D through growing graphene nano ribbons GNR [28].

The fabricated CVD graphene transistors has low mobility compared to the projected high mobility mentioned earlier. It is been reported that the mobility in grFET is affected by the interaction between graphene films and the underlying substrate [29], surface charge traps [30,31], interfacial phonons [32] and contamination during fabrication process [33]. Researches has demonstrated different explanation to that issue. For instance, suspended graphene transistors has very high mobility as a proven intrinsic transport properties in graphene [34]. In the latter, graphene is mechanically exfoliated which limits the use of this technique to research laboratory as discussed later in this chapter. Another demonstration was elaborated by integrating high k dielectrics to achieve higher motilities by reducing surface roughness at graphene / dielectric interface [35-37]. Still graphene devices needs more research work to fabricate graphene devices to meet projected characteristics.

No matter how exciting graphene properties are, graphene must be produced first. There are many methods to synthesize graphene. Graphene synthesis can be categorized into two main parts. The top down approach and the bottom up approach. The top down approach relies on having graphene compounds or bulk graphite. Reduction of bulk

graphite yields graphene via direct simple scotch tape process also known as mechanical exfoliation while graphene compounds like graphene oxide and liquid phase exfoliation can be reduced to graphene via chemical routes [38-40]. On the other hand, the bottom up approach is divided into two main methods; (i) chemical vapor deposition CVD [41,42] technique and (ii) epitaxial growth [43,44]. The work on graphene devices based on mechanical exfoliation production resulted in noble prize 2010 and the foundation of new physical phenomena. However, top down methods in general are limited to scientific research and laboratory purposes due to its misalignment with current CMOS technology [45,46]. Lack of reproducibility and scalability are the main obstacles that must be addressed towards making graphene technology adopted by industry. The answer to that quest lies in the bottom up approach. Graphene films synthesized via CVD and epitaxial techniques can grow graphene on wafer scale with CVD advantage of having graphene film size limited to that of metal catalysis size [47,48]. Different metals has been reported as catalysis for CVD graphene growth like nickel, platinum, iridium, ruthenium , palladium and copper [49,50]. Nickel and copper have showed better results compared to other metals. For nickel, carbon atoms decomposed at activating temperature then diffuses into bulk Ni. Then carbon atoms precipitated on metal surface forming graphene layers []. For copper, carbon atoms are directly deposited on top of cu surface []. In the latter case, carbon atoms start nucleating at cracked surface edges then those nuclei merging together forming the seeding graphene layer. Comparing those two mechanisms, suggested that growth on Ni is based on cooling rate of the process while Cu based growth is depending strongly on the surface of the metal. Enhancement of CVD graphene is reported via introducing low vacuum pressure and new furnace designs. Low pressure growth

LPCVD, allow atoms to have less mean free path hence more atoms reached metal surface eventually controlling the growth rate. The use of copper foil as catalysis metal has shown superior properties to deposited Cu with size being to the size of the Cu foil used. It is of worth to mention that epitaxial method does not suffer the latter case because the film is grown directly on deposited copper instead of copper foil. However, the high cost of SiC wafers is a major challenge to eliminate other methods. Thus, developing CVD graphene film is a crucial step in order to have graphene technology in industrial scope. To summarize, graphene synthesis is the main entry toward building new device structures such as sensors, transistors and energy harvesting.

Thanks to the intensive graphene research community which help covering wide range of graphene properties and application in short time periods. There is still a huge window open for investigating graphene potential as a replacement of current silicon technology.

Therefore, developing a simple low cost graphene synthesis process is an important objective in this dissertation. The main characteristics of high quality CVD graphene films are reproducibility, scalability, uniformity, low defectivity and transfer method. It is worth mentioning that keeping graphene properties intact is important to have high quality devices.

Graphene is transferred to arbitrary pre patterned substrates via aqueous media resulting in compromised graphene device properties. Thus, further enhancements is needed to obtain high device properties. The grown film properties must be tailored according to the application and function of the fabricated devices. Dielectric engineering

and contact engineering are aimed to level up the performance of graphene based devices. The integration of high-k dielectric into graphene devices has enabled high mobility values with severe voltage reduction. While, contact engineering by having very low contact resistivity is resulted in higher device sensitivity and better carrier transportation through metal contacts/graphene interface. Hence, the quest of having high quality graphene device properties which can be tailored as per functionality of the device is still open.

Therefore the objective of this dissertation research is to develop a controlled graphene synthesis process, integrating the grown films into pre patterned substrates and build up devices such as sensors and energy harvesters with performance improvements being kept as vital criterion through every phase of graphene device fabrication process. For example, building simple cost, sensitive and low power graphene device that can detect molecular charges on top of high quality graphene based transistors is depending on the intrinsic properties of the grown film after being transferred to the substrate.

Discovery of new sensing platforms based on graphene seems feasible more than any time because the fast progress in the field of graphene. By making use of pristine graphene films, one would realize extreme device performance metrics such as tiny particle that can be rendered as change in electronic properties of the device.

1.2. Dissertation Overview and Chapter Organization

In order to realize graphene based devices, many challenges are ascending in every phase of the fabrication process which must be addressed. These challenges

including graphene synthesis, graphene film transfer, integration of graphene with the fabricated structures.

This research work starts with developing graphene synthesis process based on chemical vapor deposition CVD method in chapter 2. Also, discussion of CVD approach advantages over mechanically exfoliated graphene is included. Although CVD graphene is a promising synthesis technique to fabricate graphene devices, still grown graphene films failed to meet mechanically exfoliated graphene device characteristics values and theoretically estimated values as well. Therefore, we aimed at studying graphene device performance enhancements through engineered dielectric and contacts. Chapter 3, consisting of integrating ultra-scaled high-k Al_2O_3 dielectric (10 nm) into fin graphene back gated transistors FinFET to allow for substantial supply voltage reduction and achieving high mobility as a result of better electrostatic potential control. Moreover, contact engineering study is conducted by developing novel buried contact transistor without the need for further metal deposition/lithography steps. This would allow for full channel exposure to surrounding ambient.

The next to be discussed in chapter 4, is developing graphene devices for sensing application, investigation of graphene behavior at elevated temperature and energy harvesting. Graphene films is utilized as a sensing material to monitor water quality is included then stability of graphene back gate transistors at harsh environment as step to consider graphene devices as alternative to current SiC based devices. Developing CVD graphene on nickel as a cathode material in micro bio fuel cell MFC is then discussed briefly followed by implementing MFC design using growing graphene films using copper foil as catalysis metal to promote the performance.

Finally, graphene devices for medical application is discussed in chapter. We presented a new sensing method based on molecular charge transfer in which the grown graphene films can detect the concentration of glucose in solution without the need for functionalization step. This method is then extended to be used with real diabetes samples collected clinically from well observed patients. Then, comparing clinical measurements with our experimental measurements.

Chapter 2. Graphene Synthesis

In this chapter, I will describe the sustained growth of bilayer graphene synthesis based on chemical methods (chemical vapor deposition) and it is advantages against mechanically exfoliated process. Also, I will highlight the type of growth that we achieved in our lab.

2.1 Stable growth of bi-layer and multi-layer graphene at atmospheric pressure

This work has been presented in SIECPC 2013 conference held in Riyadh by KACST, published accordingly in IEEE 2013.

Ramy Qaisi, Casey Smith, and Muhammad M. Hussain. "Time variant layer control in atmospheric pressure chemical vapor deposition based growth of graphene." Electronics, Communications and Photonics Conference (SIECPC), 2013 Saudi International. IEEE, 2013.

2.1.1. Introduction

Graphene can be prepared by various methods, including exfoliation of graphene from bulk highly ordered pyrolytic graphite (HOPG), chemical reduction of graphene oxide [51], epitaxial growth on SiC substrate [52] and chemical vapor deposition CVD on metal catalysts including Ni, Pt, Iron , Ru, Pd and Cu [53] . Among these methods exfoliated graphene has shown superior carrier transport properties (mobility) however it is not practical for mass production due to the limited produced size and unreliable layer

thickness. Chemical exfoliation gained enormous interest for its mass production capability though the carrier transport properties of the produced films are deteriorated due to the chemical treatments [54]. Recently, CVD graphene synthesis has received significant attention as it yields films whose size is limited only by the dimensions of the metal substrate [55] and its flexibility to modify synthesis conditions to manipulate the electronic properties such as doping, bandgap, resistivity of the resulting film. Among the different metals that have been used as a catalyst for graphene synthesis, copper substrates are preferred because of the metal's extremely low solid solubility of carbon atoms [56]. Graphene has been successfully synthesized using low pressure chemical vapor deposition (LPCVD) by several groups [57]. The impact of different growth parameters has been studied carefully for LPCVD and APCVD [53,58]. It has been suggested that hydrocarbon dissociation on copper surfaces at low pressure results in graphene film growth kinetics that are self-limiting to 1 or 2 layers [59]. On the other hand, APCVD growth does not appear to adhere to this same trend and film thickness is essentially controlled by time of exposure to the carbon source. While this growth dynamic represents an additional challenge to achieve highly uniform graphene coverage over large areas, the cost effective nature of atmospheric pressure furnace processing can enable significantly higher throughput for mass production of graphene used for transparent electrodes and analogue components. In this work, we present time controlled synthesis and characterization of uniform and continuous bilayer graphene (BLG) and multi-layer graphene (MLG) films synthesized at atmospheric pressure. Very low concentration of methane precursor helps maintain uniformity by suppressing homogeneous nucleation site density resulting in graphene sheets with large domain size.

2.1.2 Growth and Transfer Method

Graphene films were synthesized by atmospheric pressure chemical vapor deposition on commercially available copper foils (25 μm, 99.8%, Alfa Aesar) in a custom tube furnace (figure 2.1.a). The copper foils were cleaned with Acetone, isopropyl alcohol, deionized water and dried with nitrogen before placing into a 4 inch quartz boat and loaded into the horizontal tube furnace. The system is then ramped to 800˚C at rate of 80˚C/min in while flowing Argon and Hydrogen at 300 sccm and 10 sccm respectively for initial Cu cleaning. Then, the temperature is raised to 1050˚C at 5˚C/min and under constant Argon and Hydrogen flow for 30 minutes in order to fully reduce the copper surface. Methane gas diluted in argon (500ppm) is introduced in place of pure argon for a duration from 20-60minutes to grow graphene. Immediately after the growth duration, the sample is quenched by physically moving the sample out the hot zone and is cooled under the flow of Argon and Hydrogen. The growth profile is shown in Figure 2.1.b.

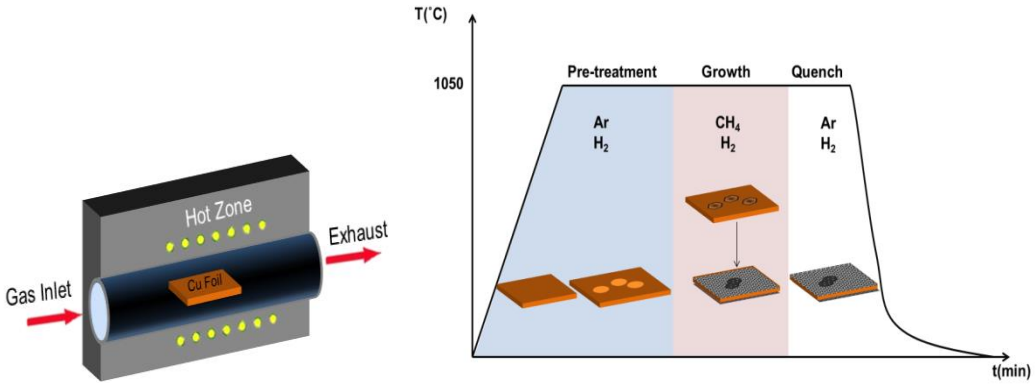

Figure 2.1. Schematics and growth profile.

a) schematic of CVD system and b) growth profile along with process Cu grain boundary formation and graphene nucleation.

Transfer of the synthesized graphene to glass slides begins with removal of the graphene from one side of the copper foil using a 3 minutes etch in nitric acid diluted 1:3 in deinionized water.

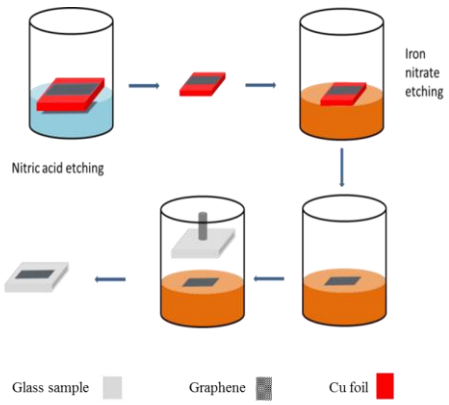

Figure 2.2. CVD graphene transfer scheme without using PMMA.
First, back side etching is performed using nitric acid then iron nitrate etching is performed to etch Cu and finally transfer of the released film is done using vacuum holder to glass substrate.

After rinsing in deionized water the copper foil is then transferred into a solution of 33% weight iron nitrate dissolved in deionized water that completely etches the copper foil in approximately 1 hour. It should be noted that this transfer technique does not make use of any handling layer for transfer such as Polymethyl methacrylate (PMMA) and is not recommended for graphene films as they will simply break apart in solution with minimal agitation. Additionally, since there is essentially no optical signature for the graphene sheet transferred without a handling layer we found it useful to shine very bright light at oblique angles on the surface of the iron nitrate solution to identify the exact location of the floating graphene prior to final transfer. Finally, a vacuum wand was used to pick up a glass slide cleaned in iso-propyl alcohol (IPA) and then translated

downward parallel to the floating graphene sheet until contact. The graphene on the glass slide was gently washed in DI water and IPA to remove iron nitrate residuals. It should be noted that the hydrophobicity of graphene aids the eye in determining its exact location on the glass slide during this final rinse. A diagram of this transfer process is shown in figure 2.2.

2.1.3 Results and discussion

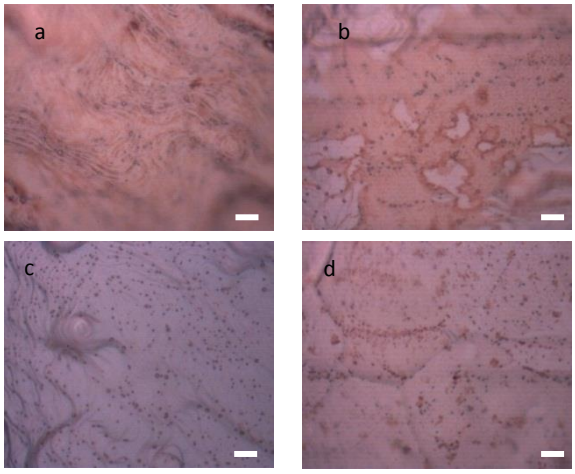

Figure 2.3. Optical images of grown CVD graphene on Cu foil at atmospheric pressure for different growth times and constant flow rate of CH_4 and H_2.
a) 50 minutes growth time; b) 40 minutes growth time; c) 30 minutes growth time; And d) 25 minutes growth time. The scale bar is 10 mm.

Figure 2.3, shows different samples grown with changing time only. It is clearly observed that time plays important role in graphene growth process and thickness. The darkest pattern (a) corresponds to a multi-layer graphene (3-10 layers), and the lighter patterns seen in (b) are thinner graphene regions of one to three layers. These thin graphene regions are distributed homogeneously over the surface of the Cu foil, with the size strongly depending on the dimensions of the under lying domains. Multi-layer

graphene is obtained at 50 minutes growth time (figure 2.3.a). As the time is decreased, further reduction in the number of grown layers is observed (figure 3 b–d). Further evaluations of the grown films were performed using Raman spectroscopy technique as shown in figure 2.4.

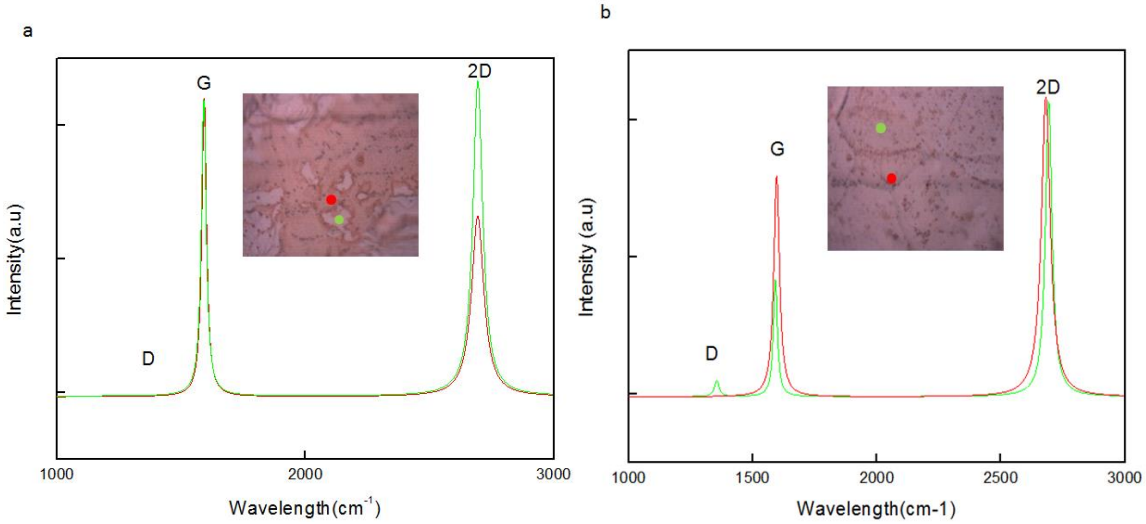

Figure 2.4. Raman spectrum of the grown graphene at different times and locations to verify the obtained number of graphene layers and elucidate the different graphene thicknesses

a) The graphene grown in 40 minutes, the red spectral shows multi-layer grown film while the green spectral is indicating bilayer graphene film with 2D/G ratios of 0.5 and 0.9 respectively; And b) The graphene grown in 25 minutes, the red spectral acquired from dark region contrast showing bilayer film with 2D/G ratio of >1 compared to 2D/G ratio of >2 for green spectral acquired in the areas that show brighter contrast.

The Raman spectra in Figure 2.4.a, for the sample with 40 minutes growth time reveals two different 2D/G Intensity ratios taken from the different contrast regions evident in the optical microscope image and confirms the presence of two different graphene thicknesses. The absence of D peaks indicate that the films have long range sp^2 bond order and the 2D/G ratios of 1 and 0.6 indicate BL and ML graphene respectively.

To evaluate graphene films uniformity, we performed Raman mapping techniques of the samples that shows high homogenous under optical microscopy (30 minutes and 50 minutes). Raman mapping acquired for these two specimens shown in Figure 2.5 confirms a high degree of uniformity in the 2D/G ratio. The Raman maps cover areas >150 μm^2 and indicate that these films are predominantly of one uniform graphene thickness. Figure 2.5.a, has a 2D/G ratio in the range of 0.2 characteristic of multilayer (4L-5L) graphene film whereas the film mapped in Figure 2.5b reveals a 2D/G ratio between 1 and 2 indicating the presence of uniform bilayer graphene. Figure 2.6.a, summarizes the growth trends as a function of time of our method compared with best results at low pressure. It is to be noted that graphene number of layers is a function of I_{2D}/I_G ratio, 2D peak position and FWHM. It is illustrated in Figure 2.6.b, that the peak position is down shifted as number of layers increases while it is upshifted for decreased layer number.

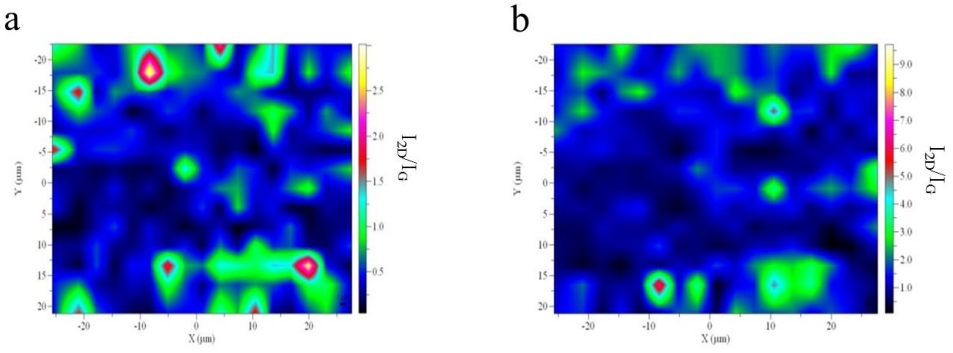

Figure 2.5. Raman mapping for the samples grown in 50 minutes and 30 minutes respectively

a) The sample grown in 50 minutes, the majority of the map reveal 2D/G ratio in the range of 0.2-0.7 which representing multi-layer graphene of 4-5 layers; and b) the sample grown in 30 minutes, the map indicating that the predominant area of the grown film is a bilayer graphene with 2D/G ratio in the range of 0.8 -1.5 which are a characteristic of bi-layer graphene.

The two optically homogenous samples are transferred to glass samples for transmittance and sheet resistance measurements. Figure 2.7 shows the optical transmission spectral of the uniform ML and BL graphene respectively. The transmittance of both graphene specimens is superior to the most widely used transparent conductor indium tin oxide (ITO). The measured quantities are summarized in table 2.1.

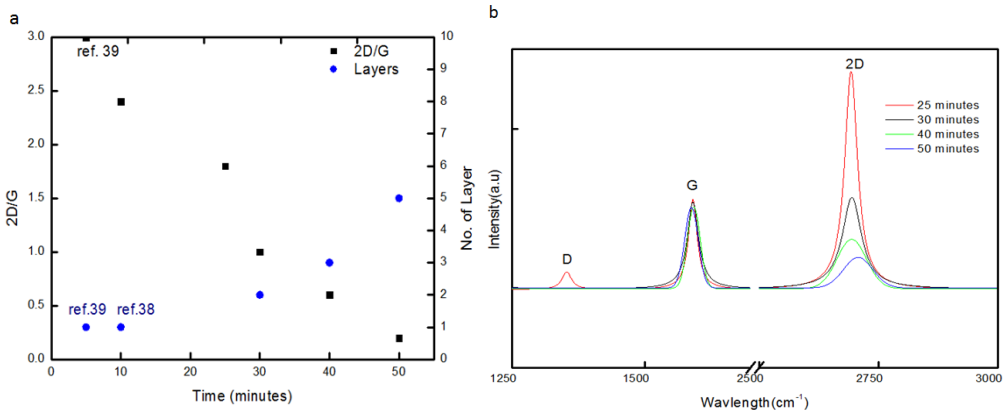

Figure 2.6. The trend of 2D/G ratio with time and acquired Raman signals at various growth times.
a) the 2D/G ratio and number(s) of grown CVD grapene layers with time; and b) the acquired Raman spectrum for 50, 40, 30 and 25 minutes respectively with a clear shift in the position of 2D peak in the 50 minutes growth time spectral as a result of the movement from thinner to thicker graphene film.

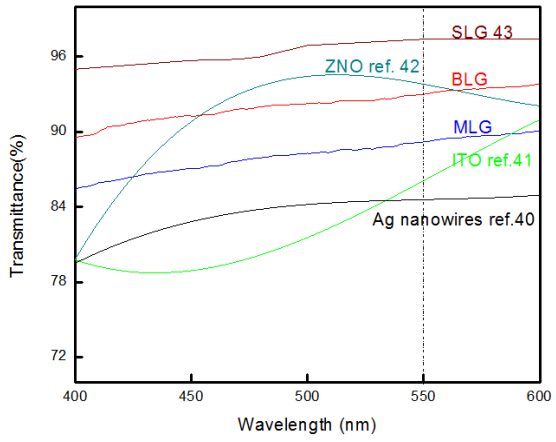

Figure 2.7. Transferred graphene transmittance measurement for bilayer graphene (BLG blue) and multi-layer graphene (MLG red) compared with different materials at a wavelength of 550 nm.
The different spectrum are Single layer graphene (SLG) exhibits 97.1% transperancy, BLG with 92.8%, MLG with 89.1 %, ZnO with 93.8%, ITO with 87% and Ag nanowires with 84.5%.

Table 2.1. The properties of the grown graphene films at 30 and 50 growth times.

Sample	Growth time	D/G	Layers	Optical transmittance (%)	Sheet resistance(Ω/□)
BLG	30	0.9	2	92.8	818.9
MLG	50	0.4	4-5	89.1	733.8

2.1.4 Conclusion

We report time controlled uniform growth of transparent and continuous bi to multi-layer graphene in atmospheric chemical vapor deposition system. We examine the quality of graphene using Raman spectroscopy and support the observation with electrical characterization. The obtained high uniformity provides a cost effective and reliable solution for developing wafer scale graphene coverage.

2.2 Related Achievements

Based on the developed methods of graphene synthesis, we have successfully obtained graphene directly on deposited nickel (Ni) on SiO_2 substrates. Also, graphene

oxide is obtained for both Cu foils and deposited Ni. Table 2.2, summarizes the obtained graphene films categories.

Table 2.2. Summary of the obtained films.

Substrate	Type of Graphene film	size	Pressure	Comments
Deposited Ni	Multi-layer	Half of 4-inch wafer	Atmospheric	Variant growth profile is found where graphene grew on half of the wafer in a profile distributed from 3 layers to less than 10 layers.
	Multi-layer	1cm X 1.5 cm	Low pressure	Poor uniformity with excellent coverage.
	Graphene oxide	1cm X1.5 cm	Atmospheric	Excellent coverage and high degree of uniformity, Ni thickness in the range from 500 to 1000 nm.
Cu foils	Bi-layer	6 cm X 6 cm	Atmospheric	Homogenous and uniform.

	Multi-layer	6 cm X 6 cm	Atmospheric	Homogenous and uniform, number of layers is controlled by time.
Deposited Cu	Graphene oxide	1 cm X 1.5 cm	Atmospheric	The film is not continuous.

Chapter 3. Performance Enhancements of Graphene Back Gated Transistors

In this chapter, I will describe my efforts toward realizing high performance graphene devices. First, describe the effect of high-k dielectric on carrier mobility. Then, I will demonstrate buried contact graphene device and how it improved contact resistance. Finally, future challenges to improve graphene back gated devices are briefly discussed.

3.1 Dielectric engineering

This work has been published as "Smith, C., **Qaisi, R.**, Liu, Z., Yu, Q., & Hussain, M. M. (2013). Low-Voltage Back-Gated Atmospheric Pressure Chemical Vapor Deposition Based Graphene-Striped Channel Transistor with High-κ Dielectric Showing Room-Temperature Mobility> 11 000 $cm^2/V\cdot s$. ACS nano, 7(7), 5818-5823."

3.1.1 Introduction

Utilization of graphene may help realize innovative low power replacements for III-V materials based high electron mobility transistors (HEMT) while extending operational frequencies into the THz regime for superior wireless communications, imaging, and other novel applications. Device architectures explored to date suffer a fundamental performance roadblock due to lack of compatible deposition techniques for nanometer scale dielectrics required to efficiently modulate graphene transconductance (g_m). Room temperature carrier mobility of >100,000 cm^2/V-s, small but controllable band gap, and very high cut-off frequency – are some of the electronic properties of

graphene that makes it one of the key enabling materials for realizing low power RF devices spanning the THz regime [60-62]. Many groups have previously reported on the performance of back-gated field effect transistors utilizing graphene synthesized by various techniques including exfoliation of HOPG, chemical vapor deposition, epitaxial growth on SiC, and reduction of graphitic oxide [63,64]. The vast majority of these devices utilize thick silicon dioxide (SiO_2) as the gate dielectric to facilitate optical detection albeit at the expense of very high switching voltage. Attempts have been made to tailor the thickness of higher dielectric constant materials such as silicon nitride (Si_3N_4) or aluminum oxide (Al_2O_3) that still preserve the optical signature of graphene resulting in improved electrostatic coupling [65]. Unfortunately, even the reduced thickness of these materials compared to SiO_2 still require high switching voltage because the dielectric thickness is an order of magnitude too large for high speed/low power devices. In this work, we overcome two important barriers to study graphene interaction with scaled high-k dielectrics: (i) the difficulty of dielectric deposition on hydrophobic (untreated/pristine) graphene and (ii) lack of optical signature for graphene transferred to scaled high-k dielectrics. The key to achieving this study is fabrication of back-gated devices on heavily doped silicon wafers capped with scaled ALD gate dielectric and circumventing the need for graphene optical detection by utilizing continuous, uniform, and wafer sized high quality graphene synthesized by chemical vapor deposition such that the need for precise alignment of discrete source/drain contacts is eliminated. Hence, the dielectric needs no seed layer because it is grown directly on a silicon wafer using industry standard ALD processes and the complete lack of optical contrast is not a

hindrance since we transfer large (~6 cm x 6 cm) highly uniform graphene sheets that cover the majority of the wafer surface.

3.1.2 Fabrication

First, graphene film was synthesized using the same method described in chapter 2, section 2.2. After growth was completed, the film is then transferred based on poly methyl methacrylate (PMMA) to heavily doped Si wafers coated with either 27.5 nm silicon dioxide (SiO_2) or <10 nm aluminum oxide (Al_2O_3). The SiO_2 was grown by dry/wet/dry oxidation sequence in a tube furnace whilst Al_2O_3 was grown via atomic layer deposition (ALD) using tri-methyl aluminum precursor and H_2O reactant at 200-250˚C with deposition rate of ~1Å/cycle. After solvent removal of PMMA, the wafers were exposed to a nitrogen/hydrogen gas mixture at 450^{o}C for 10 minutes to remove any additional PMMA residue and promote photoresist adhesion. Contact mask based liftoff lithography was utilized to pattern 50/200 nm Ti/Au source/drain contacts deposited via e-beam evaporation. Finally, a second mask was used to preserve graphene in the channel regions upon exposure to a short duration O_2/Ar reactive ion etch (Figure 3.1).

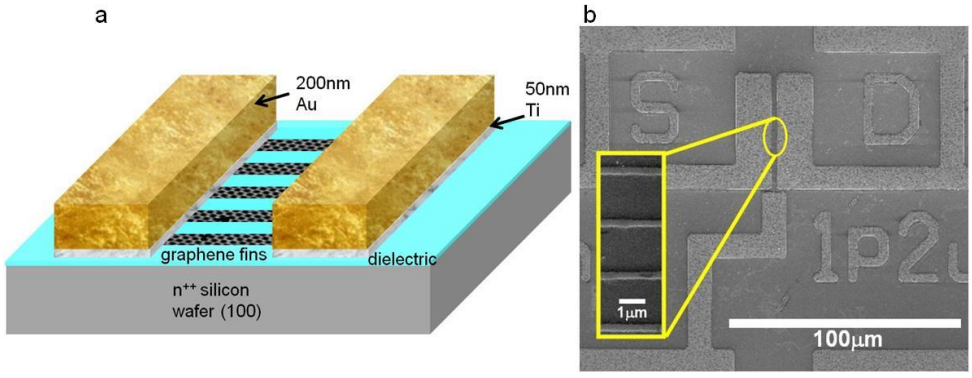

Figure 3.1. Schematics of the fabricated FinFET and SEM image of the fins. a) Schematic of device after PMMA transfer of large 60 cm x 60 cm sheets of CVD graphene to the Al_2O_3 dielectric surface, liftoff processing of the Ti/Au contact metal,

and finally patterning of the graphene fins in the channel region. It is important to note that there is almost no contrast following PMMA removal, hence the need for large area graphene over the 100mm wafer to ensure a statistically sound data set. b) Scanning electron micrograph (SEM) of a representative device. The inset shows sub micrometer fin structures of graphene coated with photoresist for clarity.

3.1.3 Results and Discussion

Raman spectral were taken before and after the PMMA transfer to both substrates to demonstrate the successful transfer process as shown in Figure 3.2.a. The Raman spectra shown possess an I_{2D}/I_G ratio of 2-3 depending upon the substrate with little or no evidence of peaks signature of defects thereby confirming the high quality of the graphene used in this study. Raman mapping is utilized to ensure larege area graphene film were transferred to the grown high-k dielectric as shown in Figure 3.2.b. the Raman map indicates a fairly uniform normalized I_{2D}/I_G peak intensity ratio over a large 40 μm X 40 μm area whilst the accompanying optical image (of graphene on SiO_2) shows isolated higher contrast spots where the graphene sheet has wrinkled or folded during PMMA transfer from the Cu foil substrate. It is also noticed that the full width at half maximum (FWHM) of G band peak increased after transferred to oxide substrates. Also, another peaks seemed to rise after transferred to Al_2O_3 substrate. On the other hand, the 2D band is downshifted on both substrates. These observations are attributed to uniaxial strain that is produced by the Al_2O_3 dielectric [66].

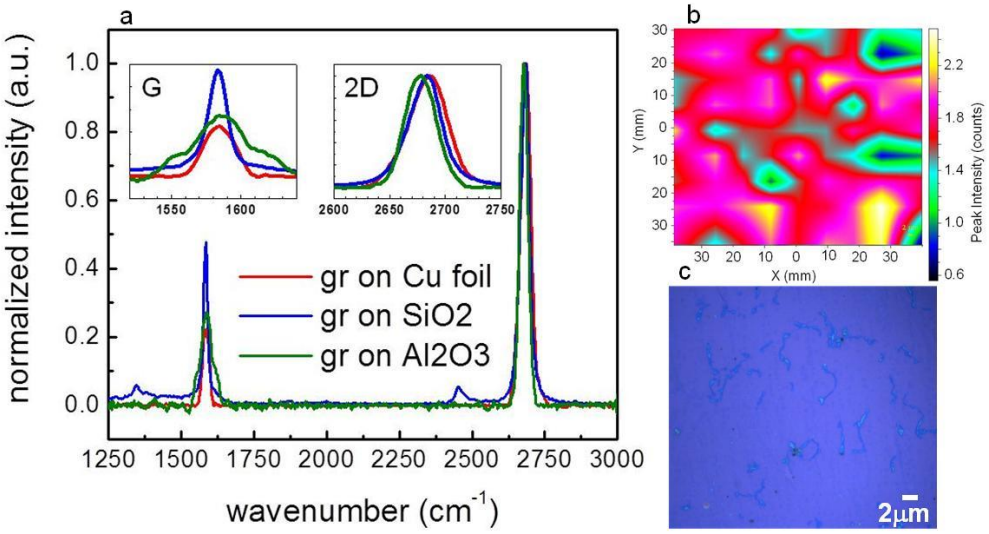

Figure 3.2. Raman Analysis of the grown film along with large area raman map with optical image of the transferred film. a) Raman signatures of graphene films on copper foil and after transfer to the dielectric coated substrate. It is to be noted that a much higher attractive force existed between graphene and the Al_2O_3 substrate compared to SiO_2 during transfer from the final DI water rinse to the host substrate. Specifically, the graphene sheet could be "repositioned" on the SiO_2 substrate as it glided over the interfacial water layer whereas the graphene irrevocably "stuck" to the Al_2O_3 surface upon contact. This increased attractive force may have contributed to the residual strain in the graphene on Al_2O_3 as seen in the inset of the G peak. b) Large area Raman mapping of the I_{2D}/I_G intensity ratio indicates continuous and relatively uniform graphene over very large areas. This criterion was especially important for this study due to the lack of optical contrast between graphene and the thin Al_2O_3 dielectric. c) optical image of graphene after transfer to SiO_2 substrate showing wrinkled and folded regions that give rise to anomalies in the raman map.

Gate overdrive normalized transfer characteristics of representative devices with gate length, L_g = 2.4 μm on SiO_2 and Al_2O_3 substrates are shown in figure 3.3. Both devices exhibit p-type conduction typically seen in CVD derived graphene films transferred from the growth substrate to the insulating substrate in aqueous solution media. The device with scaled high-k Al_2O_3 dielectric and FinFET type graphene channel

has an I_{ON}/I_{OFF} ratio of 3.75, and almost 3000x higher normalized peak linear transconductance (g_m) than the SiO_2 specimen. These characteristics are rarely seen in back gated devices and are attributed to the high quality of the graphene channel material and the enhanced electrostatic coupling through the thin high-k dielectric into the graphene fins. The deposited ultra-scaled high-k dielectric offered a very low voltage (from -1V to 1V) and better electrostatic control over graphene channel compared to SiO_2 substrate. Moreover, we note that our device escapes many of the parasitic fringing field issues present in ultra-thin body silicon MOSFETs due to the lower V_{ds} required for efficient graphene transistor operation and the nanometer scale thickness of the buried Al_2O_3 [67].

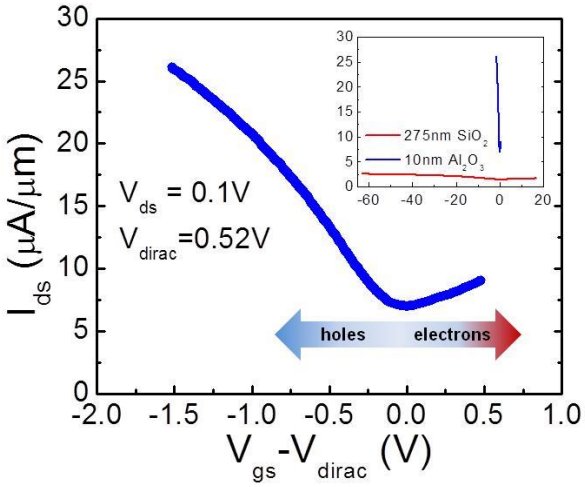

Figure 3.3. Width normalized Id-Vg plot for the back gated device on thin Al2O3 dielectric. Despite having only the back gate and graphene fins on the order of 250 nm the device still exhibits excellent I_{ON}/I_{OFF} of 3.75. Electron conduction is severely inhibited in these devices due to heavy p-type doping. Typical gate leakage current was < 10nA over the range of V_{gs} shown with breakdown occurring between 2.5-3V V_{gs}. The inset shows the dramatic improvement in gate control from adopting the scaled gate dielectric.

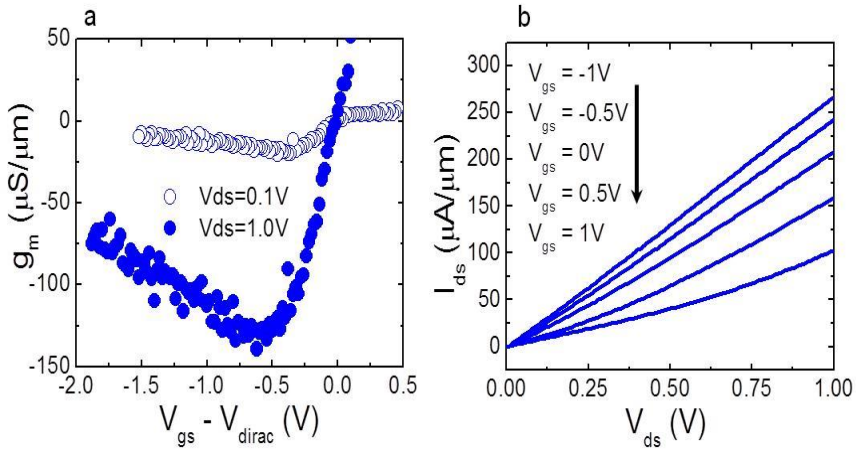

Figure 3.4. transconductance of FinFET compared to graphene on SiO2 substrate and Id-Vd curves. a) Comparison of width normalized transconductance for linear and saturation V_{ds} conditions highlighting the ease of switching the device state at a fraction of gate voltage typically required for back gated FETs. b) I_dV_d curves indicate the device retains appreciable I_{ON}/I_{OFF} ratio in saturation It is important to note that the combined saturation gm of ~140 μS/μm, I_d^{sat} >250μA/μm, and I_{ON}/I_{OFF} ratio >2.5 outstrip any of the seeded ALD dielectric growth techniques presented in [18].

Saturation transfer characteristics shown in Figure 3.4 using a -1V to 1V supply indicate a peak g_{mSAT}/I_{drive} ratio that surpasses even the best top gated devices with seeded deposition ALD films while still maintaining an I_{ON}/I_{OFF} ratio > 3 [68]. A model was used to extract effective mobility yielding an intrinsic (sheet) carrier concentration of ~1.42 x 10^{12} cm^{-2} and contact resistance that varies between 70-80% of the total device resistance depending upon the back gate voltage value in good agreement with other work [69,70]. The extracted mobility is found to be > 11,000 $cm^2\ V^{-1}s^{-1}$

3.1.4 Conclusion

Here we presented the integration of a scaled (<10 nm) high-k gate dielectric aluminum oxide (Al_2O_3) with chemical vapor deposition (CVD) derived graphene

channel using FinFET architecture to realize mobility > 11,000 $cm^2\ V^{-1}s^{-1}$. The high mobility is a by-product of the graphene growth quality, enhanced electric field offered by pristine scaled gate dielectric, and superior electrostatic control of the graphene fins. The record saturation drive current and conductance compared to other top-gated devices requiring undesirable seed assisted dielectric deposition suggests that this facile transistor structure provides critical insight toward future device design to maximize CVD based graphene transistor performance. It is to be noted that recently semiconductor industry has adopted a non-planar architecture tri-gate or FinFET for better electrostatic control and enhanced performance. Up to the best of our knowledge, our demonstration is the first ever FinFET device using graphene as channel material.

3.2 Contact Engineering

This work has been presented in IEEE Nano 2013 conference held in China. And published accordingly in **Qaisi, R. M.**, Smith, C. E., Ghoneim, M. T., Yu, Q., & Hussain, M. M. (2013, August) In Nanotechnology (IEEE-NANO), 2013 13th IEEE Conference on (pp. 890-893). IEEE.

3.2.1 Introduction

The extremely high intrinsic carrier mobility coupled with very small (engineered) bandgap makes graphene a promising candidate for future low power radio frequency (RF) analog devices where speed rather than high I_{on}/I_{off} ratio is most critical [71]. Achieving high performance low power graphene devices and circuits mandates

intelligent choice of materials and fabrication techniques for contacts used to inject carriers and the gate dielectric for electrostatic actuation of drive current [72,73]. For current-generation silicon metal-oxide-semiconductor transistors (MOSFETs), the International Technology Roadmap for Semiconductors calls for a contact resistance of 80 μΩ-m per contact, which is about 10% of the transistor's on-resistance $V_{DD}=I_{ON}$ [24]. Not Optimized contacts between graphene and metal electrodes can significantly increase device resistance and severely limit performance. Engineering low device contact resistance is aimed at increasing I_d [25,26] compared to band gap engineering for decreasing I_{off} [27]. In theory, the absence of a band gap in graphene should make ohmic metal contacts quite easy to obtain low resistance. However, small density of states in graphene suppresses current injection from the contacts resulting in non-negligible contact resistance (RC) [28]. It is suggested that contact resistivity ($\rho_{contact}$) should be less than ~10-9 Ω-cm^2 for miniaturized graphene transistors [29]. Different contact resistivity values have been reported for various graphene growth methods with the lowest value obtained using epitaxially grown graphene on SiC substrate is less than 10 μΩ-cm^2 compared to $\rho_{contact}$ in the range from 2 μΩ-cm^2 to 5 μΩ-cm^2 for CVD grown graphene and mechanically exfoliated graphene [21,30]. Clearly, additional research is required to identify appropriate materials and processes to achieve the target contact resistivity on the order of nΩ-cm^2. Here, we demonstrate a novel structure for direct measurement of contact resistivity that eliminates the need for metal deposition directly on graphene, permits direct access to the graphene-metal interface enabling further chemical treatments/characterization, facilitates wrinkle free transfer of graphene to a planar surface generated without the use of complex chemical mechanical planarization (CMP) processing, and broadens the

variety of available metals used to research graphene contact resistivity. We feel that this methodology is ideally suited for systematic engineering of materials and processes needed to realize high performance low power RF carbon based electronics.

3.2.2 Fabrication

First, graphene film was synthesized using the same method described in chapter 2. After growth was completed, the film is then transferred based on poly methyl methacrylate (PMMA) to a test wafer. Preparation of the test wafer started with 3000 Å thermal oxidation of a heavily doped Si wafer followed by metal lithography. Buffered oxide etchant (BOE-7:1 Transene) was used to recess the SiO_2 by approximately 1500Å. Deposition of 20 nm titanium adhesion layer and 120 nm gold via physical vapor deposition (PVD) was followed by gentle sonication in acetone for the lift-off process and O_2 ashing to remove any additional photoresist residue. Graphene was then transferred from aqueous media onto the planar test wafer surface and dried in N_2 after which PMMA was removed by hot N-Methyl-2-pyrrolidone (NMP), acetone and isopropyl alcohol (IPA). Finally, photo-resist (PR) patterning of graphene in an oxygen/argon reactive ion etch (RIE) and subsequent PR removal in acetone completed the fabrication sequence as shown in Figure 3.5.b.

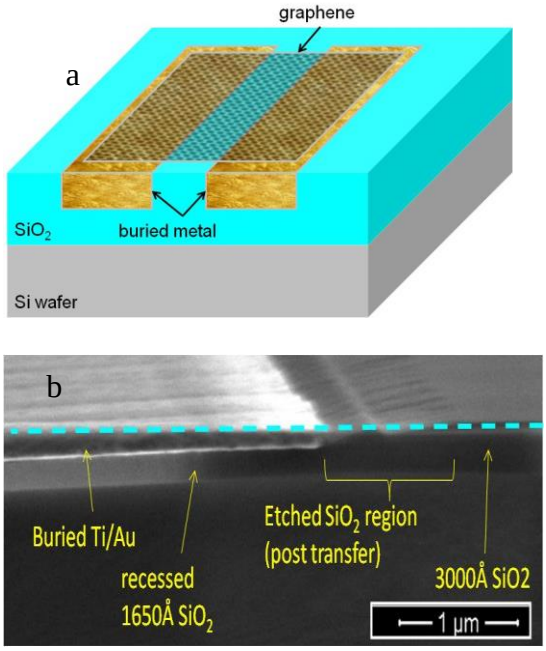

Figure 3.5. Shows the schematic of the buried gate structure and a cross section SEM image. a) the schematic of the proposed novel buried contact structure; and b) the cross section of the buried contact metal structure that shows that Au /Ti gold is deposited on the recessed SiO_2 while the surface is planar (blue dashed line) after graphene transfer.

3.2.3 Results and Discussion

Transfer of the graphene to the buried contact structure helps avoid film wrinkling, breakage and delamination due to the coplanar metal/SiO_2 surface shown in Figure 3.5.a. It is important to note that the recessed oxide region near the edge of the metal pad is a byproduct of the graphene RIE and hence only appeared after transfer. Raman spectroscopy and mapping of the as grown graphene on Cu foil indicate an I_{2D}/I_G ratio of ~2 with no defectivity peak ID indicating that our bilayer graphene is of high quality and uniformity (Figure 3.6).

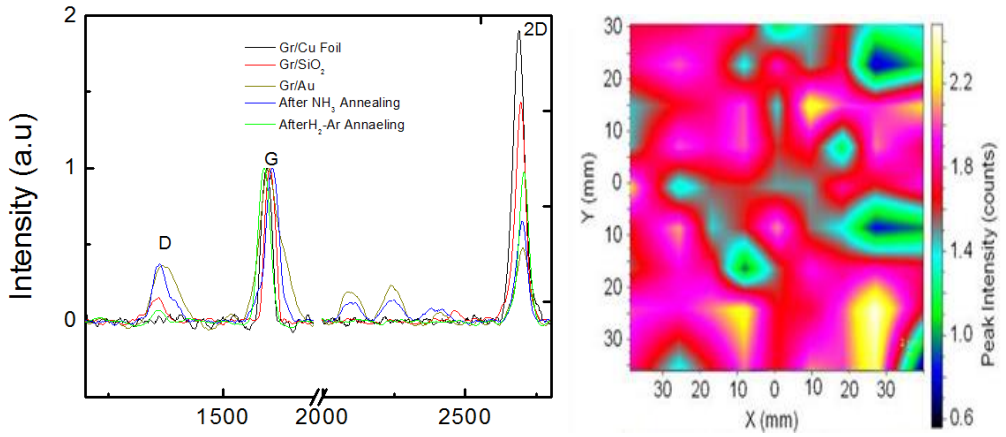

Figure 3.6. The acquired Raman spectrum of graphene and Raman mapping of the grown graphene film: a) Raman signatures of graphene films on copper foil (black), after transfe to SiO_2 (red), after transfer to buried contact metal surface (yellow), after NH_3 annealing(blue) and after H_2-Ar annealing(green). It is found that the PR is not thoroughly removed as indicated in the spectrum of Gr/Au and after Nh_3 annealing. The rise in D band after NH_3 annealing is showing that the graphene is doped with NH_3. The PR is removed after H_2-Ar gas mixture annealing; b) Large area Raman mapping of the I_{2D}/I_G intensity ratio indicates continuous and relatively uniform good quality graphene over very large areas. The raised peaks from 200 cm^{-1} to 2500 cm^{-1} for the shown spectra is indicating that PR residual is not thoroughly resolved.

Linear fitting of resistance versus channel length data yields transfer length (LT) and contact resistance (R_{con}) as a function of back gate voltage (V_{bg}) and ultimately allows for extraction of contact resistivity based on the transfer length method (TLM) [31]. Despite statistical variation in the example graphene devices tested shown in Figure 3.7, we still see the expected trend of decreasing channel resistance (slope) with more negative V_{bg} indicating p-type graphene. Moreover, we note a slight change in the contact resistance as a function of V_{bg} as observed by other groups that could be more pronounced due to the buried contact structure we have employed. The low contact

resistivity in the range of 1 μΩ-cm^2 suggests that the as transferred Au-graphene contact resistivity is inherently favorable as suggested by [32].

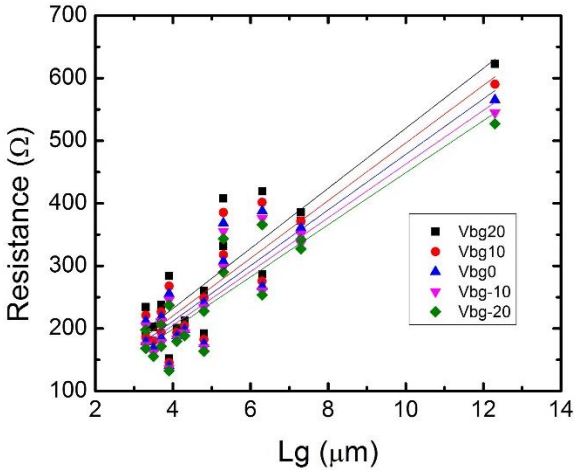

Figure 3.7. R–Vg plot for Au contacts on graphene showing the resistance as a function of distance and Vg. The plot of TLM method is showing that the sheet resistance ρ_{sheet} (slope) decreased as the $V_{g\ decreased}$ indicating that the Au/graphene contact is less sensitive to holes than that for electrons.

The effect of NH_3 annealing on device contact resistivity shows a much stronger effect with higher temperature (Figure 3.8). We attribute the increased contact resistivity post NH_3 anneal to a less favorable injection of electrons to/from graphene-Au due to the metal's high work function. Although contact resistivity increased after NH_3 annealing, we note a much stronger inversion response for the same V_{bg} range as seen in the obtained I_d -V_g curves in Figure 3.9. The clear shift in V_{dirac} towards zero corroborates the observed increased channel resistance because the device is no longer experiencing the same gate overdrive (V_{bg}-V_{dirac}). A similar observation for FGA of the graphene FETs seen in Figure 3.9.b, can be explained by the removal of organic residue altering the Dirac point.

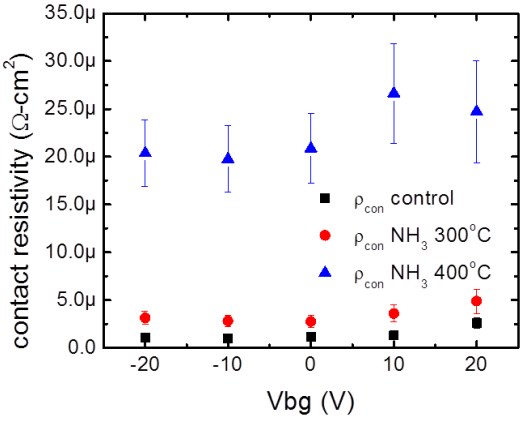

Figure 3.8. The contact resistivity as a function of Vbg. It is observed that the contact resistivity is increasing with NH_3 annealing. The back gate bias is causing a slight change in the contact resistivity due to the injection of carriers from graphene into gold and from gold to graphene.

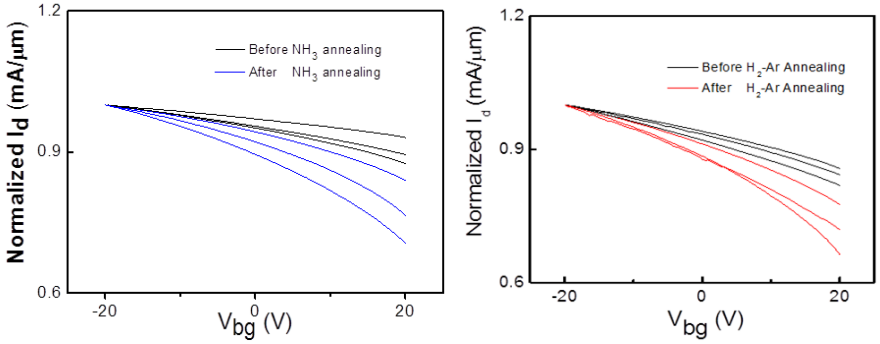

Figure 3.9. Id -Vg plot for the buried contact metal device before and after NH3 and H2-Ar gas mixture annealing. It is noted that the contact resistivity decreasing as the device is exposed to NH_3 and H_2-Ar gas mixture while the graphene channel resistivity is decreased in both cases: a) the I_d-V_{bg} before and after the exposure to NH_3. The observed shift in dirac point (blue) is attributed the compensation of carriers population (electron) occurred after doping the graphene with NH_3; b) the I_d-V_{bg} before and after annealing in H_2-Ar gas mixture under vacuum. The pronounced shift dirac point (red) is caused by the removal of PR and PMMA residual after annealing in vacuum.

3.2.4 Conclusion

We report on the fabrication of a buried metal contact structure for facile study of metal/graphene contact resistivity. The low extracted contact resistivity for Au/graphene (~1 $\mu\Omega$-cm^2) implies that processing issues alone may account for the high contact resistance reported in much of the graphene device literature. Annealing in NH_3 and H_2-Ar mixture indicates that metal work function selection may be a critical component of lowering contact resistivity to graphene based on its predominant carrier type (doping). This novel test vehicle can be utilized to test a wide variety of material and processing options for realizing low contact resistance in graphene transistors for low power RF applications.

Chapter 4. Graphene Applications

In this chapter, development of graphene sensor based on back gate transistor structure is illustrated. First, water quality sensor based on graphene channel ion sensitivity is shown. Then, I will talk about graphene behavior at high temperature as a step toward realizing graphene sensors for high temperature application. Finally, I will talk briefly on my contribution in building graphene micro biofuel cells.

4.1 Water Quality Sensor Based on Graphene Ion Sensitivity

This work has been presented in MRS 2013 fall meeting held in USA. "**Ramy Qaisi**, Casey Smith and Muhammed Hussain, "Ion Sensitivity from Back Gated Graphene Field Effect Transistor""

4.1.1 Introduction

Graphene is a unique platform for sensing application since it is simple, less expensive and requires less energy due to its extraordinary properties [33]. Comprised of a single layer of carbon with every atom on its surface, graphene is a full two dimensional material where the whole volume is exposed to surface absorbs that results in a change of graphene conductivity. The high sensitivity of graphene to tiny local environmental changes in its conductivity gives rise to interesting sensing application. In practical, graphene has been used to detect changes in aqueous media level. A graphene field effect transistor response is achieved through direct exposure to aqueous media or by top gating

through electrolyte solution. Here, we report on the electrical behavior of the as transferred graphene to SiO_2 substrate in deionized water (DI) and NaCl. The measurements were taken after dipping the sample in DI water and NaCl/DI water respectively. In this work we show that graphene can be used as ion sensitive graphene field effect transistor without using top gating via "solution gating" solution-gate field effect transistor (SGFET). Instead, back gated graphene field effect transistor is adopted in this study which require no further treatment or fabrication processes.

4.1.2 Results and Discussion

It is observed that the neutrality point is shifted negatively. Dirac voltage increased from 15 V to 23 V after dipping the sample for one second. Then followed by a continued decrease with time until it reached 22 V after 15 seconds as shown in Figure 4.1. This shift is due to electrostatic fields induced by the H_2O dipole moments and resulted in hole (increase of hole carriers) doping of the graphene after one seconds however the doping profile after one seconds demonstrating that electron concentration is increasing after one seconds. This can be seen from the upshift of dirac voltage. The change of dirac voltage is indicating that graphene surface adsorbed more H_2O molecules leads to a change in graphene carrier concentration near Fermi energy level. We observed that the value of the current tends to saturate as time increased. This phenomenon comes in agreement with what has been observed in [34]. However, the time response could be attributed to substrate/ graphene interface property. The effect of H_2O adsorbents on graphene surface is investigated for different gate lengths. It is observed that dipping the sample in DI water would affect graphene channel instead of graphene edges as the percentage change of 10V gate over drive resistance is increasing with time as shown in

Figure 4.2. After that, we prepared NaCl solution with varying concentration of NaCl ranging from 0.03 g to 0.5 g diluted in 200 mL of DI water. Transfer characteristics as a function of NaCl concentration is shown in Figure 4.3. The obtained I_d-V_g curves showing an I_{on}/I_{off} ratio of ~ 2.5 before dipping the sample in NaCl solution. The ratio decreased with increasing the concentration of NaCl as we introduce more ions that affect the conductivity of graphene channel eventually leading to a change in carrier concentration. Figure 4.4, demonstrates the dirac voltage as a function of NaCl concentration. Dirac voltage decreased from 32 V to 10V. Dirac voltage decreased monotonically from 32V to 10V. Since there is only a negative shift in V_{dirac}, graphene surface is more sensitive to Na^+ ions rather than H^+ ions as can be evidenced from the down shift of dirac voltage that exceeded the original state of carrier concentration. In addition, the pragmatic change in in the overdrive gate resistance suggests that the effect occur in graphene channel and graphene edges simultaneously as illustrated in Figure 4.5.

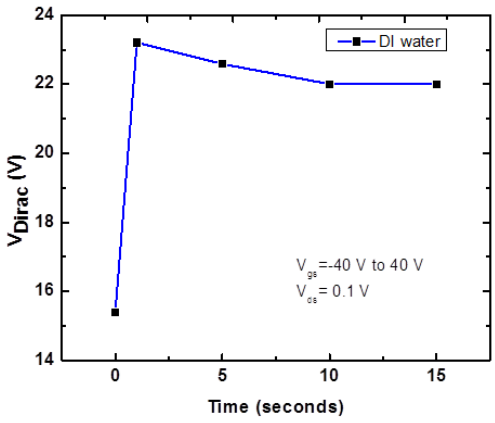

Figure 4.1. Voltage at minimum conductivity (dirac voltage) as a function of time in DI water. it is shown that graphene dirac voltage increased after one seconds from ~15 V to ~23 V then decreased steadily until it reached 22 V.

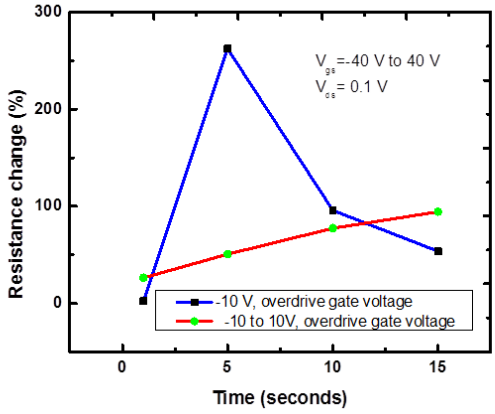

Figure 4.2. The percentage change in resistance as a function of time for DI water. Two lines are plotted representing the resistance of -10 V gate over drive voltage (blue) and 20 V gate over drive voltage taken from -10 V to 10 V (red). The blue line is showing the change in resistance at contacts interface while the red line indicates channel resistance. Contacts/graphene interface found to be more sensitive to the perturbation caused by H_2O molecules rather than graphene channel as can be seen.

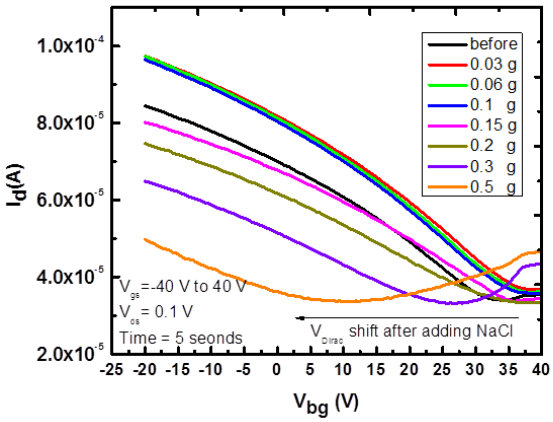

Figure 4.3. Id-Vg curves as function of NaCl concentration measured at 5 seconds, 100 mV drain to source voltage and -40 V to 40 V back gate voltage. The downshift of dirac voltage (to left direction) showing that graphene is exhibiting n-doping as more positive ions (Na^+) are introduced in the solution eventually affecting carrier concentration near neutrality point. Other trend can be seen in the minimum conduction (vertical shift), decreased conduction (increase in neutrality resistance) is observed as NaCl concentration increased

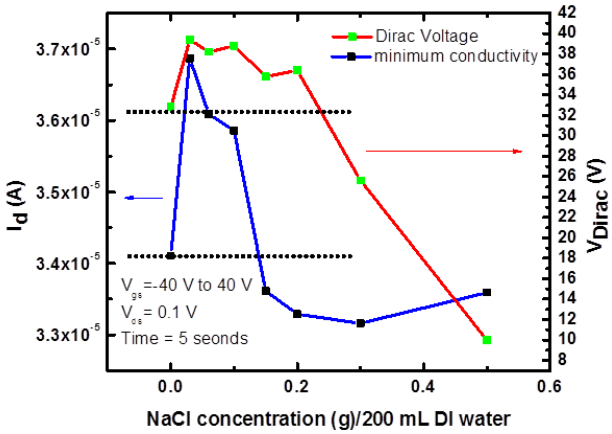

Figure 4.4. Minimum conduction current and dirac voltage as a function of NaCl concentration. Blue line is representing the change in minimum drain current whereas red line is showing the change in dirac voltage. Minimum current decreased at a concentration higher than 0.03 g then increased after introducing 0.3 g of NaCl. dirac voltage is decreasing linearly with NaCl concentration. The two dash lines representing the original state of minimum condauctivity and dirac voltage respectively. Increasing NaCl concentration leads to a change that surpassed the original state indicating stronger n-doping profile compared to dionized water.

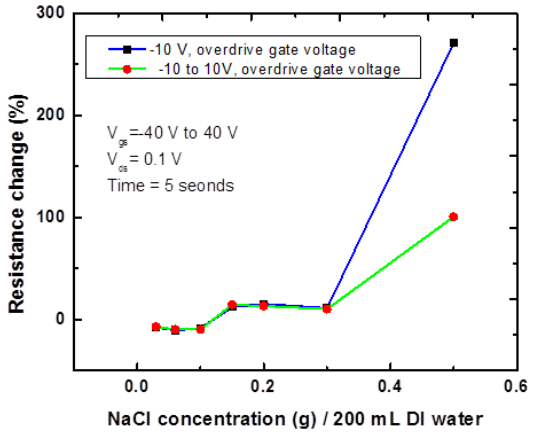

Figure 4.5. The percentage change in resistance as a function of time for NaCl concentration. Two lines are plotted representing the resistance of -10 V gate over drive voltage (blue) and 20V gate over drive voltage taken from -10 V to 10 V (green). The blue line is showing the change in resistance at contacts interface while the green line indicates channel resistance. It is observed that NaCl attacking graphene at both

contact/graphene interface and channel simultaneously as can be evidenced from the two lines that following the same trend.

4.1.3 Conclusion

We demonstrated graphene back gate transistor response as a new method that can be used as an indicator of water quality. We found that dipping graphene in deionized water would render the graphene doping profile as n-doping after time increased. Although the dirac voltage is been reduced, the electrostatic potential induced by water molecules is exceeding the original state of carrier concentration. On the other hand, graphene back gate Response exhibited strong n-doping characteristics after introducing variant NaCl concentration in deionized water for 5 seconds as can be seen from the down shift of dirac voltage. Interestingly, water molecular found to be occurring at graphene channel whereas it is affecting both graphene channel and graphene contacts. It is to be noted that the presented study is conducted for SiO_2 dielectric and it is anticipated that changing the substrate will significantly change situation as adsorbed molecules positioned in defects and create additional electrostatic potential leading to a change in the coupling between dielectric and graphene channel.

4.2 Graphene Behavior at High Temperature

This work has been submitted as **Qaisi, R. M.**, Smith, C. E., & Hussain, M. M. (2014). Atmospheric pressure chemical vapor deposition (APCVD) grown bi-layer graphene transistor characteristics at high temperature. *physica status solidi (RRL)-Rapid Research Letters*.

Also, the choice is made for this paper to be a cover page.

4.2.1 Introduction

Wide band gap semiconductors like gallium nitride (GaN) and silicon carbide (SiC) are currently employed in high temperature power transistor applications owing to their superior combination of characteristics including mobility, breakdown voltage, cutoff frequency, and operating temperature [35]. However, fabricating these devices using high vacuum epitaxial growth techniques (i.e. molecular beam epitaxy, MBE or metal organic chemical vapor deposition, MOCVD) is often cost prohibitive. Recently, high mobility graphene transistors have exhibited cut-off frequencies in the GHz regime suggesting that they are promising candidate for future low cost RF electronic applications [36]. At the same time, graphene's superior thermal conductivity and thermal stability has also been established. The high sensitivity of graphene surface to minor changes has opened the door for novel graphene sensor devices to be used in harsh environments such as ultra-clean energy storage plant, advanced combustion fuel cells, gasification, chemical looping and other applications [37]. These applications require

monitoring different gaseous species such as carbon dioxide (CO_2), ammonia (NH_3), nitrous oxide (NO_x) and sulfur dioxide (SO_2) in high temperature environments. Graphene field effect transistors (GFET) have shown promising results for detecting the absorbance of CO_2, NO_2, NH_3, SO_2 and O_2 gas molecules [38,39]. In a typical graphene FET sensor, graphene is used as a conducting channel between drain and source electrodes with the gate potential being applied through back-gate. Changes in the local electric field near the exposed graphene channel due to physisorbtion of molecules from the environment which alters conductance in the graphene channel. However, the behavior of graphene devices needs to be evaluated at elevated temperatures in order to understand the full impact and potential of low cost gas sensors for harsh environment applications. Therefore, graphene FET functionality at high temperatures is worth investigation to better conceive novel implementation of this new generation advanced material in harsh environment applications. Recently, graphene functionality at higher temperatures has been reported for mechanically exfoliated [40,41], epitaxial graphene growth [42] and suspended graphene [43]. Interestingly, most of these studies focus on the metal-graphene interface. It is widely observed that the metal contact interface would degrade the performance of the graphene due to the diffusion of metal grain boundary at high temperature. However, the studies on mechanically exfoliated graphene and epitaxially grown graphene were challenging. Mechanically exfoliated graphene does not offer an industry friendly path to scalable deposition whereas epitaxial graphene is expensive as a direct synthesis approach. Hence, it is of great importance to study the reliability, robustness, and device failure parameters in order to realize graphene device potential as a sensor in sensitive harsh environments. Therefore, we investigate the characteristics of

atmospheric chemical vapor deposition (APCVD) grown bilayer graphene transistors fabricated on ultra-scaled (10 nm) high-k dielectric aluminum oxide (Al_2O_3) at elevated temperatures. We observed that the drive current increased by >400% as temperature increased from room temperature to 250 °C. Low gate leakage was maintained for prolonged exposure at 100oC but increased significantly at temperatures >200 °C. These results pro-vide important insights for considering chemical vapor deposition (CVD) graphene on Al_2O_3 for high temperature applications where low power and high frequency operation are required.

4.2.2 Fabrication

Graphene was grown by previously mentioned process in chapter 2. Then, Poly methyl methacrylate (PMMA) based transfer of the graphene to heavily doped Si wafers coated with 10 nm atomic layer deposited (ALD) Al_2O_3 high-k dielectric was followed by deposition and patterning of 50/200 nm Ti/Au source/drain contacts deposited via e-beam evaporation.

4.2.3 Results and Discussion

Raman spectroscopy (532 nm laser wavelength) was used to evaluate the synthesized multi-layer graphene by the aforementioned process. Figure 4.6.a, Raman spectra acquired before and after transfer indicate no damage to the bilayer graphene due to mechanical handling. Also, large area Raman mapping of the I_{2D}/I_G peak ratio was acquired to validate the reliability of the graphene transfer process. The D band is centered around 1355 cm^{-1} indicating low disorder induced-defect. The G and 2D bands are positioned at ~1389 cm^{-1} and 2704 cm^{-1}, respectively. The Raman spectrum revealed an intensity ratio of ~2.5 and asymmetric 2D peak with full width at half maximum

(FWHM) of ~70 cm^{-1}. The observed characteristics of Raman spectra features is in agreement with Bilayer graphene characteristics in [44-47]. Moreover, the absence of D band peak is illustrating low deficiency nature of the grown bilayer graphene. In addition, raman spectra taken randomly from different spots to confirm similar characteristics are obtained (Figure 4.6.b). Different spectra shown in Figure 4.6.b, the revealed raman characteristics is comparable to the aforementioned features, with I_{2D}/I_G intensity ratio ranges from 1.4 to 4.1, G band and 2D band positioned in the range 1583.2 cm^{-1} and 1588.9 cm^{-1} respectively, FWHM of 2D band lies in the range 38 cm^{-1} to 55 cm^{-1}.

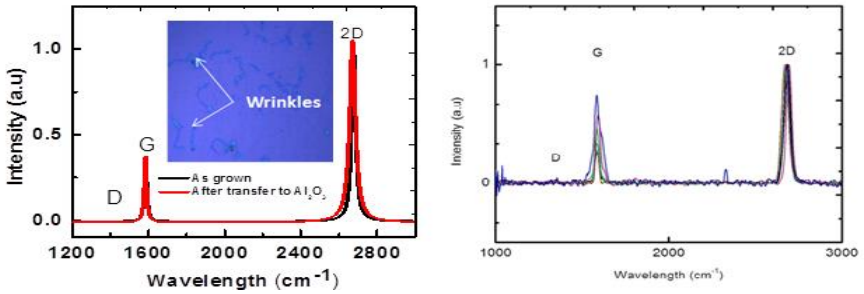

Figure 4.6. Raman spectra for as grown graphene film and after transfer. (a) Raman signatures of graphene film on Cu foil and after transfer to Al2O3 dielectric. I_{2D}/I_G is ~2.5 indicative of large area BLG. The inset shows an optical image of the transferred graphene with arrow indicating wrinkles which occurred during the transfer process. (b) Raman spectra taken randomly from different spots. The figure reveals I_{2D}/I_G ratio ranges from 1.4 to 4.1, G band and 2D band cantered between 1583.2 cm^{-1} and 1588.9 cm^{-1} respectively and FWHM of 2D band widths between 38 cm^{-1} to 55 cm^{-1}.

Raman spectroscopy (532 nm laser wavelength and 1 µm spot size) mapping technique of I_{2D}/I_G intensity ratio accompanied with FWHM mapping of 2D mapping is utilized to validate the reliability of graphene transfer process and evaluate the uniformity of the grown graphene film. Figure 4.7, represents the result of the performed Raman mapping. Figure 4.7.a, shows mapping of I_{2D}/I_G intensity ratio, graphene transfer process

yielded good graphene coverage on Al_2O_3 as elucidated from I_{2D}/I_G map with ratio varies from 0.5 to 3.5. Although the map shows that the majority of the transferred graphene film retains intensity ratio I_{2D}/I_G comply with graphene film with less than three layers [48,49], FWHM map of 2D band must be correlated with I_{2D}/I_G intensity map to quantify graphene layer numbers distribution across the film [50]. Figure 4.7.b, demonstrates FWHM of 2D band for the same map area shown in Figure 4.7.a. FWHM of 2D band range started from 35 cm^{-1} to 70 cm^{-1} with the majority band lies between ~40 cm^{-1} (blue) and ~45 cm^{-1} (green). Comparing I_{2D}/I_G intensity ratio map to 2D band FWHM map, unveil excellent agreement between I_{2D}/I_G ratio and FWHM widths that larger peak widths are associated with smaller intensity ratios. Also, from Figure 4.7.a and Figure 4.7.b, taking I_{2D}/I_G above 1 along with FWHM of greater than 30 cm^{-1}, we concluded that the grown graphene film is bi-layer graphene with high uniformity. Although the film signature is predominantly bi-layer graphene, areas that resemble multilayer graphene were present and found to be caused by large but isolated wrinkles in the graphene – a byproduct of a much stronger surface adhesion between the graphene and Al_2O_3 than we typically observe for SiO_2 dielectric based back-gated substrates [48-05].

Transfer characteristics of the graphene devices at elevated temperature are shown in Figure 4.8.a. A pronounced increase in the drive current alongside a reduced I_{ON}/I_{OFF} ratio as a function of temperature is attributed to thermal excitation of carriers leading to higher occupation of the available density of states. Since Raman spectra indicate that the synthesized grahpene is bi-layer, it is safe to believe in alignment with previous reports on bi-layer graphene exhibiting an increased carrier density with temperature rise leading to higher occupation of the available density of states in graphene [51].

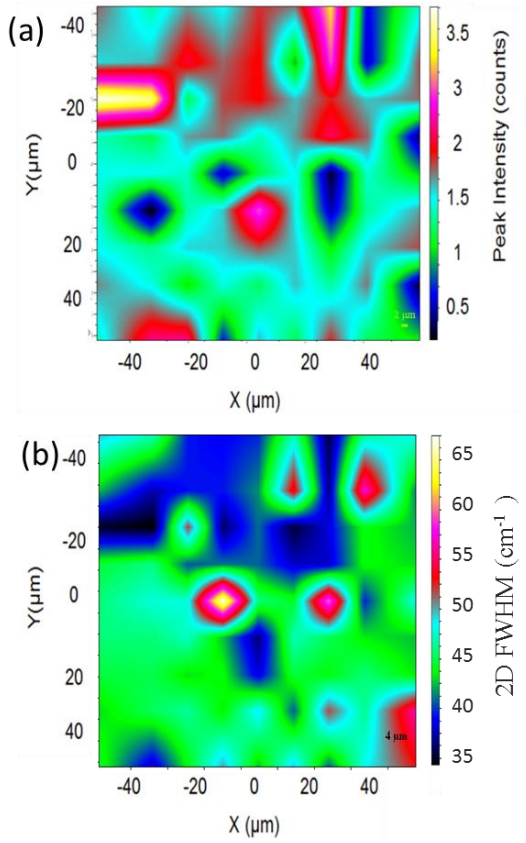

Figure 4.7. Raman mapping for large area (40 μm2) graphene on SiO2 to validate graphene transfer process and evaluate the uniformity of the grown films. (a) I_{2D}/I_G intensity ratio map with large graphene coverage possessing ratio of greater than 1 predominantly. (b) FWHM of 2D band map revealing the majority of 2D peak widths lies in the range from 40 (blue) cm^{-1} to 45 cm^{-1} (green).

Figure 4.8.a, the observed change in carrier density is ~ 60 % increase from room temperature to 76 °C according to previous works [52-54]. In our work, intrinsic carriers are estimated to increase by 80% compared to that of room temperature as the temperature reaches 250 °C. The stepwise increments are as follows: 60% additional carriers are excited as the temperature reached 50 °C followed by 15%, 4%, 1% and 1% for the next steps of 100 °C, 150 °C, 200 °C and 250 °C respectively. This increase in the carrier

density manifests itself as an observed increase in the drive current (I_{ds}). Therefore, the drive current increment by ~75% at 250 °C compared to that of the room temperature is in good agreement with the expected carrier density increase. It is also observed that the minimum conductance (conductivity at $V_g=V_{dirac}$) is increasing with temperature which explain the reduction in I_{ON}/I_{OFF} ratio. Eventually this trend defines the upper limit at which the device still can be switched between on and off states. Figure 4.8.b, shows the corresponding I_d-V_g curves of a back gated graphene transistor measured at room temperature before and after being exposed to a 250 °C environment. It is found that the device has ~10 % increased drive current post high temperature exposure. We attribute this increased performance to thermal annealing which removed impurities at the S/D contacts thus enhancing the drive current by reducing contact resistance (a known issue for graphene devices in general). It is important to note that the increasing conductance behavior with temperature that we observed is markedly differs from monolayer graphene where mobility is known to degrade with temperature due to dominance of surface/interface phonon rather than coulomb scattering [55,56]. A verified model is used [19,20] to extract the effective mobility based on total device resistance with fitting parameters of contact resistance (60–75% of the total device resistance), intrinsic carrier concentration (10^{12} cm^{-2}), and mobility (9000 cm^2/V-s). It is found that the carrier concentration increased from 1.42 x 10^{12} cm^{-2} at room temperature to 8.4 x 10^{12} cm^{-2} at 250 °C with corresponding mobility of ~9000 cm^{-2}/V-s and ~12,500 cm^{-2}/V-s, respectively. Figure 4.8.c, shows the extracted values of mobility and carrier concentration as a function of temperature. The pronounced increase in both mobility and carrier concentration with temperature agrees with observations by other groups.

Enhanced screening by the thin Al_2O_3 dielectric is primarily responsible for mitigating mobility degradation in these devices. The temperature effect is promising for this particular device embodiment since mobility in bi-layer is dominated by coulomb scattering rather than different scattering mechanisms (i.e. phonon scattering) [57].

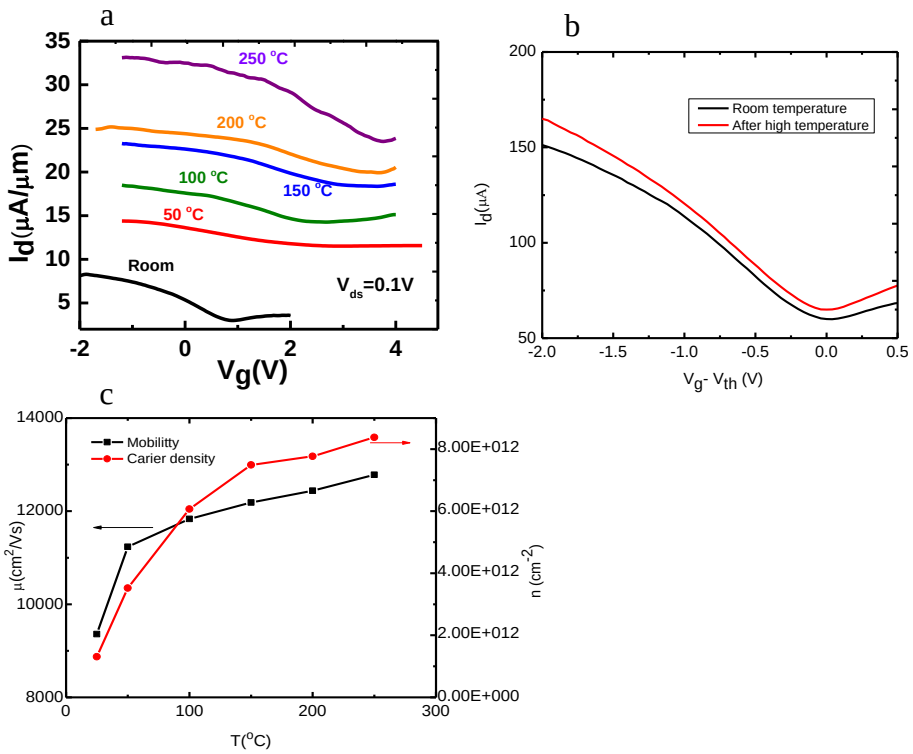

Figure 4.8. The transfer characteristics plot (Id-Vg) as a function of temperature. (a) Gate overdrive (V_g-V_{dirac}) normalized I_d-V_g plot showing increasing drive current with rising temperature along with increasing of the minimum conductance (I_d at dirac voltage); (b) The corresponding I_d-V_g curves of a back gated graphene transistor measured at room temperature before and after being exposed to a 250 °C environment. It is observed that the drive current is enhanced by ~10%; (c) The extracted values of mobility and carrier concentration as a function of temperature. It is illustrated that mobility is increased with temperature with increasing carrier density

The linear increase in I_{ds} shown in Figure 4.9 persists to 250 °C but is not solely due to increased gate overdrive (V_g-V_{dirac}) from the positive shift in V_{dirac} since the curves clearly show saturation behavior. We attribute this trend to temperature induced

elimination of negatively charges defects (i.e. V_O oxygen vacancies) at the BLG/Al_2O_3 interface whose elimination renders V_{dirac} more positive and at the same time reduces coulomb scattering. Moreover, the interface between gold (Au) and graphene leads to difference in work function between them, where the higher work function combined with the non-reactive nature of Au leads to higher probability of carrier transmission through the interface. Dirac voltage shift and I_{on}/I_{off} ratio as a function of temperature is shown in figure 4.10, implies that the device operation stabilizes after a relatively mild vacuum treatment at 50°C. We do not expect any effect from physiosorbed water since the V_{dirac} shift is moving in the wrong direction.

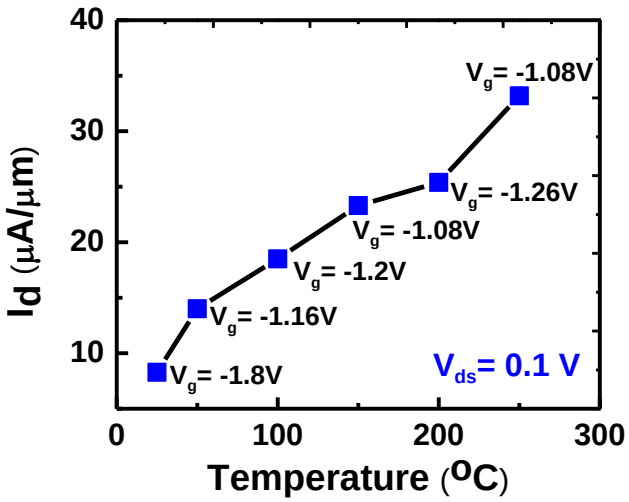

Figure 4.9. Drain current as a function of temperature. The monotonically increasing current with temperature is due to the increased density of carriers by thermal excitation.

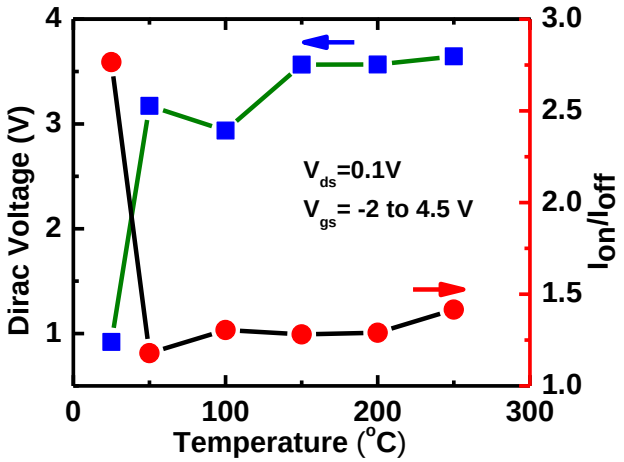

Figure 4.10. Dirac voltage and Ion/Ioff ratio as function of temperature. Stabilization of these device metrics occurred after a modest anneal at 50 ˚C. [V_{ds} = 0.1V, V_{gs} = -2 to 4.5V]

Exposure to elevated temperature showed a detrimental effect on the gate current density seen in Figures 4.11.a-c, a condition that could cause significant joule heating further affecting the changes we propose at the BLG/Al_2O_3 interface. Figure 4.11.a, shows the I_d-V_d plot of the device at different temperature as a function of time. The drain current increased as temperature increases compared to room temperature current.

The measured drain current has increased ~ 51% from room temperature to 100 °C after 40 minutes compared to ~68% increase in the current from room temperature to 200 °C after 15 minutes. However, this trend tends to affect the gate leakage current as shown in Figure 4.11.b. To investigate the gate leakage trend, a thermal budget measurement is acquired for the device at 100 °C and 200 °C respectively for 40 minutes. For both temperatures, the devices showed a pronounced increase in the leakage current after 30 minutes. Further measurement on gate current leakage was carried out at elevated temperature as shown in Figure 4.11.c. Here, the devices preserved low and steady gate leakage current up to 200 °C. This can be interpreted as an introduced vacancy to the

high-k dielectric due to the increased temperature. In addition, Al_2O_3 dielectrics exhibit Frenkel–Poole emission [58] where the dielectric gradually becomes a conductive as the temperature increases. The increased temperature gives rise to additional thermal energy that aids carriers in transitioning from localized states to the conduction band. The trapped carriers with sufficient energy to overcome the barrier offset or tunnel through the barrier manifest themselves as exponentially increasing leakage current.

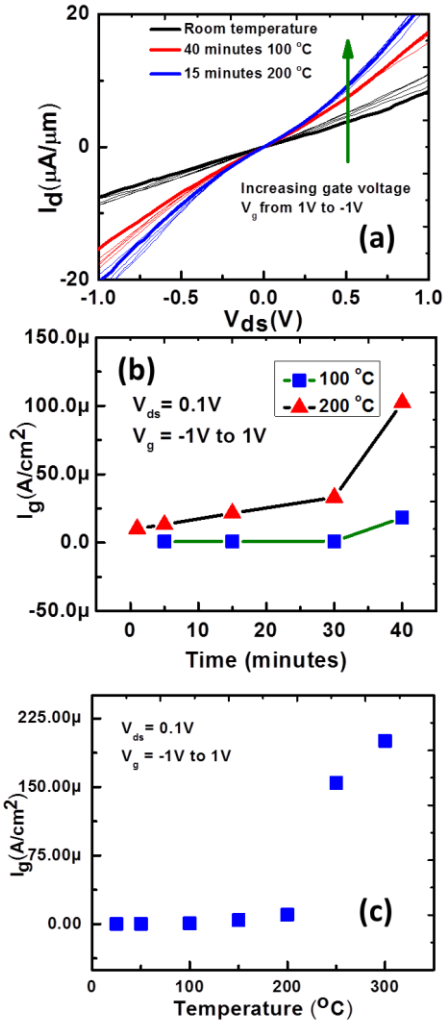

Figure 4.11. Leakage current analysis and failure data. (a) Width normalized I_d-V_{ds} plot for 100 °C and 200 °C respectively compared with room temperature. The gate modulation is much less effective at higher temperatures where the applied field cannot reduce the number of thermally excited carriers owing to graphene's small band gap. (b)

Area normalized gate leakage after extended time at 100 ˚C and 200 ˚C. The device at 100 ˚C generally suffered no degradation with time but leakage increased dramatically at 200 ˚C until the device suffered breakdown. (c) Width normalized gate leakage as a function of temperature. The gate leakage increase observed here implies that graphene transistors operating above 200 ˚C would need thicker (>10 nm) dielectrics to reduce gate leakage.

4.2.4 Conclusion

We have reported on APCVD grown graphene behavior at elevated temperature up to 300 °C. Gate leakage current was found to be the principal cause of device failure at high temperature above 250 °C suggesting that dielectric engineering and device isolation would improve functionality at higher temperatures above 300 °C. It is remarkable to note that these low band gap devices survived gate current densities as high as 1 A/cm^2 and channel current densities as high as 1 MA/cm^2 at 250 ˚C while still maintaining transistor functionality. Additional efforts aimed at measuring GFET response to different gases such as NO_2, CO_2, etc. at elevated temperature are needed to further define the application space based on sensitivity. The presented data demonstrating the robustness of low voltage APCVD GFETs utilizing ultra-high-κ scaled dielectric at elevated temperature highlight their potential as low cost alternatives to current GaN and SiC power transistors for use in harsh environments.

4.3 Micro Bio Fuel Cells.

4.3.1 Graphene Based Electrodes

This work has been submitted as Mink, J. E., **Qaisi, R. M.**, & Hussain, M. M. (2013). Graphene-Based Flexible Micrometer-Sized Microbial Fuel Cell. *Energy Technology*, *1*(11), 648-652.

This work has been submitted as Mink, J. E., **Qaisi, R. M.**, & Hussain, M. M. (2013). Graphene-Based Flexible Micrometer-Sized Microbial Fuel Cell. *Energy Technology*, *1*(11), 648-652.

4.3.1.1 Abstract

Microbial fuel cells harvest electrical energy produced by bacteria during the natural decomposition of organic matter. We report a micro-sized microbial fuel cell able to generate nanowatt scale power from microliters of liquids using a sustainable design comprised of atmospheric pressure chemical vapor deposition grown graphene on nickel thin film as anode, air cathode and a polymer based substrate platform for flexibility. Our demonstration provides a low-cost option to generate useful power for lab-on-chip applications as well as rapid screening for scaling up large-scale microbial fuel cells for water purification without consuming excessive power (unlike other water treating technologies).

4.3.2 Energy Harvesting

This work has been submitted as Mink, J. E., **Qaisi, R. M.**, Logan, B. E., & Hussain, M. M. (2014). Energy harvesting from organic liquids in micro-sized

4.3.2.1 Abstract

Micro-sized microbial fuel cells (MFCs) are miniature energy harvesters that use bacteria to convert biomass in liquids into usable power. The key challenge is transitioning laboratory test beds into devices capable of high power with readily available fuel sources. Here, we show a pragmatic step in advancing MFC applications through the fabrication of a uniquely mobile and low cost micro-sized device that can even be fueled with human saliva. The 25 μL MFC was made with two-dimensional atomic crystal structured anode material, graphene, for efficient current generation and an air cathode to enable the use of oxygen in air, making its operation completely mobile and free of the need for laboratory chemicals. With saliva as a fuel, the device produced higher current densities (1190 A/m^3) than any previous air-cathode micro-sized MFCs. The use of the graphene anode generated 40 times more power than that possible with a carbon cloth anode. Additional tests using acetate, a conventional organic material, at high organic loadings comparable to those in saliva demonstrated a linear relationship between organic loading and current. These findings open the door to saliva-powered applications of this fuel cell technology for Lab-on-a-Chip devices or portable point-of-care diagnostic devices.

Chapter 5. Graphene For Medical Purposes

With over 5% world population suffering from diabetes, invasive processes to analyze blood are used for daily monitoring of diabetes. Although reliable and comparatively economical, development of a more pragmatic and low-cost technology for non-invasive monitoring of diabetes is critical. In that regard, graphene for non-invasive glucose monitoring is demonstrated using non-functionalized graphene in the first section. Then, we show with clinical data from real diabetes patients that graphene based sensor can use saliva or sweat as specimen to analyze and fairly accurately predict the diabetes level on a daily basis with high sensitivity, selectivity, response time and refresh rate.

5.1. Non-Functionalized Graphene Based Bio-Electronic Sensor

5.1.1. Introduction

Graphene and other two dimensional (2D) atomic crystal materials have emerged with unique properties such as high speed charge transport, mechanical strength, thermal conductivity, etc. Graphene is of particular interest as the first 2D material with a single layer of carbon atoms packed in 2D honeycomb lattice. The 2D carbon material possesses low energy dynamics of electrons with low thickness ~2Å offering fast heterogeneous electron transfer.[60] Graphene is semi-metallic with zero band gap exhibiting high

transport rates and micrometer scale mean free path. The 2D atomic crystal structure of graphene makes it favorable for sensing application because it provides high surface area combined with its ability to adsorb different molecules eventually impacting the channel conductance.[61]In that regard, graphene and graphene oxide (GO) have received a great attention in developing biosensors owing to its biocompatibility,[63]high surface area,64 excellent conductivity, ease of functionalization and production.[65]Several groups have investigated GO electrodes and graphene composites for glucose detection.66-68Glucose sensors based on graphene materials are developed using two approaches: (i) graphene and graphene modified films utilized as a channel material to be activated through top gate;[69,70] (ii) employing graphene or graphene oxide composites as electrodes.[70-73] Nonetheless, functionalization of graphene surface is required for efficient glucose detection. This is done by introducing different molecules to graphene film that leads to catalyzing glucose oxidation process eventually changing graphene conductance. On the other hand, developing graphene composites as electrode material is dependent on redox solution ability to oxidize glucose thus releasing more electrons in the solution to be collected in that electrode. The recent development in glucose enzymatic and non-enzymatic types of sensors shows that defects present in synthesized graphene plays an important role in the process of modifying graphene surface.[74]However, common and serious problems about the glucose oxides are the price and insufficient long-term stability. Also, it can be easily affected by temperature, pH value, humidity and toxic chemicals, due to the nature of enzymes.[75] In addition, enzyme activity is affected by process complexity of adsorption, cross-linking, entrapment and electro polymerization to immobilize enzymes on solid electrodes.[76]

Here we show glucose detection based on double layer graphene grown via atmospheric pressure chemical vapor deposition (APCVD) through modulating channel conductance by water and glucose molecules with respect to their adsorption behavior to change the electronic structure of graphene film. Manipulation of graphene conductance by physisorption of molecules on top of graphene channel and semiconductor materials is simple and well-studied approach.[77-90] Our results indicate that graphene channel conductance is significantly changed after introducing water (H_2O) molecules and glucose molecules into graphene channel. In the case of graphene field effect transistor (figure 5.1.a), H_2O and glucose molecules are adsorbed on top of graphene channel. The positively charged physisorped molecules produce gating electrostatic potential effect that transduced into a readable signal in the form of a noticeable change in the electrical characteristics through the ultra-scaled dielectric and the 2D grown graphene. Furthermore, those molecules changes doping profile of the graphene by adding additional positive net charge. The mechanism of graphene electrical doping is well studied.[91-93]Electrical doping is achieved through changing gate potential which in our case is represented by electron transfer between graphene and the adsorbed molecules on graphene surface illustrated as a change in the Fermi level energy of the graphene. (Figure 5.1.b), shows the change of graphene Fermi level energy as a function of adsorbed molecules related to graphene Dirac point.

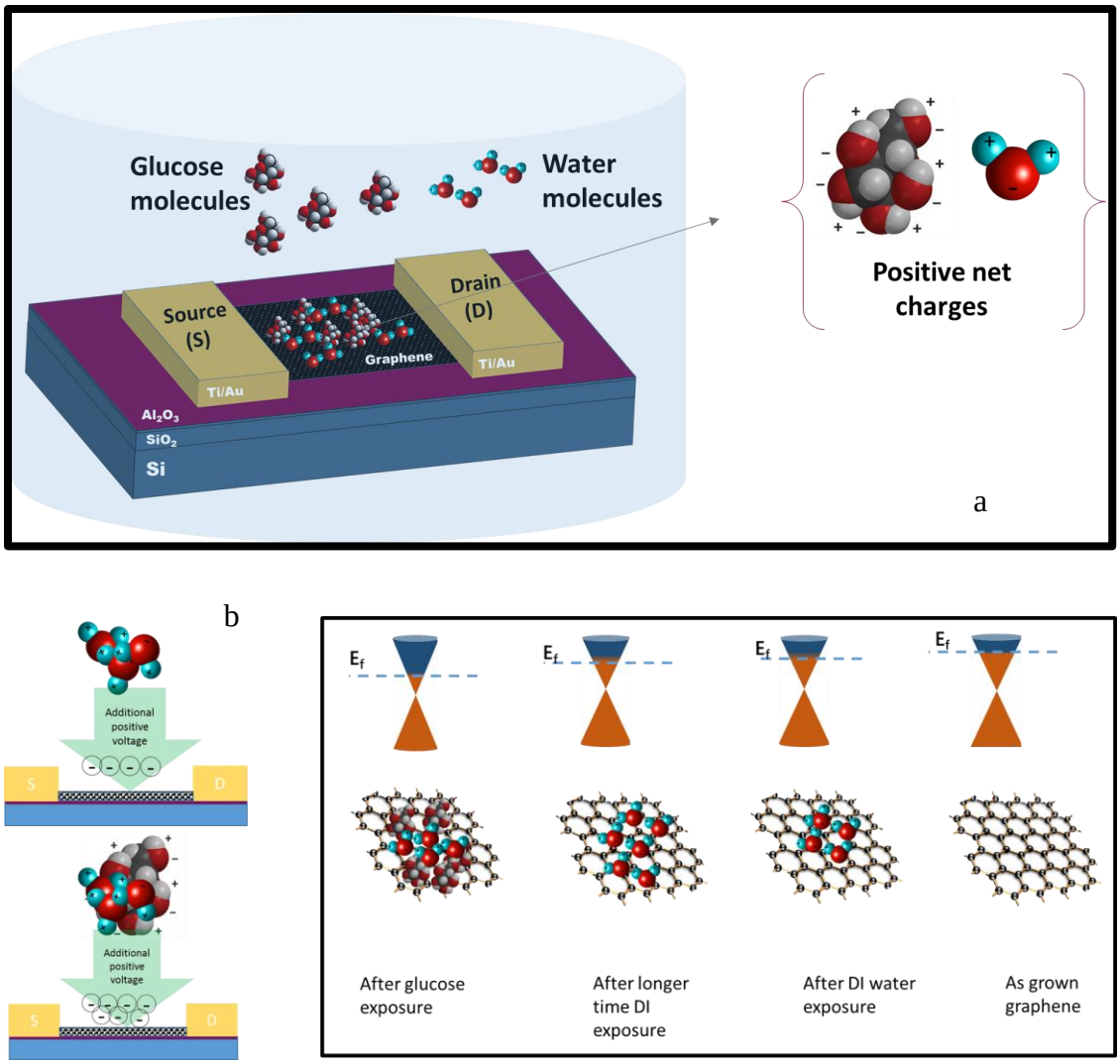

Figure 5.1. Device schematic and fermi level manipulation by charge molecular transfer . a, general device schematics showing the device under water/glucose treatment with the arrow indicating a sample of water/glucose molecules possessing positive total net charges. b, energy fermi level representation of the graphene under the influence of water/glucose molecules.

5.1.2. Experiment

For experiment of sensing functionality, first we analyzed performance characteristics of as fabricated graphene devices in DI water with time for different gate length values. It is observed that the Dirac voltage point is down shifted over time for the

measured devices. Also, performance parameters such as (channel resistance and I_{ON}/I_{OFF}) were extracted from I_d-V_g plot. Upon analyzing performance parameters over rinse time step ranging from 1 second to 30 minutes, we concluded that observed changes are stable with time as it can be seen from the three gate lengths measured devices namely 12 µm, 14 µm and 20 µm. After that, glucose was diluted in DI water for different concentration (5 mM, 10 mM, 15 mM and 20 mM) followed by measuring the I_d-V_g plots of the 20 µm gate length device as it shows the highest sensitivity to DI water due to the larger area offered along graphene channel device. The same analysis was repeated to investigate the sensing properties of the device after introducing DI water.

Water was obtained using Milli Q water purified system provided by Milipore with resistivity of 18.2 MΩ.cm at 25 ºC. The pH value delivered by the tool is around 6.4 and remained the same through the experiment. The experiment was conducted by first pouring the water from Mili-Q machine then rinsing the device for the allotted time step. For time step that is larger than 5 seconds the bottle that is containing the DI water/glucose was covered with glass until it is rinsed for the specified time step. Also, the water was only used once.

5.1.3. Results and Discussion

We start with analyzing the nature of graphene film. Raman spectroscopy (532 nm laser wavelength and 1 µm spot size) mapping technique of I_{2D}/I_G intensity ratio complemented with FWHM mapping of 2-D band was utilized to validate the reliability of graphene transfer process and was also used to evaluate the uniformity of the grown graphene film (Figure 5.2.a). Graphene transfer process yielded good graphene coverage on Al_2O_3 as elucidated from I_{2D}/I_G map with ratio varies from 0.5 to 3.5 with majority of

the I_{2D}/I_G lies in the range from 1 to 2 indicating that the number of graphene layer(s) are consistent to the characteristics of less than three layers of graphene films previously reported [93-95]. Figure 5.2.b, demonstrates FWHM of 2D band for the same map area shown in Figure 5.2.a, FWHM of 2D band ranges start from 35 cm^{-1} to 60 cm^{-1} with the majority band lies between ~40 cm^{-1} (green), ~45 cm^{-1} (cyan) and ~50 cm^{-1} (red). In order to quantify graphene number of layers distribution across the film, correlation between I_{2D}/I_G intensity ratio and FWHM map was evaluated. Comparing I_{2D}/I_G intensity ratio map to 2D band FWHM map, unveils excellent agreement between I_{2D}/I_G ratio and FWHM widths that larger peak widths are associated with smaller intensity ratios. Also, from Figure 5.2 (a and b), taking I_{2D}/I_G above 1 along with FWHM of greater than 30cm^{-1}, we conclude that the grown graphene film is double layer graphene with high uniformity. Although the film signature is predominantly double layer graphene, areas that resemble multilayer graphene were present and found to be caused by large but isolated wrinkles in the graphene – a byproduct of a much stronger surface adhesion between the graphene and Al_2O_3.[96] In addition, Raman spectra taken randomly from different spots to confirm similar characteristics are obtained (Figure 5.2.c). Different spectra shown yields Raman characteristics comparable to the aforementioned features, with I_{2D}/I_G intensity ratio ranges from ~ 0.5 to ~ 4.4, G band and 2D band positioned in the range 1582.2 ±5 cm^{-1} and 2686.9 ±5 cm^{-1} respectively, FWHM of 2D band lies in the range 40 cm^{-1} to 60 cm^{-1}. The acquired Raman spectra illustrating different graphene layers number ranging from multi-layer graphene (gray), double layer graphene (red, green and light cyan) and single layer graphene (yellow). The observed characteristics of

Raman spectra features are in agreement with double layer graphene characteristics as a majority of the film.[97-101]

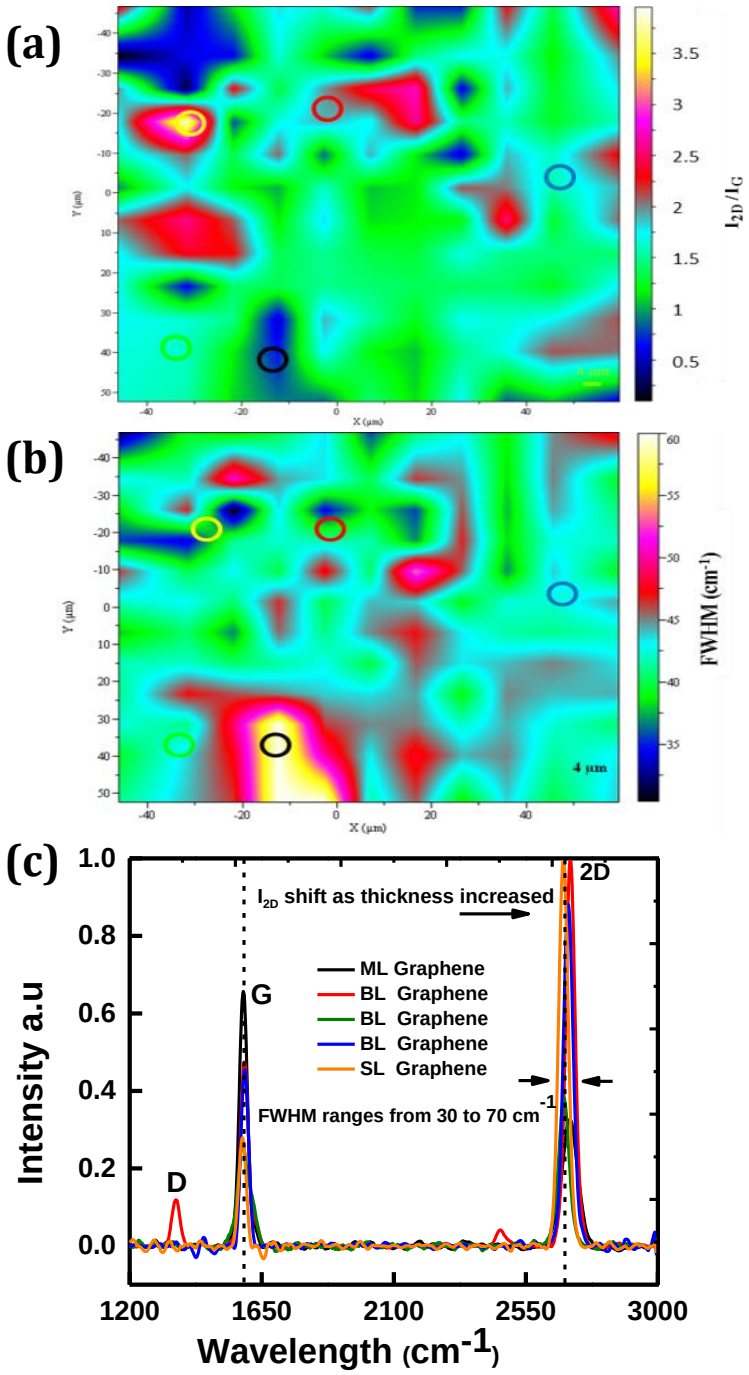

Figure 5.2. Raman spectroscopy mapping of I2D/IG with Raman spectra acquired from the same area. a) I_{2D}/I_G ration map shows that the majority of the film has intensity ratio from ~1 to ~2.5. b) FWHM mapping of the same area comparing I_{2D}/I_G

and FWHM maps indicate that for intensity ratio larger than 1 preserve FWHM larger than ~40 cm^{-1} which is a feature of double layer graphene. c) Raman spectra obtained randomly from the same mapping area to demonstrate the different Raman signatures variation among different combinations of intensity ratio and FWHM. The colored circles on the maps show the positions at which Raman spectra were taken.

Electrical measurements of the same devices before and after different time periods of rinsing in deionized (DI) water were carried out at room temperature (Figure 5.3). It is important to understand how the experimental sensor response to DI water only. The substrate is used as global back gate biased between ±1 V, while the Ti/Au contacts are biased at 0.1 V representing the source-drain voltage. The Dirac voltage at which the device delivered minimum conduction for the as-fabricated back gated double layer graphene transistor was found to be ~ 0.8 V for different gate lengths showing p-doping behavior under ambient conditions. This p-doping characteristic is attributed to the introduction of impurities such as oxygen, moisture or defects in the fabrication process.

To examine the doping effect of H_2O molecules on graphene channel, the devices are rinsed in water then dried using nitrogen (N_2) followed by measurements after each rinsing step. The observed shift in the Dirac voltage is indicating a change in graphene electronic properties due to physisorption of H_2O molecules on graphene channel which is directly related to graphene Fermi level energy. When impurities through fabrication process are present in graphene channel active area, the resulted device is p-doped when back gate electrode was biased. Hence, opposite potential (positive) is required to restore the Dirac point back to zero state. This reflects the positive charge nature of H_2O molecules to drive the device neutrality toward less voltage. As a result of water molecules treatment, the devices exhibited n-doping effect (increase in electrons carrier

concentration) as noted from the down shift of minimum conduction voltage. Since source/drain contacts were not covered, the charge impurities introduced in both channel active area and contacts led to a change in both energy levels. This plays an important role because the modification of contact Fermi level will extend to graphene's energy level as well. The accumulation of H_2O molecules on graphene channel builds up more positive charge eventually producing a capacitance between graphene and top molecular charges. Figure 5.3,a, shows transfer characteristics of 12 μm gate length. It is found that the Dirac voltage is reduced by ~55% after rinsed in water for 30 minutes with channel conduction remains insensitive to increasing rinse time period. Also, the device with 14 μm gate length preserves a reduction of ~43% in Dirac voltage with channel resistance increased from 864 to 920 Ω after 1 minute then saturated at that value (Figure 29(b)). On the other hand, for 20 μm gate length device, Dirac voltage is upshifted by ~53% while channel resistance being increased with time (Figure 29(c)). It is to be noted, the devices show less vertical shift in the minimum conduction current. To conclude, we find that H_2O molecules adsorbents on graphene lead to n-doping effect. Gate length has low impact on doping behavior whereas channel sensitivity is affected. Larger gate lengths found to be more sensitive due to larger exposure area.

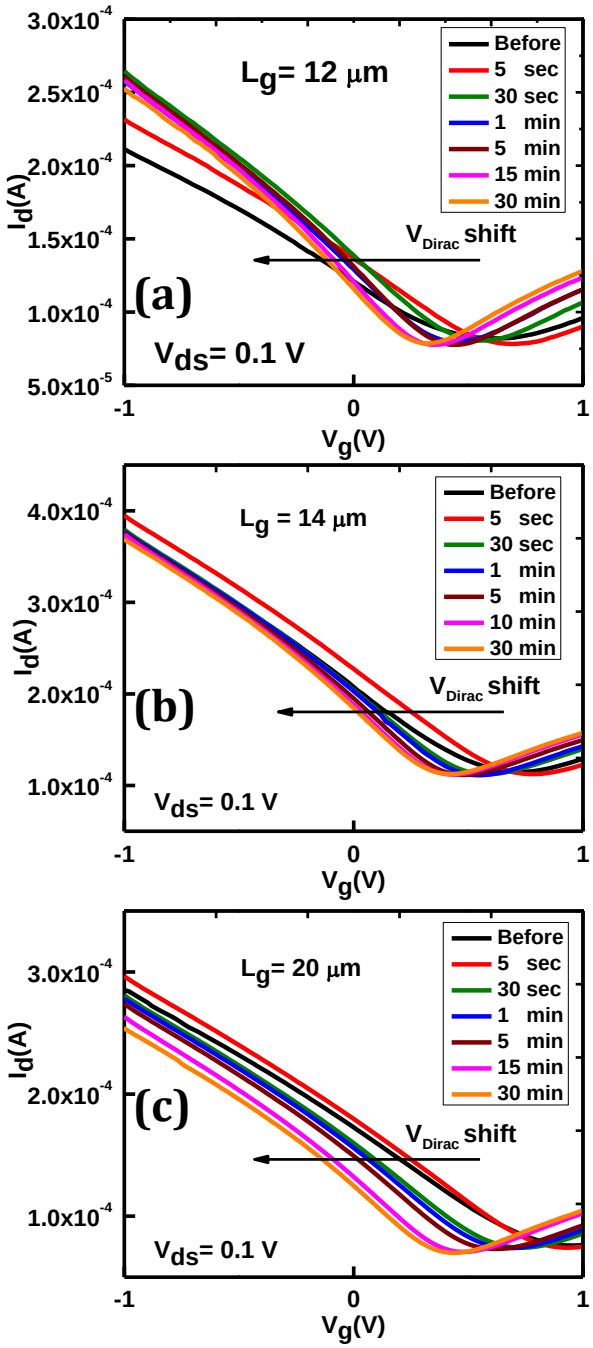

Figure 5.3. Transfer characteristics curves (Id-Vg) as a function of time in DI water for different gate lengths. a) I_d-V_g curves of 12 μm gate length indicate that the device neutrality point is shifting towards less voltage values (to the left). b) 14 μm gate length curves exhibit the same neutrality point shift toward less voltage. Both devices (12 and 14 μm gate lengths) are showing the same trend from the perspective of neutrality point where the minimum voltage increased slightly after 5 seconds then decreased steadily

afterward. c) I_d-V_g curves of the 20 μm gate length device show continuous decrease of minimum voltage point.

In order to understand the effect of H_2O molecules on graphene channel conductance, further evaluation of extracted parameter from transfer (I_d–V_g) characteristics is plotted in Figure 5.4. As a result of the higher sensitivity of the 20 μm gate length toward H_2O molecules, from now until the end of the paper we will focus on the 20 μm gate length device. Dirac voltage is found to decrease steeply after 5 seconds (Figure 30(a)). This reduction is caused by the induced electrostatic potential from physisorption of H_2O molecules on top of graphene channel leading to a change in electrostatic coupling between charges on top of graphene surface and graphene/dielectric interface occurs. The coupling phenomenon is much stronger for thinner dielectrics as reported in the past.[102, 103] The shift of neutrality voltage toward less voltage is reflecting the nature of the positive H_2O charges as mentioned earlier. To evaluate the increased electron carriers produced after deionized water, channel resistivity versus time is plotted (Figure 5.4.b). The observed increase in channel resistance is attributed to the induced charge impurities after rinsing in deionized water combined with coupling between graphene surface charges and back gate external applied electrostatic potential. We found that channel resistance increased linearly after 30 seconds by 0.045 Ω/second. Although the channel resistance decreased after 5 seconds then increased again, could be due to the stability of charge generation process at small time periods. While increment is estimated to be from increased carrier concentration in graphene channel which directly impact channel resistance rather than contact resistance. It is to be noted that the channel resistance is extracted from the I_d-V_g plots by taking the resistance difference of highest

contact value and lowest resistance value in which the device functioning properly (i.e. between Dirac point and voltages less than +1 V). It is also possible that contact resistance might be affected due to exposure of stimuli like DI water or glucose. Nonetheless we focused on the overall impact in the channel which can be read for sensing a change in the device functionality. To ensure high precision of our device, I_{on}/I_{off} ratio as a function of time period is plotted (Figure 5.4.c). The measured device maintained I_{on}/I_{off} ratio between 3.7 and 4 through different time rinsing demonstrating high quality back gate graphene transistor comparable to top gated or electrochemically gated bio sensors.[70] The device is then kept for three hours inside a vacuum furnace for resetting and removal of the adsorbed molecules (data not shown).

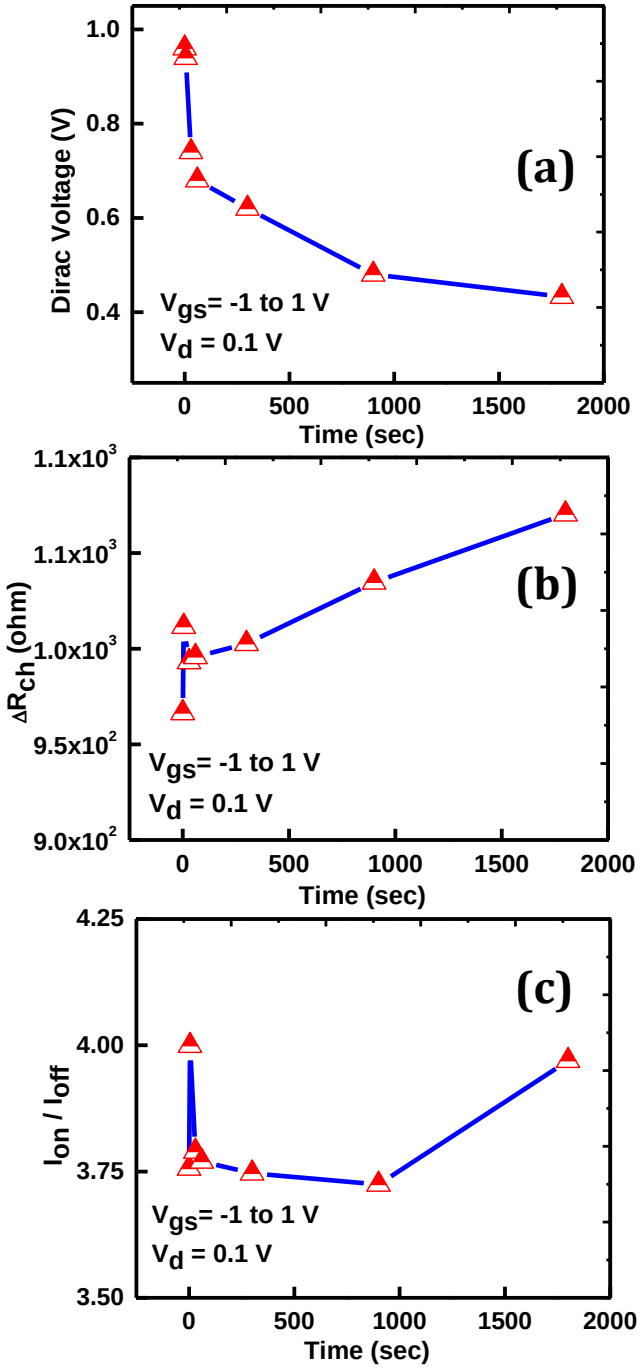

Figure 5.4. Extracted parameters form transfer curves of the 20 □m gate length transistor. a) Dirac voltage as function of time illustrating that Dirac voltage is decreasing sharply until 1 minute while decreased slowly after that. b) Channel resistivity

as a function with time shows a linear growth after 5 seconds. c) I_{on}/I_{off} ratio as a function with time shows that the device maintained ratio in the range of ~3.7 to ~4 indicating high performance of the device and distinguishable on and off states.

Next glucose is diluted in DI water at different concentrations namely 5 mM, 10 mM, 15 mM and 20 mM. It is to be noted, that this molar ranges cover most of the diabetes detection references. Electrical measurements are performed on the 20 μm gate length transistor in two time steps rinse (5 seconds and 5 minutes) at room temperature to evaluate the effect of adding glucose molecules on graphene channel (Figure 5.5). After 5 seconds (Figure 5.5.a), increasing glucose molecules started to induce more charges leading to more n-doping effect as can be noted from the upshifting of Dirac voltage by ~ 65%. The minimum conduction voltage reached a value of ~0.26 V indicating higher carrier concentrations than observed under DI water. The minimum conduction current is changed vertically imposing prominent change in graphene active area resistance where current decreased from ~28 μA to ~10 μA at a rate of 1 μA/glucose mM. This change is more pronounced at higher glucose concentration as a result of the incorporation of higher charge transfer that is affecting the electro-coupling state between graphene/dielectric and graphene/top molecules. After 5 minutes (Figure 5.5.b), Dirac voltage is following the same observed trend after 5 seconds, however the reduction in Dirac voltage found to be ~60% at a value of ~0.2 V at higher rate which can be ascribed by the intensification of glucose carriers. Also, the minimum conduction value is decreased with higher glucose concentrations at approximately the same rate. To conclude, the higher glucose concentration leads to more n-doped behavior and

substantial decrease of channel resistivity. Interestingly, at higher glucose concentration the device starts to display more hole conduction than those observed under deionized water demonstrated from the upshifting of Dirac voltage after 5 seconds and 5 minutes at 20 mM and 15 mM of glucose respectively.

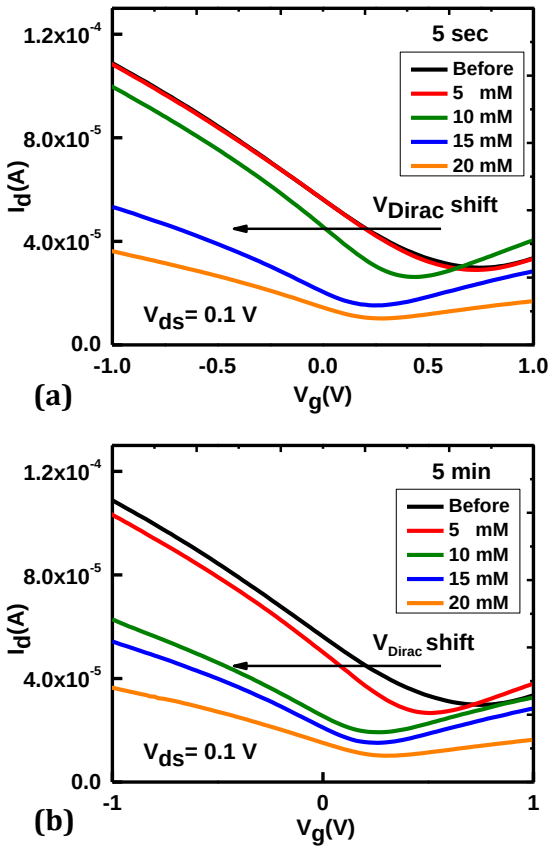

Figure 5.5. Transfer curves (Id-Vg) of the 20 □m gate length transistor as a function of glucose concentration taken at 5 seconds and 5 minutes respectively. a) Transfer curves after 5 seconds reveal two obvious trends. First, the Dirac voltage is decreasing as glucose concentration increased. Second is vertical downshift of the minimum conduction current. b) The transfer curves after 5 minutes of the same device show the same observed trends at 5 seconds. The observed downshift of Dirac voltage for both measurements (5 seconds and 5 minutes) indicates the n-doping effect after glucose was introduced while the vertical downshift of minimum conduction current is directly related to minimum carrier concentration at Dirac point.

To study the effect of glucose concentration on electronic properties of the grown double layer graphene channel, extracted parameters from transfer curves are plotted in Figure 5.6. The change in Dirac voltage is plotted against glucose concentration in Figure 5.6.a. The adsorption of glucose molecules on graphene can be evidenced from the decreased Dirac voltage after rising glucose concentration as indicated by red lines. This observation shows that strong local electrostatic potential is created from water and glucose molecules. We noticed that the Dirac voltage increased unexpectedly after introduction of 15 mM of glucose for 5 seconds (Figure 5.6.a), red lines with blue half-filled squares) while increased after introduction of 10 mM of glucose for 5 minutes (Figure 5.6.a), red lines with green half-filled circles). This observation shows that intensified glucose concentration is altering graphene doping profile from n-doped to p-doped as explained by the upshift of the Dirac voltage after adding 10 mM of glucose whereas after 5 seconds it occurs after adding 15 mM of glucose (i.e. longer exposure time leading to increased glucose molecules on graphene surface eventually changing the doping profile from n-doped to p-doped). The alteration in graphene doping is not attributed to glucose molecules accumulation only. Instead, doping profile due to water adsorbents is heavily relies on water molecule orientation, dipole momentum and substrate quality. In our case, we can attribute the alteration in doping profile to the fact that additional glucose concentration leading to a change in dipole momentum created by H_2O – glucose molecules impacting locally induced electrostatic potential. Likewise deionized water, glucose molecules induced positive charges that contributed toward reducing neutrality voltage. Channel resistivity as a function of glucose concentration along with I_{on}/I_{off} ratio is shown in Figure 5.6.b. We observe higher sensitivity of

graphene channel with respect to increased glucose concentration. For both measurements, channel resistivity is increased linearly with glucose concentration (Figure 5.6.b, purple lines with orange half-filled hexagons for 5 seconds and half-filled green triangle for 5 minutes). The sensitivity of graphene channel to glucose molecules can be calculated from the slope of each line. The obtained sensitivities in terms of graphene channel change in resistivity are ~197 Ω/glucose mM and ~189 Ω/glucose mM for 5 seconds and 5 minutes, respectively. The device preserved I_{on}/I_{off} ratio in the range from 3.2 to 4 is verifying high performance of back gate transistor compared to previously reported devices (Figure 5.6.b), red lines with blue half-filled squares for 5 seconds and black filled circles for 5 minutes). Table 5.1, shows a comparison of this devices with previously published devices.

Table 5.1. Comparison of this work with previously published sensors.

Ref.	Detection range (mM)	Selectivity	Sensitivity	Time response (sec)
Ref 11	3.3-10.9	H_2O_2 and glucose	N/A	180
Ref 15	2-10.1	H_2O_2 and glucose	30 µA/mM/cm^2 @ 50 mV cycling	2
Ref 13	0.1 - 10	N/A	110 µA/mM/cm^2 @ 1 V cycling	N/A

Ref 8	28 mM/mm^2	N/A	8.045 □A/mM/cm^2	600
Ref 12	0-4	glucose and glutamate	0.5μA/μM	40-500
Ref 16	0.2-2.5	oxidization function group and glucose oxidation	N/A	50
Ref 17	50 μM -4.5	N/A	1 A/0.025 mM @ 20 sec interval	2s - 20 s
This work	0-15 mM	H_2O and Glucose	180 Ω/mM	5 and 300

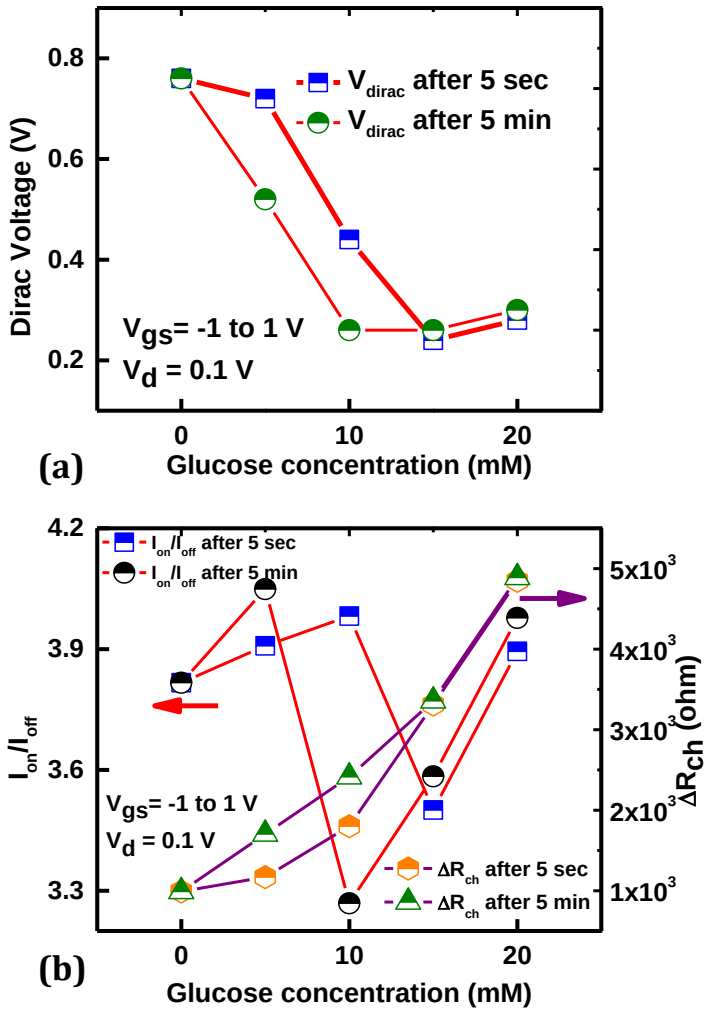

Figure 5.6. Extracted parameters from the transfer curves of the 20 µm gate length device as a function of glucose concentration for 5 seconds and 5 minutes, respectively. a) Dirac voltage exhibiting a pronounced alteration of the reduction trend. The change of Dirac voltage is correlated with a change in the electronic structure of the graphene. The device is showing n- doping characteristics as can be noticed from the decrease in the Dirac voltage however for both devices Dirac voltage increased after 15 mM of glucose was introduced for 5 seconds (blue squares) and after 10 mM of glucose was introduced for 5 minutes, respectively. The observed increase of the neutrality point is indicating that the device went through a change in doping profile from n-doped to p-doped structure. b) I_{on}/I_{off} ratio (red lines) and channel resistance (purple lines) as a function of glucose concentration. The device maintained a high performance as can be seen from the ratio that found to be between ~3.3 and ~3.9 for both measurements. On the other hand, channel resistance increased linearly at different rates for both measurements. 5 seconds data are represented by half-full triangles and 5 minutes data

are represented by half-filled hexagons, respectively. The sensitivity can be calculated from the slope of each lines and it is found to be ~197 Ω/glucose mM and ~189 Ω/glucose mM for 5 seconds and 5 minutes, respectively.

Although the adsorbent of H_2O and glucose molecules on graphene surfaces is evidenced from the induced shift in Dirac voltage which is a result of change in carrier concentration, these imposed changes in graphene electronic structure inherently make changes in graphene Raman modes.[104, 105] We employed Raman spectral analysis to verify the obtained doping profile from electrical measurement as shown in Figure 5.7. Raman spectrum was taken after each time period step measurement. Figure 5.7.a, demonstrates the effect of rinsing the device in DI water for several time periods. The G-band Raman frequency is downshifted as time decreased whereas 2D band frequency increased. The induced variations in our graphene devices are showing n-doping behavior as interpreted in previously published results.[70, 106] Also, a prominent decrease in I_{2D}/I_G ratio occurs as a result of the stiffening of the full width at half maximum (FWHM) of G-band. This can be attributed to the absence of external electrostatic potential which can have strong impact on 2D-band by inducing electrostatic coupling between graphene surface and the dielectric while G-band is more sensitive to additional change in electrons distribution on graphene surface.[86,107] The rendered n-doping profile is resulting from the introduced positive charge from H_2O molecules found to be affecting graphene electron structure electrostatically rather than dynamically by molecule charge transfer.[82, 86] Similarly, introducing glucose to the solution also resulted in increasing electron concentration (n-doping) in graphene as illustrated in Figure 5.7.b. However the trend is altered after 15 mM of glucose and 10 mM of glucose for 5 seconds and 5 minutes,

respectively where G-band start shifting downward while 2D band shifted in upward direction. The observed variation is designated a p-doping characteristics.[87] This change in the doping profile (p-doping) is in line with what we observe in Dirac voltage where the neutrality point can be reached in positive voltages. Overall, the observed broadening of the G-band peak and transforming into asymmetric peak observed at higher frequency is expected when graphene is in direct contact with ultra-scaled Al_2O_3 dielectric and it is attributed to the uniaxial strain.[108, 109] This high uniaxial strain is due to its larger coefficient of thermal expansion.[110] This phenomenon is observed at larger time step rinse in DI water and at higher glucose concentration. Therefore, we conclude that these variations are in agreement with the obtained electrical measurements and lead to confirm the n-doping behavior which resulted from introducing H_2O and glucose molecules into graphene surface.

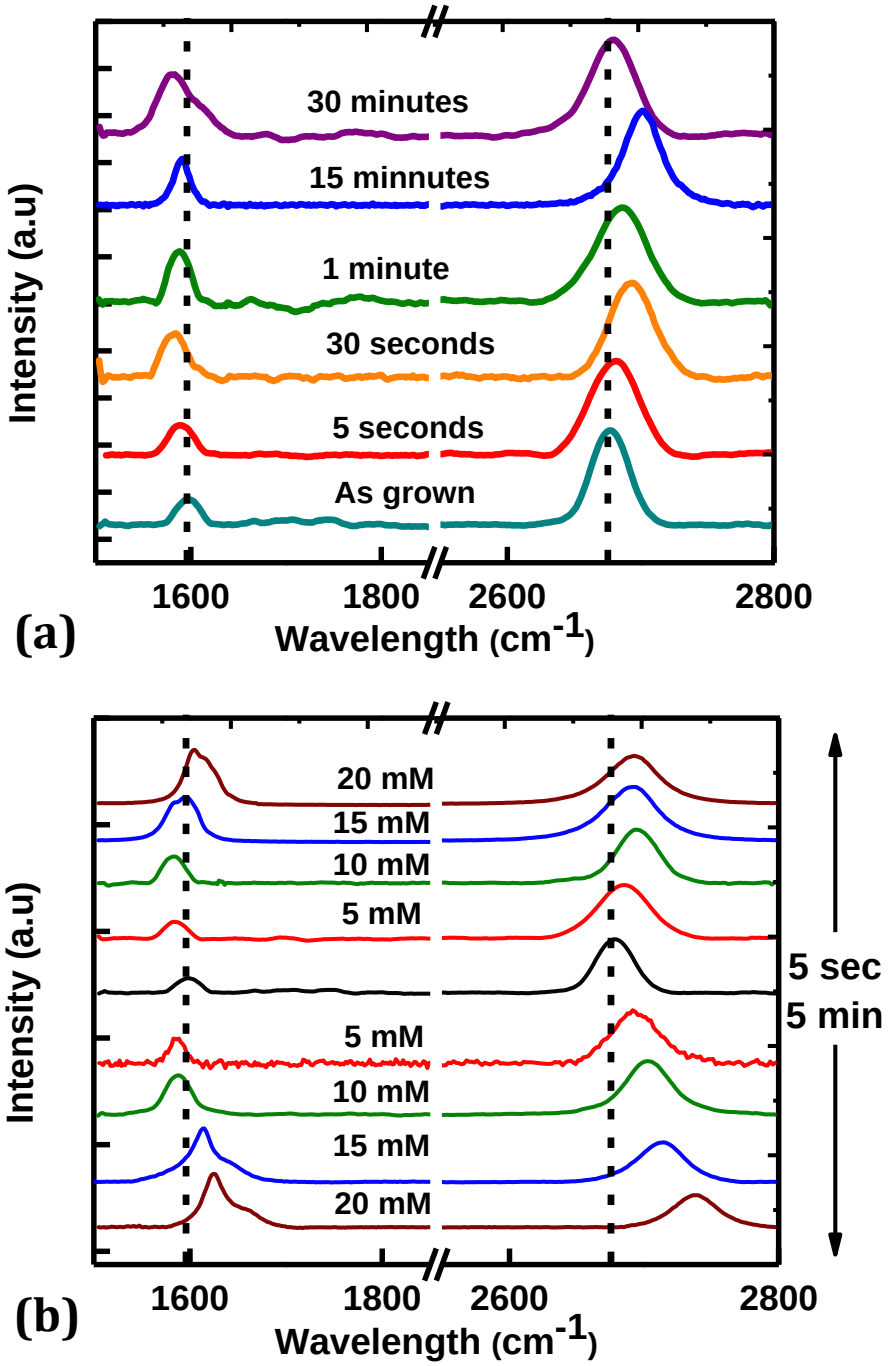

Figure 5.7. Raman spectra as function of time for DI water and for glucose, respectively. a) The G band peak is downshifted as rinsing time increased while 2D band peak is broadening revealing a n-doping behavior. b) G-band peak is downshifting for both time measurements while it is upshifted after 15 mM of glucose concentration and

10 mM of glucose concentration for 5 seconds and 5 minutes, respectively. The observed changes in Raman spectra indicate the alteration of doping profiles.

Further analysis of device selectivity was investigated by using the device in a strong ionic environment. Sodium chloride (NaCl) is used at different concentrations namely (0.06 g to 0.5 g) diluted in 100 mL DI water. Figure 5.8 shows the transfer (I_d-V_g) curves of the graphene back gate transistor for monitoring NaCl concentration. It is obvious that the Dirac point behaves differently than the case of glucose molecules. It is observed that NacL causes slight down shifting of the Dirac voltage while it is affecting channel conductance. The decrease in Dirac voltage found to be not exceeding 25% of the original Dirac voltage. It is anticipated that ionic solution does not have strong doping effect on the fabricated devices. The monotonic decrease in channel resistance indicates that the device is responding to the incremental change of NaCl concentration. Compared to glucose sensing, ionic solutions have more pronounced effect on graphene channel electronic properties without doping the graphene channel. On the other hand, glucose caused n-doping profile along with change in graphene channel resistance.

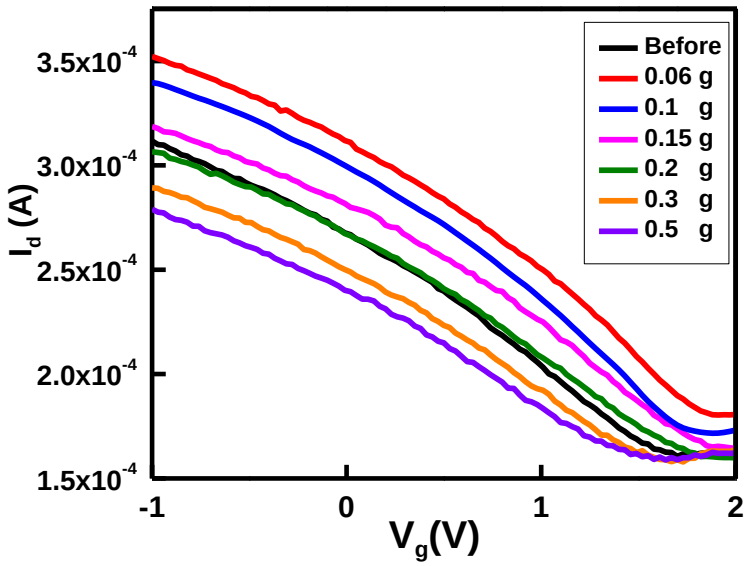

Figure 5.8. Selectivity measurements using transfer (Id-Vg) curves of the same device with the introduction of NaCl molecules diluted in DI water for five seconds. Two observations are noted: (i) curve steepness is decreased as NaCl concentration increased; (ii) slight down shifting of Dirac voltage which is estimated to be 25 % overall reduction.

5.1.4. Conclusion

In conclusion we have shown a simple method to fabricate atmospheric pressure chemical vapor deposition (APCVD) grown double layer graphene integrated back-gated transistor based bio-electronic sensor which for the first time does not need any functionalization of graphene. The demonstrated sensor is used to detect deionized water and glucose and it shows high sensitivity, fast response and ultra-low power operation. Compared to prior demonstrations, we show that glucose can be sensed via charge transfer from adsorbed molecules on top of graphene channel under source/drain biasing at a certain voltage combined with low sweeping bias of global back gate bias. Full

exposure of polymer free transferred APCVD grown double layer graphene with ultra-scaled high-k based global back gate biasing makes the fabricated sensor catalyzes such mechanism. Both water quality monitoring and glucose level detection for diabetic patients are directly needed to ensure a sustainable future. Access to a simple bio-electronic device like ours is a leap forward for advanced healthcare.

5.2. Clinically Trialed Graphene Based Sensor For Non-invasive Monitoring Of Diabetes

5.2.1. Introduction

Over 5% world population suffer from diabetes where due to absence or low level of insulin in the body, patients suffer from fatigue, exhaustion, frequent urination, severe craving for food and water, non-healed wound-bruise-tear, weight gain or loss, and many other health complications. Not only diabetes causes sufferings to patients, it poses financial burden on them and eventually raise the global healthcare cost. The most critical challenge diabetes patients face is it is a non-curable illness and the only way its consequences can be adverted is to monitor it on daily basis and then based on the insulin level in the body to manage that by physical exercise, diet, additional intake of insulin and such [111-113]. Therefore, monitoring of insulin level is a critical factor in diabetes management. Most of the commercially available technologies are invasive measurements through collection of blood samples in milliliter scale and then to analyze it [114-119]. Yet, researchers have continued their exploration for a non-invasive method based on near-infrared spectroscopy and transdermal measurement of glucose through

skin using the physics of light and photonics [120-122]. Another non-invasive test approach is to analyze urine samples [123,124] which need significant improvement in accuracy as (i) blood sugar level needs to be larger in order to be correlated with urine glucose level and (ii) often for some patients fasting before the test causes lack of enough urination for sufficient amount of sample [125].

Therefore, there is an open need for developing analysis techniques in which the patients remain in comfort while performing the test. As cited before, like urine there are various human extract live samples can be tested to find out a reasonable corroboration between insulin level extracted from such sample and the one measured by well-known traditional methods using blood samples. In this regard, saliva seems to offer interesting and unique results in conjunction with its easy availability in a non-invasive painless way [*126-134*]. Different materials and device configurations have been studied for such purpose based on glucose sensing which impacts body insulin level [135-137]. Majority of these studies are dealing with enzymatic reaction between active materials with precisely developed electrodes which eventually lead to the immobilization of the material of interest to be detected [138,139]. Nonetheless, this type of configuration depends heavily on the activity of the bio-reaction of those enzymes. Hence, the quest for developing non-enzymatic configuration of glucose sensors arose. The latter case led to the developments of non-enzymatic sensors based on metal electrodes to enhance the electrochemical responses of glucose oxidation [140-142]. These non-enzymatic sensors require catalysis and acceleration of oxidation reaction of glucose toward metal electrodes thus more electrons are released through the containing solution and sensed via the other electrode. Based on these early and some ongoing studies, recently, advanced techniques have been pursued

to produce gadgets which can detect glucose in human live samples such as tears, saliva, sweat, urine and blood serum [143-145]. Some of these developed gadgets are available commercially like the recently announced lenses for glucose detection [146]. Though these advanced techniques are capable of giving reasonably accurate results, they are expensive due to their sophisticated designs and costly manufacturing process. And thus we have focused to develop a non-invasive, low-cost, easy-to-use, low-voltage (so it can consume less power and becomes a mobile device) and accurate monitoring device for diabetes.

Graphene – the two dimensional atomic crystal structure material manifested itself as a promising candidate for biomedical sensors application owed to its extraordinary properties [147], high surface to volume ratio [148], excellent electrical conductivity and high electron mobility [149], small band gap potential [150], physical adsorption of different molecules [151,152]. Therefore, we use an atmospheric pressure chemical vapor deposition growth bi-layer graphene based back gate transistor integrated with ultra-scaled high-k dielectric aluminum oxide (Al_2O_3) for glucose level screening in human live samples. We chose bi-layer graphene due to its excellent surface uniformity enabling quality interfacing with Al_2O_3 high-k dielectric without compromising its intrinsic properties. The ultra-scaled dielectric allows for low voltage operation of the device eventually that leads to low-power operation as well as higher sensitivity due to of change in graphene channel conductance even with minute amount of sample (resulting in higher sensitivity) when it is exposed to deferent environments with maintaining the excellent conduction properties intact. These characteristics are of major importance for realizing low cost, high performance and non-invasive device for glucose detection in human live saliva samples.

5.2.2. Sample Preparation & Experimental Methodology

As part of sample preparation, we first deposited aluminum (Al) nucleation seeding layer using e-beam evaporation on heavily doped *(n^{++}, 0.005 Ω-cm)* 4" n-type silicon substrates. We grew 3-7 nm of Al. The seeding Al layer was completely oxidized in air during the vacuum break and transferring to atomic layer deposition (ALD) system. Yet, to complete the oxidation process, ALD process started with water (H_2O) cycle at elevated temperature. Next we used tri-methyl aluminum precursor as source of aluminum (Al) in conjunction with H_2O as oxidizer at 200–250 ˚C to deposit Al_2O_3 *(~10 nm)* with a deposition rate of ~1Å/Cycle. We synthesized graphene films at atmospheric pressure using copper (Cu) foil (99.8%, Alfa Aesar) as transition metal for nucleation site for graphene growth. This technique allows large *(moer than ~ 6 cm X 6 cm)* area graphene synthesis with high uniformity and controlled thickness. We started the process with cleaning Cu foils using Acetone, Isopropyl Alcohol (IPA) and then deionized (DI) water. Then, we dried the foil with *(99% pure nitrogen gun)* inserted inside a horizontal APCVD furnace. Then we ramped up the temperature of the system to 800 ˚C at a rate of 800˚C/min while flowing Argon (Ar) and Hydrogen (H_2) at 300 sccm and 10 sccm, respectively for initial Cu surface cleaning. As the next step, we raised the temperature to 1050˚C at 5˚C/min. Then, we kept the sample in a mixture of Ar and H_2 gases at the same flow rates for 30 min in order to remove oxygen and consequently stabilizing the surface of Cu foils. Next, we introduced Methane gas into the tube for 15 min at a flow rate of 300 sccm. Thereafter, we terminated the growth and the sample was quenched by moving the sample out the hot zone under the flow of Ar and H_2. The sample was next

cooled while the flow of Ar and H_2 continued. When the sample was completely cooled down to room temperature, using Poly methyl methacrylate (PMMA) we transferred the grown graphene to the previously prepared silicon substrate with already deposited Al_2O_3 [153]. Finally, Contact mask based liftoff lithography was utilized to pattern 50/200 nm Ti/Au source/drain contacts deposited via e-beam evaporation. Finally, a second mask was used to preserve graphene in the channel regions upon exposure to a short duration O_2/Ar reactive ion etch. We used Raman spectroscopy (532 nm laser wavelength) to evaluate the synthesized *(bi)*-layer graphene by the aforementioned process. Electrical characteristics of the *fabricated* back gated field effect transistor were studied using keithley 4-probe station at room temperature. (Figure 5.9.a) shows schematic of the fabricated device. The adsorption of water molecules and glucose molecules on graphene surface imply the transfer of charges into graphene channel which eventually affecting the electronic properties of graphene device (Figure 5.9.b).

a

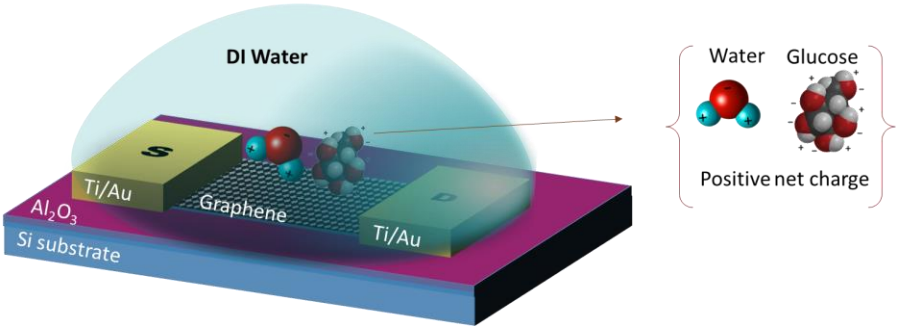

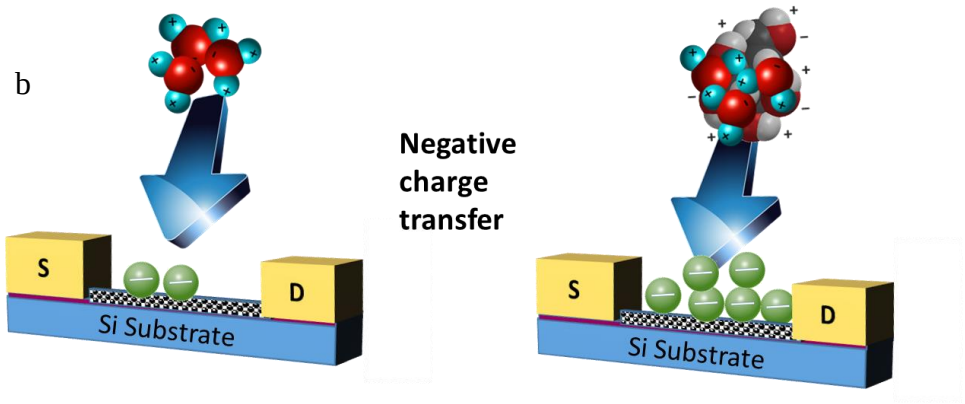

Figure 5.9. Schematics of the fabricated device after graphene transfer. a, shows the device in the presence of water droplet representing water (H_2O) and glucose ($C_6H_{12}O_6$) molecules charges (positive). b, water molecule charge effect on graphene sheet by allowing negative charge to transfer to graphene. c, glucose molecule effect on graphene sheet by allowing more negative charges to transfer into graphene channel.

After disclosing the purpose and then securing consent from the type-2 diabetes patients of *King Faisal Hospital*, Makkah, Saudi Arabia, we collected human blood and salivary samples on the same day and at the same time in an environmentally safe way. Our clinical collaborators conducted the blood sample analysis using standard pathological lab techniques to classify the type of their diabetes level and amount of insulin level. Saliva was collected after detailed information regarding food and fluid consumption prior to data collection. After that, saliva were collected in sterilized container by spiting method. Glucose level processing of saliva samples were conducted by using coloration and intensity approach of quinoneimine complex upon introducing glucose oxidase (GOD). Yet, the released H_2O_2 complex is peroxidase to releases quinoneimine complex. We performed the testing of salivary samples at the same time without any prior special treatment of the samples *after spiking the samples by direct*

injection with certain amount of glucose. The collected saliva samples were maintained at pH value of ~6. Table 5.2, summarizes the collected samples for this experiment.

Table 5.2. Clinically collected samples details

Sample number	diabite type	post meal	age	ethnicity	sex
1	2	yes	40	Asian-Saudi	male
2	2	yes	30	Asian-Saudi	male
3	2	yes	33	Asian-Saudi	female
4	2	yes	55	Asian-Bahrini	male
5	2	yes	21	African-Egyptian	female
6	2	yes	36	Asian-Saudi	male
7	2	yes	29	Asian-Saudi	male
8	2	yes	50	Asian-Saudi	female

5.2.3. Results and Discussion

For sensor characterization, we dropped 10 saliva samples on top of graphene devices. Next we left the devices inside the closed glass pockets for two different time slots: 5 seconds and 5 minutes, respectively. Figure 5.10, shows the experimental setup. Next we dried the devices in nitrogen environment before taking them Keithley probe stations for electrical measurements.

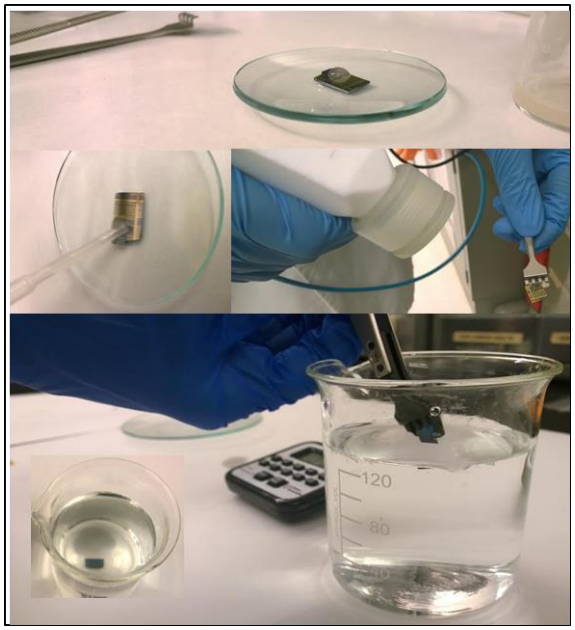

Figure 5.10 Experimental set up showing saliva droplets and water rinsed devices along with water/saliva residuals cleaning using nitrogen gun.

Figure 5.11, shows the optical image of the fabricated device and the corresponding Raman spectrum. In the Raman spectrum Figure 5.11.b, the D band is not present, indicating non-defective graphene. The G and 2D bands are positioned at ~1582 cm^{-1} and 2676 cm^{-1}, respectively. The Raman spectrum revealed an intensity ratio of I_{2D}/I_G >1 and asymmetric 2D peak with full width at half maximum (FWHM) of ~37 cm^{-1}, confirming the presence of bi-layer graphene [154-156]. Raman spectrum was also collected for entire graphene channel area to ensure that graphene film is uniform (Figure 5.11.c). The map revealed an intensity ratio of I_{2D}/I_G in the range of 1-3 along with FWHM of 2D-band peak in the range of 30 – 40 cm^{-2}. The acquired features of Raman map indicate that the graphene film is homogenously distributed across the device [157-160].

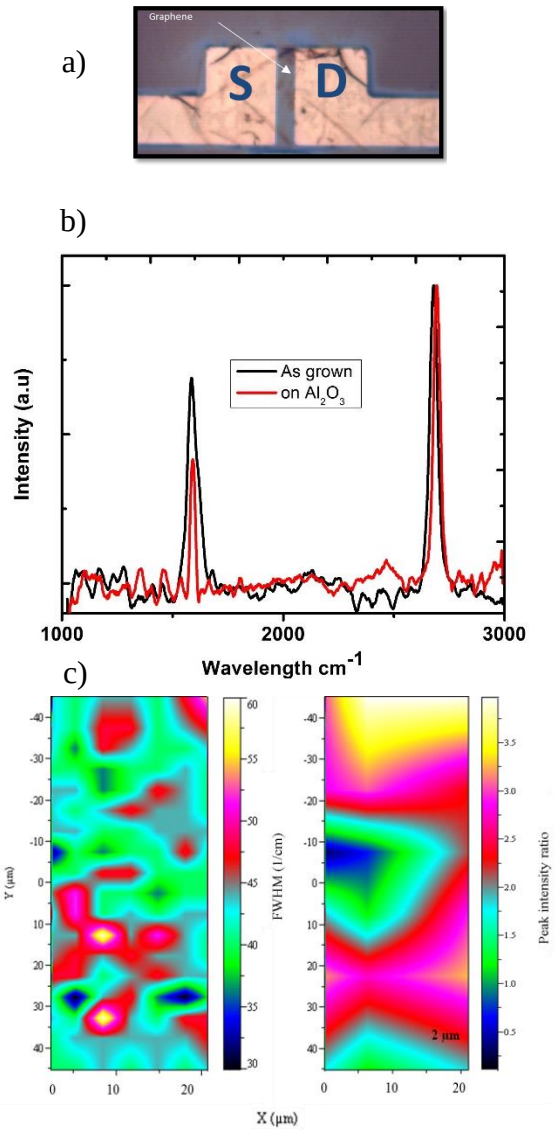

Figure 5.11. Optical image of the fabricated device combined with Raman signature spectral analysis of the grown graphene and Raman mapping. a, optical image of the device. b, Raman signature of grown graphene and after transferring graphene to Al_2O_3 substrate showing I_{2D}/I_G intensity ratio >1 with the absence of D-band peak indicating high quality graphene. c, large area Raman mapping with I_{2D}/I_G intensity ratio >1 along with FWHM lies in the range ~38 cm^{-1} to 50 cm^{-1} is demonstrating continuous large area bi layer graphene.

The back gated graphene transistor was evaluated as diabetes monitoring device based on its (graphene's) channel conductance variation upon the addition of pre-determined glucose concentration in the saliva samples. The change in graphene

conductance due to physisorped atoms on its surface is manifested through a change in the Dirac voltage point (minimum conduction voltage) [160]. The ID-VG characteristic curves are obtained for back gate graphene transistor with 20 µm gate length for 5 seconds and 5 minutes, respectively as shown in figure 5.12. After 5 seconds, we found that Dirac voltage is downshifted from 1 volt to 0.3 volt as glucose concentration increased from 2.04 mM to 2.096 mM as shown in Figure 4a. On the other hand, figure 5.12.b, shows transfer characteristic curves for the same device acquired after 5 minutes. In the latter case, the Dirac voltage is following the same trend noticed for 5 seconds however, the Dirac voltage was reduced from approximately 2 volts to 1 volt. The observed changes in Dirac voltage in both measurements are attributed to the induced electrostatic potential which is affecting the carrier concentration across graphene channel through the ultra-scaled Al2O3 dielectric resulting in additional positive charge coming from the adsorbed molecules glucose ultimately changing Dirac voltage [161,162]. Also, the witnessed monotonic reduction in the minimum conduction current is an evidence of the adsorbed particles on graphene channel hence reducing the conduction through the channel [163-165]. It is to be noted that for both cases, that addition of more glucose will lead to a small change in the minimum conduction current. This observed small change can be attributed to the saturation of graphene channel with more particles of glucose found in saliva.

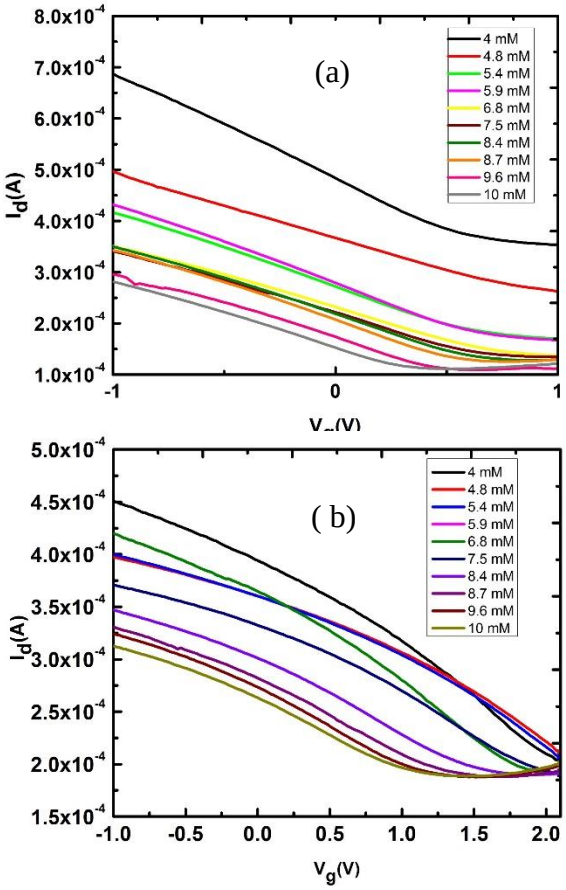

Figure 5.12. IdVg transfer curves for the fabricated device in the presence of incremental glucose level in the saliva. a, I_dV_g curves after 5 seconds is showing that the device channel conductance is rigorously deteriorated as glucose concentration increases. b, I_dV_g curves after 5 minutes is showing the same trend as in 5 seconds however the deterioration is more pronounced due to the larger window time allow or more glucose molecules to be adsorbed on graphene.

From the transfer characteristic curves for both cases, channel resistance is an extrapolated parameter representing the sensing variable in our study. The channel resistances were calculated as the change between maximum resistance and lowest resistance of graphene channel. Figure 5.13, shows the channel resistance as a function of glucose concentration in human saliva for both 5 seconds and 5 minutes. It is found that channel resistance change abruptly from ~260 Ω to ~ 600 Ω as glucose concentration increased for the measurement taken after 5 seconds while the change after 5 minutes was

modestly increased from ~ 220 Ω to ~ 250 Ω. The variation between both measurements can be explained as graphene channel reaching saturation to adsorb anymore molecules on its surface as concentration saturates. This can be seen from the extracted 5 seconds channel resistance abruptly changing compared to larger time window (5 minutes) which allows more molecules to be adsorbed on top of graphene channel leading to slow rate of channel resistance as a function of glucose concentration. From the channel resistance plot, sensitivity was calculated as the slope of each curve and it is found to be 54 Ω/mM and 13.5 Ω/mM for 5 seconds and 5 minutes, respectively. This portion of the study also infers that a responsivity of 5 seconds can be experienced in the demonstrated device which is completely competitive to any commercially available invasive methods.

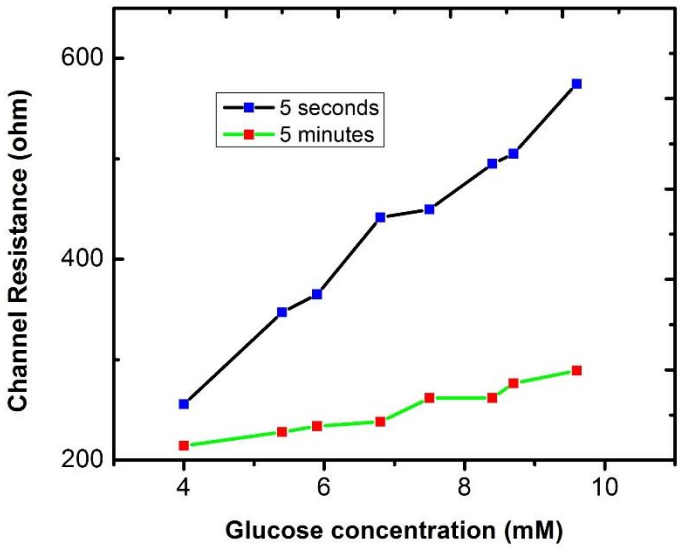

Figure 5.13. Extracted channel resistance from IdVg transfer curves for 5 seonds (blue squares) and 5 minutes (red squares) respectively as a function of saliva glucose concentration. The device response is steeper after 5 seconds as the channel is perturbed with glucose molecules while after 5 minutes the response is moderated.

We conducted density functional theory (DFT) calculation to understand the effect of water and glucose molecules relaxation on graphene surface. First, water adsorption on freestanding graphene with 4X4 supercell and 32 carbon atoms is simulated (Figure 5.14.a). The water molecules yielded a binding energy of ~30 meV indicating a physisorped H_2O molecules on graphene without changing graphene fermi level band energy. This result is showing that water adsorption on graphene has no doping effect. This comes in agreement with previous results (156,166). Though the simulation showed no doping effect in the case of water molecules it is found through our experimental measurement of graphene device with water molecules only that water can cause slight n doping effect as the rinsing time increased (i.e. increasing time eventually leads to increasing number of water molecules on graphene surface). Water molecules can cause a slight n-doping effect depends on water molecule orientation and clustering effect combined with the used substrate [167,168]. Second, mono-layer graphene and bilayer graphene with 4X4 supercell is simulated for fully relaxed glucose molecule on graphene surface (Figure 5.14.b and Figure 5.14.c). It is found that single glucose molecule affected graphene electronic properties by inducing a clear n-doping effect. This attributed to the positive charge of glucose molecule to causing a charge transfer from glucose molecule to the free standing graphene. In this case, glucose acts as a donor where highest occupied molecular orbital (HOMO) is above the Fermi level of the graphene for both cases. As a conclusion of DFT calculation graphene has went through chemical n-doping process in the mean of charge transfer from adsorbed molecules into free standing graphene.

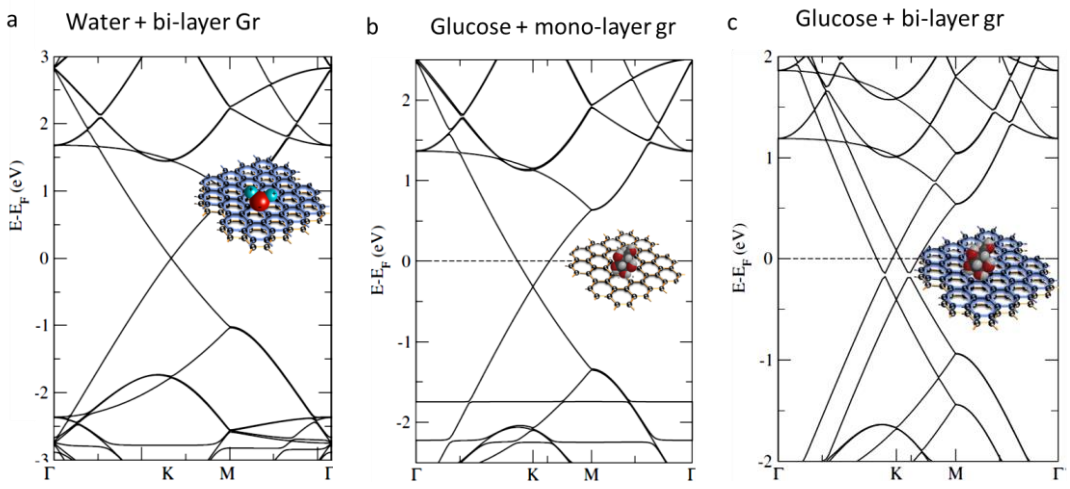

Figure 5.14. Band structure super cells of fully relaxed single molecule on graphene. a, bilayer graphene with single water molecule indicating that graphene has no doping effect. b, monolayer graphene with single glucose molecule. c, bilayer graphene with single glucose molecule. It is shown here that glucose have the same effect (n-doping) on band structures for both mono and bilayer layer graphene.

To understand the reusability of the device, we tested the same device on randomly chosen saliva samples after annealing the device for three hours under vacuum for resetting and residue removal. Figure 5.15, shows the measured results for 5 seconds and 5 minutes compared with clinical laboratory measurements. The glucose concentration was again estimated by calculating the channel resistance for each reading of the transfer curves combined with device sensitivity. These results gave acceptable measurements of glucose concentration in human saliva as can be seen from the plot where the difference between clinical data and our measurement data remained in the range from 2 mM to 7 mM and from 10 mM to 16 mM for 5 seconds and 5 minutes, respectively. The observed trend from the measurements indicates that the device successfully predicted the extra glucose concentration. This variation can be used as a calibration factor in addition to the sensitivity of the device to achieve the desired results accurately after ensuring that the device gave incremental channel resistance variation.

Table 5.2, summarizes the performance of this device compared to previously published results.

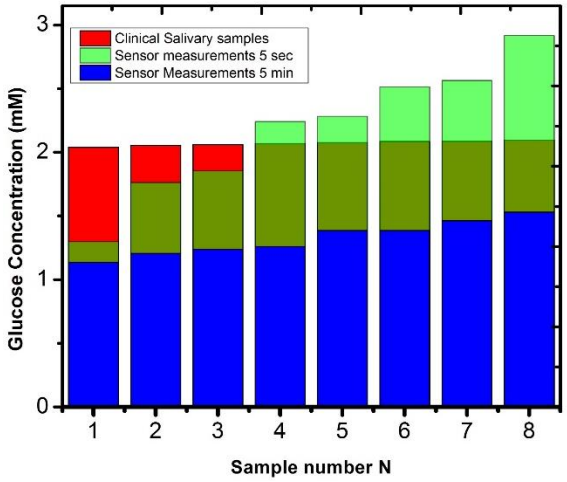

Figure 5.15. Data plot for clinically measured samples spiked with 2 mM and experimental measurements. The measured samples using graphene back gate transistor 5 seconds and 5 minutes (green and blue) respectively against clinical measurements (red). Graphene devices predicted the incremental change after both 5 seconds and 5 minutes.

Examination of monitoring device's selectivity for different parameters is very important since it can be affected by other constituent present human saliva. One of these important factors is pH value of the saliva which strongly depends on the nutrition system of the patient and when one takes the measurement [165]. Therefore, we tracked the device response over the change of pH values by analyzing solutions with different pH values and then studied the transfer characteristic curves as before. Figure 5.16, shows the I_D-V_G curves for the graphene back gate transistor as a function of pH value. The device was measured for incremental step of 1 pH value as shown in Figure 5.16.a. We observed that graphene Dirac voltage is upshifting from ~ 0.3 volt to ~ 1.3 volts as pH value increasing from 5 to 9. This change is due to increased negativity of the solution which leads to

development of negative charge residues [163,164]. Next we evaluated the response to different pH values by taking the measurements at various incremental steps namely 4, 7 and 9 pH values as shown in Figure 5.16.b. We found the Dirac voltage follows the same trend when the incremental change was 1 indicating that the graphene channel properties is affected by the presence of negatively charged environment coming from the variation of pH values of the solution. Another observed change is the change in minimum current conduction and it can be attributed to resist residues during the fabrication process and other molecules existed in the solution. These observations come with agreements with previously reported graphene electrical measurements [166].

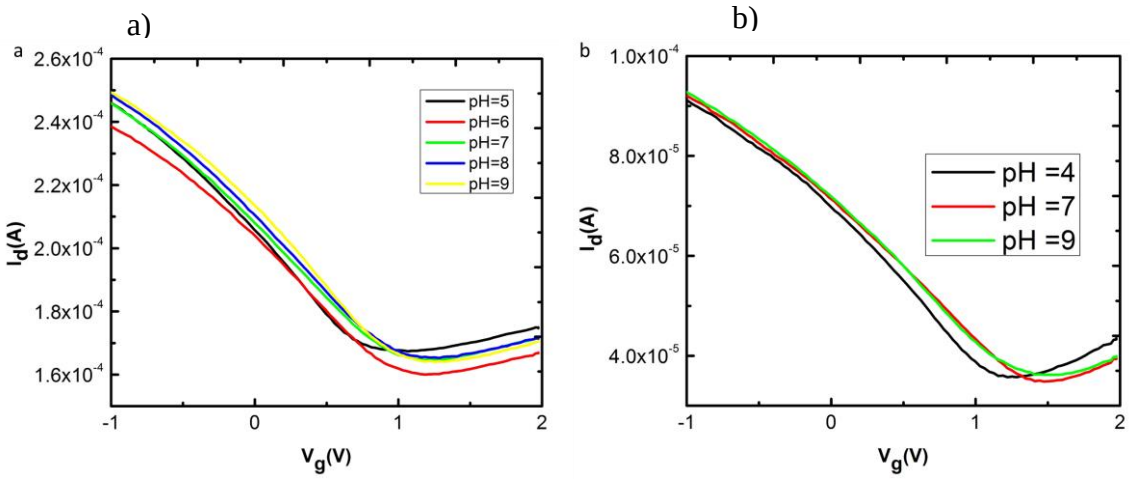

Figure 5.16. I_d-V_g transfer curves for graphene back gate transistor as a function pH ranging from 5 -9. a, I_d-V_g curves showing graphene is sensitive to pH value where dirac voltage point exhibited a upshift as pH value increases. b, I_dV_g as a function of low, median and high pH values showing that the device is sensitive to pH value. Dirac voltage increased by ~0.2 V for every pH value.

Further evaluation of the device selectivity was conducted by measuring the transfer characteristics of the monitoring device subjected to saliva samples with varied pH values followed by introducing of certain amount of glucose concentration into the solution then annealing the device under vacuum for three hours for resetting after

completing different measurement steps. Figure 5.17, shows the selectivity measurement of graphene back gated transistor. The device exhibited the same trend of upshifting Dirac voltage as pH value increased while the Dirac voltage downshifted after introducing 5 mM of glucose into the solution and the trend kept intact under the increased glucose concentration. This explains the presence of positively charged molecules on top of graphene leading to positively induced electrostatic potential through Al_2O_3 dielectric to overcome the negatively charge effect from the presence of increasing pH value. It can be seen that the device was reset after three hours vacuum annealing from the Dirac point reaching neutrality (i.e. removal of residues from graphene channel and contacts leading to less change in the minimum voltage).

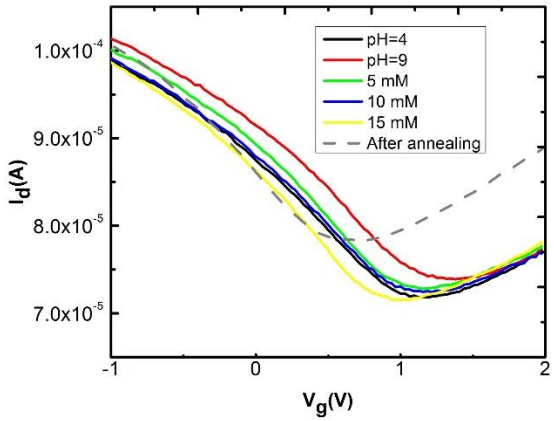

Figure 5.17. I_D-Vg transfer curves for graphene back gate transistor as a function of pH and glucose concentration. The response is measured first for low and high pH values namely 4 (black) and 9 (red). After that, glucose was introduced at 10 mM (blue) and 15 mM (yellow). The change in dirac voltage upshifted as pH increased while it is down shifted with introduction of glucose. The device is then annealed under vacuum for three hours (dashed line) for resetting.

Another device was fabricated by transferring graphene film through aqueous media 300 nm silicon dioxide (SiO_2) dielectric to evaluate graphene device response under the presence of varying concentration of saline (sodium chloride – NaCl rich) DI

water following the same procedure. We achieved saline solution via diluting certain amount *(0.03 g to 0.5 g)* of NaCl in 100 ml DI water followed by the acquisition of transfer curves as shown in figure 5.18. It is obvious that the Dirac voltage is down shifted due to positively added charges on top of graphene channel with strong dependency on NaCl concentration. This observation is attributed to severe ionic environment after adding larger amount of NaCl. Also, this change in Dirac voltage led to a pronounced change in graphene channel conduction. Interestingly we noticed that at higher concentration of NaCl, the device starts to conduct both electron and hole carriers. The small modification in minimum conduction current is because of the low impact of NaCl molecules residues on minimum conduction as expected from increasing ionic strength of the solution [165]. These observations come in agreement with what was observed under the presence of glucose molecules and validate the method of detecting adsorbed materials on top of graphene channel using the two dimensional nature of graphene films and the induced electrostatic potential of these molecules eventually leading to an observed sensible change in the electronic properties of the film.

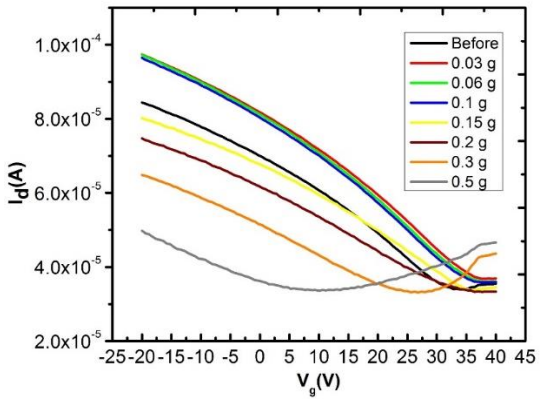

Figure 5.18. Transfer curves I_dV_g plot for the graphene back gate transistor using SiO_2 dielectric as a function of NaCl concentration. The ionic concentration of the solution severely affected graphene channel conduction. It is shown that dirac voltage

down shifted as ionic concentration increased along with a notable decrease in channel conduction.

To evaluate the influence of glucose measurement under the presence of alcoholic for 5 seconds, graphene device was rinsed in different alcoholic concentration with keeping glucose level constant at 10 mM. Acetone is representing alcholoic substance in this measurements. The graphene device response is shown in figure 5.19. It is noted that alcoholic has a pronounced effect on glucose measurement. The fabricated device dirac voltage exhibited down shift from 0.7 V to 0.4 V. Carrier conduction at minimum voltage remained intact during the measurements while channel conduction and mobility decreased gently as it can be seen from the steep branch of the curves due to the presence of oxygen groups in acetone which affect the carrier population in graphene channel.

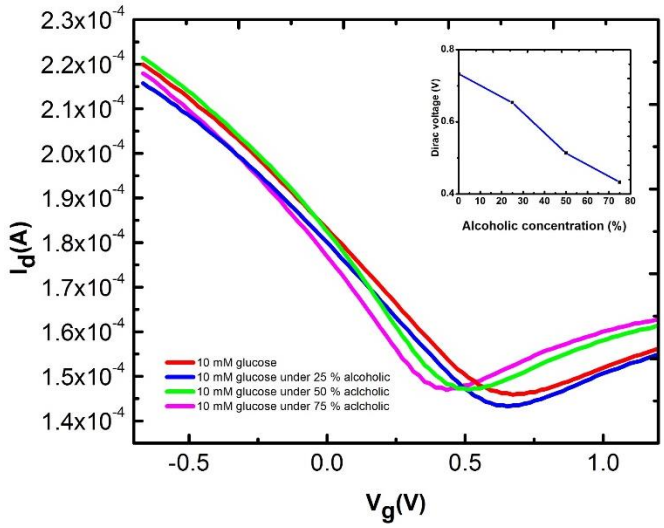

Figure 5.19. I_d-V_g transfer curves for graphene back gate devices as a function of alcoholic concentration. The dirac voltage decreased from 0.7 V to ~ 0.4 V as alcoholic concentration increased from 25 % to 75 %. Glucose measurement is influenced by the presence of alcoholic. The inset showing the extracted dirac voltage as a function of alcoholic concentration.

5.2.4. Conclusion

We show a graphene based simple low-cost sensor for daily monitoring of diabetes non-invasively with high sensitivity, selectivity and response time. The presented device successfully detected the incremental change in glucose concentration.

Chapter 6. Summary and Future Directions

6.1. Summary

Graphene research is receiving great interest owed to its extraordinary properties that makes graphene a prominent candidate among other 2D materials to replace current silicon technology over the next decade. From synthesis standpoint, we developed a sustained CVD Bi-layer graphene film growth at atmospheric pressure. The rendered film features high uniformity, scale reliability, high quality, 93% optical transparency, 819 Ω/□ and low defect. The grown film is then transferred through aqueous media. After that ultra-scaled Al_2O_3 dielectric is utilized in developing finFET architecture combined with graphene channel. The exhibited high mobility > 11,000 $cm^2\ V^{-1}\ s^{-1}$ is attributed to the quality of the grown film, ultra-scaled high-k dielectric and the better electrostatic control offered by the fin structurer. Another novel structure was fabricated to facile the study of metal/graphene resistivity. The obtained low Au/graphene resistance ($1\mu\Omega\text{-}cm^2$) indicated that most of the reported contact resistance in literature is accounted for processing issues.

We presented new sensing method for water quality monitoring based on ion sensitivity. The obtained I_d-V_g characteristic curves showed a pronounced dirac voltage down shift as a function of NaCl concentration. Also, graphene back gated transistor behavior at elevated temperature is reported. It is found that the fabricated devices persevered transistor functionality for operational temperature up to 250 ^oC. The main reason for device failure above that temperature is attributed to gate leakage current through the 10 nm dielectric film. It is worth noting that the graphene FET survived 1

MA/cm^2 before dielectric breakdown. The demonstrated high temperature revealed high potential for considering graphene devices as alternative to current GaN and SiC power transistors.

A brief discussion of grown CVD graphene film on nickel as MFC cathode for simple water treatment technology. Another MFC was designed based on CVD graphene on cu foil. The grown film was used as cathode exposed to the air. It is found that graphene on cu foil exhibited better current generation because of the promoted adhesion interface eventually leading to better current generation that is able to withdraw current out of human saliva efficiently.

For medical application, graphene and CNT is widely used due to their high bio compatibility, sensitivity to outer elements and the ability for functionalization. However, functionalization process requires sophisticated complex steps. From that prospective, we developed a systematic study for non-invasive new sensing approach based on molecular charge transfer. We showed that glucose concentration in artificially made solutions can be monitored using graphene back gate device with sensitivity estimation of 197 Ω/glucose mM and 189Ω/glucose mM for 5 seconds and 5 minutes respectively. Continue in the glucose detection field, the same study is extended to real diabetes samples collected and measured clinically. It is found that glucose level is estimate correctly in lab measurements. The revealed study showing that graphene simple low cost sensor for daily diabetes monitoring. In addition, high sensitivity, selectivity and response time was attainable in the experiment.

6.2. Future Directions

We have demonstrated exciting insights on the pursuit of realizing low power, simple and low cost graphene based devices. Continuing the current progress, the next step is centered on developing a direct CVD graphene synthesis method for pre patterned structures. Hence, making graphene device fabrication process more compatible with current CMOS technology.

We also extending the research spot to cover other 2D materials like MoS_2 and Ws_2. Furthermore, currently we are trying to make flexible graphene devices by integrating the grown film with peeled silicon substrate.

REFERENCES

[1] Alexander A. Balandin, Suchismita Ghosh, Wenzhong Bao, Irene Calizo, Desalegne Teweldebrhan, Feng Miao, and Chun Ning Lau. "Superior thermal conductivity of single-layer graphene." Nano letters 8, no. 3, pp. 902-907, Febraury 2008.

[2] Walt A. De Heer, Claire Berger, Xiaosong Wu, Phillip N. First, Edward H. Conrad, Xuebin Li, Tianbo Li, Joanna Hass, Alexei N. Marchenkov, Edward H. Conrad, Phillip N. First and Walt A. de Heer. "Epitaxial graphene." Solid State Communications 143, no. 1, pp. 92-100, July 2007.

[3] Xuesong Li, Weiwei Cai, Jinho An, Seyoung Kim, Junghyo Nah, Dongxing Yang, Richard Piner, Arunna Velamakannia, Inhwa Junga, Emanuel Tutucb, Sanjy K. Banerjee, Luigi Colombo And Rodney S. Ruof . "Large-area synthesis of high-quality and uniform graphene films on copper foils." Science 324, no. 5932, pp. 1312-1314, May 2009.

[4] Mustafa Lotya, Yenny Hernandez, Paul J. King, Ronan J. Smith, Valeria Nicolosi, Lisa S. Karlsson, Fiona M. Blighe, Sukanta DE ,WANG ZHIMING,I. T. MCGOVERN, S. DUESBERG Georg and N. COLEMAN Jonathan. "Liquid phase production of graphene by exfoliation of graphite in surfactant/water solutions." Journal of the American Chemical Society 131, no. 10, pp. 3611-3620, Febraury 2009

[5] Gunther Lippert, Jarek Dabrowski, Yuji Yamamoto, Felix Herziger, Janina Maultzsch, Max C. Lemme, Wolfgang Mehr, and Grzegorz Lupina. "Molecular beam growth of micrometer-size graphene on mica." Carbon, vol. 52, pp. 40-48, Febraury 2013.

[6] Xuesong Li, Carl W. Magnuson, Archana Venugopal, Jinho An, Ji Won Suk, Boyang Han, Mark Borysiak, Weiwei Cai, Aruna Velamakanni, Yanwu Zhu, Lianfeng Fu, Eric M. Vogel Edgar Voelkl Luigi Colombo And Rodney S. Ruoff. "Graphene films with large domain size by a two-step chemical vapor deposition process." Nano letters, vol. 10, no. 11, pp. 4328-4334, October 2010.

[7] Yagang Yao, Zhuo Li, Ziyin Lin, Kyoung-Sik Moon, Josh Agar, and Chingping Wong. "Controlled growth of multilayer, few-layer, and single-layer graphene on metal substrates." The Journal of Physical Chemistry C 115, no. 13, pp. 5232-5238, March 2011.

[8] Zhengtang Luo, Seungchul Kim, Nicole Kawamoto, Andrew M. Rappe, and AT Charlie Johnson. "Growth mechanism of hexagonal-shape graphene flakes with zigzag edges." ACS nano 5, no. 11, pp. 9154-9160. October 2011.

[9] HoKwon Kim, Cecilia Mattevi, M. Reyes Calvo, Jenny C. Oberg, Luca Artiglia, Stefano Agnoli, Cyrus F. Hirjibehedin, Manish Chhowalla, and Eduardo Saiz. "Activation energy paths for graphene nucleation and growth on Cu." ACS nano 6, no. 4, pp. 3614-3623, March 2012

[10] Y. Zhang et al, Direct observation of a widely tunable bandgap in bilayer graphene, Nature, Volume 459, pp 820-823, 2009.

[11] F. Schwierz, Graphene transistors, Nat. Nanotechnol, Volume 5, pp 487–496, 2010.

[12] Y-M Lin et al, Dual gate graphene FETs with fT of 50 GHz, Nano Lett., Volume 9, Issue 1, pp 422–426, 2009.

[13] M. C. Lemme et al, IEEE Electron Device Lett., Volume 28, Issue 4, pp 282–284, 2007.

[14] A. Reina et al, Large Area, Few-Layer Graphene Films on Arbitrary Substrates by Chemical Vapor Deposition, Nano Lett., Volume 9, Issue 1, pp 30–35, 2009

[15] L. Liao et al, Single-layer graphene on Al2O3/Si substrate: better contrast and higher performance of graphene transistors, Nanotechnology, Volume 21, Issue 1, pp 015705, 2010.

[16] Y-Y Wang et al, Raman studies of monolayer graphene: the substrate effect, J. Phys. Chem. C, Volume 112, Issue 29, 10637–10640, 2008.

[17] T. Ernst et al, Fringing fields in sub-0.1 μm fully depleted SOI MOSFETs: optimization of the device architecture, Solid State Electronics, Volume 46, Issue 3, pp 373-378, 2002.

[18] M. J. Hollander et al, Enhanced transport and transistor performance with oxide seeded high-κ gate dielectrics on wafer-scale epitaxial graphene, Nano Lett., Volume 11, Issue 9, pp 3601–3607, 2011.

[19] S. Kim et al, Realization of a high mobility dual-gated graphene field-effect transistor with Al2O3 dielectric, APPLIED PHYSICS LETTERS, Volume 94, 062107, 2009.

[20] I. Meric et al, Current saturation in zero-bandgap, top-gated graphene field-effect transistors, Nat. Nanotechnol., Volume 3, pp 654–659, 2008

[21] Bunch J S.; Yaish Y.; Brink M.; Bolotin K.; McEuen P L.Nano Lett. 2005, 5, 287

[22] Robinson JA, LaBella M, Zhu M, Hollander M, Kasarda R, Hughes Z, et al. Contacting graphene. Appl. Phys. Lett. 2011;98:053103.1-3.

[23] Meric I, Dean C, Young A, Hone J, Kim P, Shepard KL. Graphene field-effect transistors based on boron nitride gate dielectrics. IEEE IEDM Tech. Dig. 2010, 6-8,556-59.

[24] Semiconductor Industry Association, “The national tech- nology Roadmap for Semiconductors" , 2010

[25] P. Blake, R. Yang, S. V. Morozov, F. Schedin, L. A. Ponomarenko, A. A. Zhukov, R. R. Nair, I. V. Grigorieva, K. S. Novoselov, and A. K. Geim, Solid State Comm., 2009, 149, 1068.

[26] R. Murali, Y. Yang, K. Brenner, T. Beck, and J. D. Meindl, Appl. Phys. Lett., 2009, 94, 243114.

[27] F. Xia, D. B. Farmer, Y. -M. Lin, and P. Avouris, Nano lett., 2010, 10, 715.

[28] F. Xia, D. B. Farmer, Y. -M. Lin, and P. Avouris, Nano lett., 2010, 10, 715.

[29] Nagashio K, Nishimura T, Kita K, Toriumi A. Contact resistivity and current flow path at metal/graphene contact. Appl. Phys. Lett. 2010, 97, 143514, 1-3.

[30] Aaron D. Franklin, Ageeth A. Bol, and Vasili Perebeinos, Electron Device Letters, 2012, 33, 17.

[31] G. Giovannetti, P. A. Khomyakov, G. Brocks, V. M. Karpan, J. van den Brink, and P. J. Kelly, Phys. Rev. Lett., 2008, 101, 026803.

[32] Ravi S. Sundaram, z Mathias Steiner, Hsin-Ying Chiu, Michael Engel, Ageeth A. Bol, Ralph Krupk, Marko Burghard, Klaus Kern, and Phaedon Avouris, Nano Lett. 2011, 11, 3833–3837.

[33] F. Schedin. et al, Nat. Mater 652, 2007

[34] Yavari et. al, Small, 22, 2010

[35] F. Schedin, A. K. Geim, S. V. Morozov, E. W. Hill, P. Blake, M. I. Katsnelson, and K. S. Novoselov, Nat. Mat. 6, 652 (2007).

[36] R. Cheng, J. Bai, L. Liao, H. Zhou, Y. Chen, L. Liu, Y.-C. Lin, S. Jiang, Y. Huang, and X. Duan, PNAS, 109(29), 11588 (2012).

[37] R. S. Pengelly, S. M. Wood, J. W. Milligan, S. T. Sheppard, and W. L. Pribble, IEEE Trans. Microw. Theory. 60(6), 1764 (2012).

[38] Y. Ren, C. Zhu, W. Cai, H. Li, H. Ji, I. Kholmanov, Y. Wu, R. D. Piner, and R. S. Ruoff, Appl. Phys. Lett. 100, 163114 (2012).

[39] S. S. Sabri, J. Guillemette, A. Guermoune, M. Siaj, and T. Szkopek, Appl. Phys. Lett. 100, 113106 (2012).

[40] Q. Shao, G. Liu, D. Teweldebrhan, and A. A. Balandin, Appl. Phys. Lett. 92, 202108 (2008).

[41] A. Venugopal, L. Colombo, and E. M. Vogel, Appl. Phys. Lett. 96, 013512 (2010).

[42] V. K. Nagareddy, I. P. Nikitina, D. K. Gaskill, J. L. Tedesco, R. L. Myers-Ward, C. R. Eddy, J. P. Goss, N. G. Wright, and A. B. Horsfall, Appl. Phys. Lett. 99, 073506 (2011).

[43] K. I. Bolotin, K. J. Sikes, J. Hone, H. L., Stormer and P. Kim, Phys. Rev. Lett. 101(9), 096802 (2008).

[44] A. C. Ferrari, J. C. Meyer, V. Scardaci, C. Casiraghi, M. Lazzeri, F. Mauri, S. Piscanec, D. Jiang, K. S. Novoselov, S. Roth, and A. K. Geim, Phys. Rev. Lett. 97, 187401 (2006).

[45] C. Casiraghi, S. Pisana, K. S. Novoselov, A. K. Geim, and A. C. Ferrari, Appl. Phys. Lett. 91(23), 233108 (2007).

[46] C. H. Lui, Z. Li, Z. Chen, P. V. Klimov, L. E. Brus, and T. F. Heinz, Nano letters, 11(1), 164 (2010).

[47] A. Gupta, G. Chen, P. Joshi, S. Tadigadapa, and P. C. Eklund, Nano Letters, 6(12), 2667 (2006).

[48] A. Reina, S. Thiele, X. T. Jia, S. Bhaviripudi, M. S. Dresselhaus, J. A. Schaefer, and J. Kong, Nano Res. 2(6), 509 (2009).

[49] Malard, L. M.; Pimenta, M. A.; Dresselhaus, G.; Dresselhaus, M. S. Phys. Rep. 2009, 473, 51-87.

[50] Lee, Seunghyun, Kyunghoon Lee, and Zhaohui Zhong. "Wafer scale homogeneous bilayer graphene films by chemical vapor deposition." Nano letters 10.11 (2010): 4702-4707.

[51] Y. -W. Tan, Y. Zhang, H. L. Stormer, and P. Kim, Eur. Phys. J. Special Topics 148, 15 (2007).

[52] S. Kim, J. Nah, I. Jo, D. Shahrjerdi, L. Colombo, Z. Yao, E. Tutuc, and S. K. Banerjee, Appl. Phys. Lett. 94, 062107 (2009).

[53] I. Meric, M. Y. Han, A. F. Young, B. Ozyilmaz, P. Kim, and K. L. Shepard, Nat. Nanotechnol. 3, 654 (2008).

[54] A. Gupta, G. Chen, P. Joshi, S. Tadigadapa, and P. C. Eklund, Nano Letters, 6(12), 2667 (2006).

[55] T. Fang, A. Konar, H. Xing, and D. Jena, Appl. Phys. Lett. 91, 092109 (2007).

[56] M. T. Ghoneim, C. E. Smith, and M. M. Hussain, Appl. Phys. Lett. 102, 183115 (2013).

[57] K. Sugihara, K. Kawamura, and T. Tsuzuku, J. Phys. Soc. Jpn. 47, 1210 (1979).

[58] J. Kolodzey, T. N. Adam, G. Qui, I. Rau, J. O. Olowolafe, J. S. Suehle, and Y. Chen, IEEE Trans. Elect. Dev. 47(1), 107 (2000).

[59] Rojas, J., Torres Sevilla, G., Hussain, M. Can We Build a Truly High Performance Flexible Computer? Nature Sci. Rep. 3, 2609 (2013).

[60] K. Geim, K. S. Novoselov, Nat. Mater. 2007, 6, 183.

[61] F. Schedin, A. Geim, S. Morozov, E. Hill, P. Blake, M. Katsnelson, K. Novoselov, Nat. Mater. 2007, 6, 652.

[62] L. Tang, Y. Wang, Y. Li, H. Feng, J. Lu, J. Li, Adv. Funct. Mater. 2009, 19, 2782.

[63] O. Akhavan, E. Ghaderi, J. Phys. Chem. C 2009, 113, 20214.

[64] S. Stankovich, D. A. Dikin, G. H. Dommett, K. M. Kohlhaas, E. J. Zimney, E. A. Stach, R. D. Piner, S. T. Nguyen, R. S. Ruoff, Nature 2006, 442, 282.

[65] Y. Shao, J. Wang, H. Wu, J. Liu, I. A. Aksay, Y. Lin, Electroanalysis 2010, 22, 1027.

[66] Y. Liu, J. Chen, N. T. Anh, C. O. Too, V. Misoska, G. G. Wallace, J. Electrochem. Soc. 2008, 155, K100.

[67] Y. Liu, D. Yu, C. Zeng, Z. Miao, L. Dai, Langmuir 2010, 26, 6158.

[68] Shan, H. Yang, J. Song, D. Han, A. Ivaska, L. Niu, Anal. Chem. 2009, 81, 2378.

[69] Z. Zhu, L. Garcia-Gancedo, A. J. Flewitt, H. Xie, F. Moussy, W. I. Milne, Sensors 2012, 12, 5996.

[70] Y. H. Kwak, D. S. Choi, Y. N. Kim, H. Kim, D. H. Yoon, S.-S. Ahn, J.-W. Yang, W. S. Yang, S. Seo, Biosensors and Bioelectronics 2012, 37, 82.

[71] MingáLi, Nanoscale 2010, 2, 1485.

[72] P. Wu, Q. Shao, Y. Hu, J. Jin, Y. Yin, H. Zhang, C. Cai, Electrochim. Acta 2010, 55, 8606.

[73] Y. Song, K. Qu, C. Zhao, J. Ren, X. Qu, Adv. Mater. 2010, 22, 2206.

[74] Y. Zhang, S. Liu, L. Wang, X. Qin, J. Tian, W. Lu, G. Chang, X. Sun, Rsc Advances 2012, 2, 538.

[75] H. Wu, J. Wang, X. Kang, C. Wang, D. Wang, J. Liu, I. A. Aksay, Y. Lin, Talanta 2009, 80, 403.

[76] J. Luo, S. Jiang, H. Zhang, J. Jiang, X. Liu, Anal. Chim. Acta 2012, 709, 47.

[77] R. Wilson, A. Turner, Biosensors and Bioelectronics 1992, 7, 165.

[78] X. Kang, Z. Mai, X. Zou, P. Cai, J. Mo, Anal. Biochem. 2007, 363, 143.

[79] Das, S. Pisana, B. Chakraborty, S. Piscanec, S. Saha, U. Waghmare, K. Novoselov, H. Krishnamurthy, A. Geim, A. Ferrari, Nat. Nanotechnol. 2008, 3, 210.

[80] T. O. Wehling, A. I. Lichtenstein, M. I. Katsnelson, Appl. Phys. Lett. 2008, 93, 202110.

[81] M. Qazi, M. W. Nomani, M. Chandrashekhar, V. B. Shields, M. G. Spencer, G. Koley, Appl. Phys. Express 2010, 3, 075101.

[82] K. S. Novoselov, A. K. Geim, S. Morozov, D. Jiang, Y. Zhang, S. Dubonos, I. Grigorieva, A. Firsov, science 2004, 306, 666.

[83] Y. Zhang, J. P. Small, M. E. Amori, P. Kim, Phys. Rev. Lett. 2005, 94, 176803.

[84] Das, S. Pisana, B. Chakraborty, S. Piscanec, S. Saha, U. Waghmare, K. Novoselov, H. Krishnamurthy, A. Geim, A. Ferrari, Nat. Nanotechnol. 2008, 3, 210.

[85] Hwang, S. Adam, S. D. Sarma, Phys. Rev. B. 2007, 76, 195421.

[86] M. T. Ghoneim, C. E. Smith, M. M. Hussain, Appl. Phys. Lett. 2013, 102, 183115.

[87] C. Smith, R. Qaisi, Z. Liu, Q. Yu, M. M. Hussain, ACS nano 2013, 7, 5818.

[88] X. Li, W. Cai, J. An, S. Kim, J. Nah, D. Yang, R. Piner, A. Velamakanni, I. Jung, E. Tutuc, Science 2009, 324, 1312.

[89] L. Malard, M. Pimenta, G. Dresselhaus, M. Dresselhaus, Phys. Rep. 2009, 473, 51.

[90] Ferrari, J. Meyer, V. Scardaci, C. Casiraghi, M. Lazzeri, F. Mauri, S. Piscanec, D. Jiang, K. Novoselov, S. Roth, Phys. Rev. Lett. 2006, 97, 187401.

[91] Casiraghi, S. Pisana, K. Novoselov, A. Geim, A. Ferrari, Appl. Phys. Lett. 2007, 91, 233108.

[92] H. Lui, Z. Li, Z. Chen, P. V. Klimov, L. E. Brus, T. F. Heinz, Nano Lett. 2010, 11, 164.

[93] Z. Ni, Y. Wang, T. Yu, Z. Shen, Nano Res. 2008, 1, 273.

[94] G. Hamaide, F. Allibert, H. Hovel, S. Cristoloveanu, J. Appl. Phys. 2007, 101, 114513.

[95] Ionica, A. El Hajj Diab, S. Cristoloveanu, "Gold nanoparticles detection using intrinsic SOI-based sensor", presented at Nanotechnology (IEEE-NANO), 2011 11th IEEE Conference on, 2011.

[96] S. Pisana, M. Lazzeri, C. Casiraghi, K. S. Novoselov, A. K. Geim, A. C. Ferrari, F. Mauri, Nat. Mater. 2007, 6, 198.

[97] X. Dong, D. Fu, W. Fang, Y. Shi, P. Chen, L. J. Li, Small 2009, 5, 1422.

[98] C. SekharáRout, Chem. Commun. 2008, 5155.

[99] C. Stampfer, F. Molitor, D. Graf, K. Ensslin, A. Jungen, C. Hierold, L. Wirtz, Appl. Phys. Lett. 2007, 91, 241907.

[100] Y. Y. Wang, Z. H. Ni, T. Yu, Z. X. Shen, H. M. Wang, Y. H. Wu, W. Chen, A. T. Shen Wee, J. Phys. Chem. C 2008, 112, 10637.

[101] T. Mohiuddin, A. Lombardo, R. Nair, A. Bonetti, G. Savini, R. Jalil, N. Bonini, D. Basko, C. Galiotis, N. Marzari, Phys. Rev. B. 2009, 79, 205433.

[102] F. Shackelford, W. Alexander, CRC press, 2000.

[103] A. Heller, B. Feldman, Electrochemistry in diabetes management. Accounts of chemical research 43, 963-973 (2010).

[104] M. Gerard, A. Chaubey, B. Malhotra, Application of conducting polymers to biosensors. Biosensors and Bioelectronics 17, 345-359 (2002).

[105] C. Dhand, M. Das, M. Datta, B. Malhotra, Recent advances in polyaniline based biosensors. Biosensors and Bioelectronics 26, 2811-2821 (2011).

[106] A. I. Gopalan, K. P. Lee, D. Ragupathy, S. H. Lee, J. W. Lee, An electrochemical glucose biosensor exploiting a polyaniline grafted multiwalled carbon nanotube/perfluorosulfonate ionomer–silica nanocomposite. Biomaterials 30, 5999-6005 (2009).

[107] H. Xue, Z. Shen, C. Li, Improved selectivity and stability of glucose biosensor based on in situ electropolymerized polyaniline–polyacrylonitrile composite film. Biosensors and Bioelectronics 20, 2330-2334 (2005).

[108] A. Kausaite-Minkstimiene, V. Mazeiko, A. Ramanaviciene, A. Ramanavicius, Enzymatically synthesized polyaniline layer for extension of linear

detection region of amperometric glucose biosensor. Biosensors and Bioelectronics 26, 790-797 (2010).

[109] P. Vashist, S. Singh, N. Gupta, R. Saxena, Role of early screening for diabetic retinopathy in patients with diabetes mellitus: an overview. Indian journal of community medicine: official publication of Indian Association of Preventive & Social Medicine 36, 247 (2011).

[110] U. P. S. T. Force, Screening for type 2 diabetes mellitus in adults: US Preventive Services Task Force recommendation statement. Annals of Internal Medicine 148, 846 (2008).

[111] R. Valdez, Detecting undiagnosed type 2 diabetes: family history as a risk factor and screening tool. Journal of diabetes science and technology 3, 722-726 (2009).

[112] V. Nagalaxmi, V. Priyanka, Can Saliva be a Marker for Predicting Type 1 Diabetes Mellitus?—A Pilot Study. Journal of Indian Academy of Oral Medicine & Radiology 23, (2011).

[113] A. S. Panchbhai, S. S. Degwekar, R. R. Bhowte, Estimation of salivary glucose, salivary amylase, salivary total protein and salivary flow rate in diabetics in India. Journal of oral science 52, 359-368 (2010).

[114] A. C. U. Vasconcelos, M. S. M. Soares, P. C. Almeida, T. C. Soares, Comparative study of the concentration of salivary and blood glucose in type 2 diabetic patients. Journal of oral science 52, 293-298 (2010).

[115] P. Abikshyeet, V. Ramesh, N. Oza, Glucose estimation in the salivary secretion of diabetes mellitus patients. Diabetes, metabolic syndrome and obesity: targets and therapy 5, 149 (2012).

[116] S. M. Al-Zahawi, H. A. M. Al-Barzenji, Z. A. Al-Qassab, Effects of diabetes mellitus types II on salivary flow rate and some salivary parameters (total protein, glucose, and amylase) in Erbil city. J Bagh Coll Dent 24, 123-127 (2012).

[117] J. H. Meurman et al., Saliva in non-insulin-dependent diabetic patients and control subjects: the role of the autonomic nervous system. Oral Surgery, Oral Medicine, Oral Pathology, Oral Radiology, and Endodontology 86, 69-76 (1998).

[118] C. Jurysta et al., Salivary glucose concentration and excretion in normal and diabetic subjects. BioMed Research International 2009, (2009).

[119] M. J. Bernardi et al., Study of the buffering capacity, pH and salivary flow rate in type 2 well-controlled and poorly controlled diabetic patients. Oral health & preventive dentistry 5, 73-78 (2006).

[120] A. Darwazeh, T. MacFarlane, A. McCuish, P. J. Lamey, Mixed salivary glucose levels and candidal carriage in patients with diabetes mellitus. Journal of oral pathology & medicine 20, 280-283 (1991).

[121] A. S. Panchbhai, Correlation of salivary glucose level with blood glucose level in diabetes mellitus. Journal of oral & maxillofacial research 3, (2012).

[122] N. Oliver, C. Toumazou, A. Cass, D. Johnston, Glucose sensors: a review of current and emerging technology. Diabetic Medicine 26, 197-210 (2009).

[123] J. Wang, P. V. Pamidi, Sol-gel-derived gold composite electrodes. Analytical chemistry 69, 4490-4494 (1997).

[124] F. Patolsky, Y. Weizmann, I. Willner, Long-range electrical contacting of redox enzymes by SWCNT connectors. Angewandte Chemie International Edition 43, 2113-2117 (2004).

[125] G. Kokkindis, J. Leger, C. Lamy, Structural effects in electrocatalysis: oxidation of D-glucose on pt (100),(110) and (111) single crystal electrodes and the effect of upd adlayers of Pb, Tl and Bi. Journal of electroanalytical chemistry and interfacial electrochemistry 242, 221-242 (1988).

[126] N. Xonoglou, G. Kokkinidis, Catalysis of the oxidation of monosaccharides on platinum surfaces modified by underpotential submonolayers. Bioelectrochemistry and Bioenergetics 12, 485-498 (1984).

[127] A. Salimi, M. Roushani, Non-enzymatic glucose detection free of ascorbic acid interference using nickel powder and nafion sol–gel dispersed renewable carbon ceramic electrode. Electrochemistry Communications 7, 879-887 (2005).

[128] S. Chen et al., Carbon nanodots as a matrix for the analysis of low-molecular-weight molecules in both positive-and negative-ion matrix-assisted laser desorption/ionization time-of-flight mass spectrometry and quantification of glucose and uric acid in real samples. Analytical chemistry 85, 6646-6652 (2013).

[129] R. Obregón et al., Non-invasive measurement of glucose uptake of skeletal muscle tissue models using a glucose nanobiosensor. Biosensors and Bioelectronics 50, 194-201 (2013).

[130] R. U. Malik et al., Detection of G protein-selective G protein-coupled receptor (GPCR) conformations in live cells. Journal of Biological Chemistry 288, 17167-17178 (2013).

[131] D. Ye et al., A novel nonenzymatic sensor based on CuO nanoneedle/graphene/carbon nanofiber modified electrode for probing glucose in saliva. Talanta 116, 223-230 (2013).

[132] J. Zhang, W. G. Hodge. (Google Patents, 2013).

[133] A. K. Geim, K. S. Novoselov, The rise of graphene. Nature materials 6, 183-191 (2007).

[134] K. S. Novoselov et al., Electric field effect in atomically thin carbon films. science 306, 666-669 (2004).

[135] A. C. Neto, F. Guinea, N. Peres, K. S. Novoselov, A. K. Geim, The electronic properties of graphene. Reviews of modern physics 81, 109 (2009).

[136] I. Meric et al., Current saturation in zero-bandgap, top-gated graphene field-effect transistors. Nature nanotechnology 3, 654-659 (2008).

[137] K. T. Chan, J. Neaton, M. L. Cohen, First-principles study of metal adatom adsorption on graphene. Physical Review B 77, 235430 (2008).

[138] M. T. Ghoneim, C. E. Smith, M. M. Hussain, Simplistic graphene transfer process and its impact on contact resistance. Applied Physics Letters 102, 183115 (2013).

[139] X. Li et al., Transfer of large-area graphene films for high-performance transparent conductive electrodes. Nano letters 9, 4359-4363 (2009).

[140] Q. Yu et al., Graphene segregated on Ni surfaces and transferred to insulators. Applied Physics Letters 93, 113103 (2008).

[141] A. Reina et al., Growth of large-area single-and bi-layer graphene by controlled carbon precipitation on polycrystalline Ni surfaces. Nano Research 2, 509-516 (2009).

[142] A. Ferrari et al., Raman spectrum of graphene and graphene layers. Physical review letters 97, 187401 (2006).

[143] C. Casiraghi, S. Pisana, K. Novoselov, A. Geim, A. Ferrari, Raman fingerprint of charged impurities in graphene. Applied Physics Letters 91, 233108 (2007).

[144] C. H. Lui et al., Imaging stacking order in few-layer graphene. Nano letters 11, 164-169 (2010).

[145] A. Gupta, G. Chen, P. Joshi, S. Tadigadapa, P. Eklund, Raman scattering from high-frequency phonons in supported n-graphene layer films. Nano letters 6, 2667-2673 (2006).

[146] A. C. Ferrari, Raman spectroscopy of graphene and graphite: disorder, electron–phonon coupling, doping and nonadiabatic effects. Solid state communications 143, 47-57 (2007).

[147] Z. Ni, Y. Wang, T. Yu, Z. Shen, Raman spectroscopy and imaging of graphene. Nano Research 1, 273-291 (2008).

[148] T. O. Wehling, A. I. Lichtenstein, M. I. Katsnelson, First-principles studies of water adsorption on graphene: The role of the substrate. Applied Physics Letters 93, 202110-202110-202113 (2008).

[149] A. Das et al., Monitoring dopants by Raman scattering in an electrochemically top-gated graphene transistor. Nature nanotechnology 3, 210-215 (2008).

[150] C. SekharáRout, Changes in the electronic structure and properties of graphene induced by molecular charge-transfer. Chemical Communications, 5155-5157 (2008).

[151] C. Casiraghi, S. Pisana, K. Novoselov, A. Geim, A. Ferrari, Raman fingerprint of charged impurities in graphene. Applied Physics Letters 91, 233108 (2007).

[152] Y.-H. Zhang et al., Improving gas sensing properties of graphene by introducing dopants and defects: a first-principles study. Nanotechnology 20, 185504 (2009).

[153] E. Hwang, S. Adam, S. D. Sarma, Transport in chemically doped graphene in the presence of adsorbed molecules. Physical Review B 76, 195421 (2007).

[154] J.-H. Chen et al., Charged-impurity scattering in graphene. Nature Physics 4, 377-381 (2008).

[155] T. Österberg, S. Landahl, B. Hedegård, Salivary flow, saliva, pH and buffering capacity in 70-year-old men and women. Journal of Oral Rehabilitation 11, 157-170 (1984).

[156] N. Hiraishi et al., Effect of artificial saliva contamination on pH value change and dentin bond strength. Dental Materials 19, 429-434 (2003).

[157] Q. He, S. Wu, Z. Yin, H. Zhang, Graphene-based electronic sensors. Chemical Science 3, 1764-1772 (2012).

[158] O. Leenaerts, B. Partoens, F. Peeters, Adsorption of H 2 O, N H 3, CO, N O 2, and NO on graphene: A first-principles study. Physical Review B 77, 125416 (2008).

[159] H. Liu, Y. Liu, D. Zhu, Chemical doping of graphene. Journal of materials chemistry 21, 3335-3345 (2011).

[160] Q. Zhang et al., Graphene surface plasmons at the near-infrared optical regime. Scientific reports 4, (2014).

[161] J.-L. Chen, X.-P. Yan, Ionic strength and pH reversible response of visible and near-infrared fluorescence of graphene oxide nanosheets for monitoring the extracellular pH. Chemical Communications 47, 3135-3137 (2011).

[162] P. K. Ang, W. Chen, A. T. S. Wee, K. P. Loh, Solution-gated epitaxial graphene as pH sensor. Journal of the American Chemical Society 130, 14392-14393 (2008).

[163] Y. Ohno, K. Maehashi, Y. Yamashiro, K. Matsumoto, Electrolyte-gated graphene field-effect transistors for detecting pH and protein adsorption. Nano Letters 9, 3318-3322 (2009).

[164] Z.-Q. Zhao, X. Chen, Q. Yang, J.-H. Liu, X.-J. Huang, Selective adsorption toward toxic metal ions results in selective response: electrochemical studies on a polypyrrole/reduced graphene oxide nanocomposite. Chem. Commun. 48, 2180-2182 (2012).

[165] H. Bai, C. Li, X. Wang, G. Shi, A pH-sensitive graphene oxide composite hydrogel. Chemical Communications 46, 2376-2378 (2010).

[166] J. Liu et al., Synthesis, characterization, and multilayer assembly of pH sensitive graphene− polymer nanocomposites. Langmuir 26, 10068-10075 (2010).

[167] H. Li, T. Lu, L. Pan, Y. Zhang, Z. Sun, Electrosorption behavior of graphene in NaCl solutions. J. Mater. Chem. 19, 6773-6779 (2009).